

---

Unterschrift BetreuerIn



TECHNISCHE  
UNIVERSITÄT  
WIEN  
Vienna University of Technology

## DIPLOMARBEIT

# Effect of glycation on surface charge and indentation stiffness of individual collagen fibrils

carried out at the Institut für Leichtbau und Struktur-Biomechanik  
at the Vienna University of Technology

under guidance of

**Univ.Prof. Dipl.-Ing. Dr.sc.nat. Philipp Thurner,**  
**Univ.Prof. Dipl.-Ing. Dr.sc.techn. Georg Schitter**

and assistance of

**Univ.Ass. Dipl.-Ing. Mathis Nalbach**  
**Univ.Ass. Dipl.-Ing. Mathias Poik**

by

**Manuel Rufin**

**Mat.Nr.: 01017953**

Lambrechtgasse 8/6-8,  
1040 Vienna, Austria

September 25, 2020

---

Unterschrift StudentIn

## *Affidavit*

I declare in lieu of oath, that I wrote this thesis and performed the associated research myself, using only literature cited in this volume. If text passages from sources are used literally, they are marked as such.

I confirm that this work is original and has not been submitted elsewhere for any examination, nor is it currently under consideration for a thesis elsewhere.

Wien, September 25, 2020

\_\_\_\_\_  
Unterschrift StudentIn

# Zusammenfassung

Kollagen gilt als das häufigste und wahrscheinlich wichtigste Strukturprotein in Säugetieren. In Weichgeweben ordnen sich die Proteinmoleküle vorwiegend zu Fibrillen an, wobei sie verschiedene Arten intermolekularer Bindungen bilden. Eine Art davon sind sogenannte Advanced Glycation Endproducts (AGEs). Sie sind das Ergebnis einer komplizierten Abfolge nichtenzymatischer chemischer Reaktionen der Kollagenproteine mit verschiedenen Sacchariden, die üblicherweise als Glykierung bezeichnet werden, und tragen nachweislich zur im Alter beobachteten Qualitätsverminderung des Gewebes oder zu degenerativen Erkrankungen wie dem Diabetes mellitus bei. Die genauen Mechanismen der Gewebeeränderung und -verschlechterung sind jedoch nicht vollständig verstanden und sind daher Gegenstand aktueller Forschung.

In vorliegender Studie sollen die physiologischen Auswirkungen von AGEs durch In-situ-Messungen einzelner Kollagenfibrillen aus Mäuseschwanzsehnen, glykiert mit dem hochreaktiven Ketoaldehyd Methylglyoxal (MGO), welches als Zwischenprodukt auch in der physiologischen AGE-Reaktionskaskade zu finden ist, modelliert und erforscht werden.

Eine Nanoindentationsmessung in phosphatgepufferten Salzlösung (PBS) durch Rasterkraftmikroskopie (AFM) wurde an denselben Fibrillen ( $N = 10$ ) sowohl vor als auch nach der Glykierung durchgeführt, um *gepaarte* Änderungen an der Fibrillensteifigkeit zu erforschen. Parallel dazu wurden in ähnlicher Weise und an denselben Fibrillen mittels Raster-Kelvin-Mikroskopie (KPFM) in Raumluft Veränderungen des elektrischen Oberflächenpotentials, welches eine relevante Eigenschaft für Zellinteraktionen und -adhäsion darstellt, untersucht. Die Ergebnisse zeigen statistisch signifikante unterschiedliche Veränderungen sowohl der Fibrillensteifigkeit als auch des Oberflächenpotentials im Vergleich zu einer ähnlich behandelten, aber nicht glykierten Kontrollgruppe ( $N = 10$ ). Während das Mittel des Elastizitätsmodulus  $E_{mod}$  sowohl für die Kontroll-  $\Delta E_{mod} \approx +15\%(\pm 32\%SD)$  als auch die MGO-Gruppe  $\Delta E_{mod} \approx +42\%(\pm 33\%SD)$  anstieg, verschob sich das Mittel der Oberflächenpotentiale  $\Phi$  nur vernachlässigbar leicht nach oben für die Kontrollgruppe  $\Delta \Phi \approx +20\%(\pm 21\%SD)$  und signifikant nach unten für die MGO-Gruppe  $\Delta \Phi \approx -173\%(\pm 86\%SD)$  (SD...Standardabweichung). Hiermit konnte erstmals erfolgreich die durch Glykierung verursachte Fibrillenversteifung *direkt* mit der Änderung des elektrischen Oberflächenpotentials in Verbindung gebracht werden.

Im Rahmen der Datenanalyse wurde zusätzlich für die Bestimmung des Kontaktpunkts in der AFM Kraftkurvenanalyse ein neuartiger Ansatz durch Convolutional Neural Networks (CNNs) entwickelt, trainiert und eingesetzt. Im Vergleich zu anderen State-of-the-Art Methoden erweist sich der neue Ansatz als präziser und robuster.

# Abstract

Collagen is the most abundant and arguably most important structural protein in mammals. In soft tissues the protein molecules predominantly arrange into fibrils by forming different types of intermolecular bonds, one of which being Advanced Glycation Endproducts (AGEs). They are the result of a complicated cascade of non-enzymatic chemical reactions, commonly referred to as glycation, of the collagen proteins with sugar compounds and have been shown to contribute to the tissue deterioration observed in old age or common degenerative diseases such as diabetes mellitus. The exact mechanisms of tissue change and deterioration, however, are not fully understood and are therefore worthy of examination.

In this study we model the physiological effects of AGEs by *in-situ* measurements of individual collagen fibrils from mouse tail tendon glycated with Methylglyoxal (MGO), a highly reactive compound that is also found as intermediate product in the physiological AGE reaction cascade.

Nanoindentation measurements in phosphate buffered saline (PBS) through Atomic Force Microscopy (AFM) were conducted on the same fibrils (N=10) before and after glycation to assess *paired* changes in fibril stiffness. In a similar fashion Kelvin Probe Force Microscopy (KPFM) in air was conducted on the very same fibrils before and after glycation to test for changes in electrical surface potential, which can be an important property for cell interaction and adhesion. Results show statistically significant different changes in both fibril stiffness as well as surface potential compared to a similarly treated but unglycated control group (N=10). While means of elastic modulus  $E_{mod}$  went up for both control  $\Delta E_{mod} \approx +15\%(\pm 32\%SD)$  and MGO  $\Delta E_{mod} \approx +42\%(\pm 33\%SD)$  groups, surface potential  $\Phi$  means shifted slightly up for the control  $\Delta\Phi \approx +20\%(\pm 21\%SD)$  and significantly down for MGO  $\Delta\Phi \approx -173\%(\pm 86\%SD)$  (SD...Standard Deviation). This was the first time that the stiffening of collagen fibrils caused by glycation could be *directly* linked to the change in the electrical surface potential.

In the course of data analysis, for the determination of the contact point in AFM force curve analysis a novel approach through convolutional neural networks (CNNs) has been developed, trained and deployed. A comparison to other state of the art methods shows it to be significantly more precise and robust.



Die approbierte gedruckte Originalversion dieser Diplomarbeit ist an der TU Wien Bibliothek verfügbar.  
The approved original version of this thesis is available in print at TU Wien Bibliothek.

# Contents

<b>1. Introduction</b>	<b>1</b>
<b>2. Background</b>	<b>5</b>
2.1. Collagen . . . . .	5
2.1.1. Structure . . . . .	6
2.1.2. Mechanics . . . . .	8
2.1.3. Glycation . . . . .	11
2.2. Atomic Force Microscopy . . . . .	13
2.2.1. Force Mapping Principles . . . . .	15
2.2.2. Kelvin Probe Force Microscopy . . . . .	18
<b>3. Materials and Methods</b>	<b>23</b>
3.1. In Vitro Glycation of Collagen Fibrils . . . . .	23
3.1.1. Sample Preparation and Experiment Work-Flow . . . . .	23
3.1.2. AFM Force Mapping . . . . .	27
3.1.3. KPFM Surface Potential Measurement . . . . .	33
3.1.4. Statistical Analysis . . . . .	36
<b>4. Contact Point Determination via Convolutional Neural Network</b>	<b>39</b>
4.1. Contact Point: State of the Art . . . . .	39
4.2. Deep Convolutional Neural Networks . . . . .	45
4.3. Contact Point Estimation via Convolutional Neural Network . . . . .	47
4.3.1. Architecture . . . . .	48
4.3.2. Data Set and Training . . . . .	49
4.4. Results and Comparison . . . . .	49
<b>5. Mechanics and Surface Potential of Individual Collagen Fibrils as a Function of In Vitro Glycation</b>	<b>57</b>
5.1. Changes in Fibril Indentation Modulus through Glycation . . . . .	57
5.2. Changes in Fibril Surface Potential through Glycation . . . . .	61
5.3. Other Metrics . . . . .	61
<b>6. Discussion</b>	<b>69</b>
<b>7. Conclusion</b>	<b>75</b>

<b>Bibliography and References</b>	<b>i</b>
<b>A. Appendix</b>	<b>xi</b>
A.1. Alternative Statistical Analysis . . . . .	xi
A.2. D-Banding Statistical Analysis . . . . .	xiii
A.3. Handling of Debris on Fibrils . . . . .	xiii



# 1. Introduction

Collagens are the most abundant proteins found in mammals and constitute about 1/3 of the overall protein mass in humans. Collagens are the main constituent of most fibrous tissues such as tendons, ligaments, blood vessels, skin, and in its calcified form, bone and dentin [1]. The structures collagens build are highly hierarchical, with the lowest level building block being triple helical molecules of  $\sim 300$  nm in length and  $\sim 1.5$  nm wide, called tropocollagens, that then assemble by stacking in a staggered fashion into cylindrical structures, called fibrils, with between 50 – 500 nm in width [2]. These fibrils then form fibers in tendons and ligaments, fibrous meshes in skin or calcified fibers in bone at the tissue level, defining many of the tissues mechanical as well as biological properties and functions. In their early life cycle, after biosynthesis starting in and completing outside of cells, collagen fibrils are stabilized by enzymatically formed covalent bonds, cross-linking the non-helical tail regions of tropocollagen. Over longer time spans, there is a second type of cross-linking, called glycation, that through the well known Maillard reaction produces inter- as well as intra-molecular covalent bonds called advanced glycation end products (AGEs). These reactions happen in all biological tissues but are prone to accumulate due to their low turnover rate in some collagenous tissues, e.g. in tendons [3][4][5].

Accumulation of AGEs in connective tissues is linked to the natural ageing process, high dietary sugar consumption and to diabetes mellitus [6]. Caused by the sugar rich modern western diet, physical inactivity and increasing overweight and obesity rates, about 60 million people in Europe have diabetes, the WHO reports. This affects about 10.3% of men and 9.6% of women aged 25 years or older. The WHO projects a doubling of diabetes associated deaths between 2005 and 2030 [7], making diabetes a primary public health concern. The resulting accumulation of AGEs in biological tissues has been connected to inflammation [8] and loss in tissue functionality such as cell adhesion [9] and wound healing [10]. Long term pathologies linked to AGEs are for example retinopathy [11], atherosclerosis [12], Alzheimer's disease [13], osteoporosis [14][15] and diabetic nephropathy [16].

AGE formation in collagen fibrils leads to changes in their properties in a me-

chanical as well as in a molecular-biological way. Mechanical changes in tendon, specifically, have over the past two decades been subject of several studies, involving different techniques. At the fascicle to tendon level increased stiffness, toughness and ultimate strength have been observed [17][18][19][20] and linked to diminished inter-fiber sliding in stand alone [21] and X-ray scattering-combined [22] tensile tests. At the fibril level atomic force microscopy (AFM)-aided nanoindentation tests using ribose as an AGE cross-linker [23] as well as nanomechanical tensile tests using methylglyoxal (MGO) [20], have shown increases in stiffness of individual fibrils, while atomistic simulations showed similar effects for arginine-lysine derived AGEs [24].

The biological consequences of collagen glycation are based on collagen's important role in shaping the cellular microenvironment of the extracellular matrix (ECM). Cells can non-covalently bind to Gly-x-Hyp-Gly-Glu-Arg motifs on tropocollagen molecules via transmembrane integrin receptors [25], which is important for cell adhesion, migration and growth [26][27]. The main amino acids involved in AGE formation are believed to be arginine and lysine [28][24], both having positively charged functional groups. Surface charge shifts towards more negative values have been shown to occur through the process of glycation using optical staining techniques [29] and more recently Kelvin probe force microscopy (KPFM) [30][31]. Furthermore, diminished collagen to proteoglycan binding has been shown to be linked to glycation processes[9].

## Scope of this Thesis

In this work we aimed to further deepen our understanding of the effects of AGE cross-links on the nanoscale mechanics and biology of collagen fibrils. We used methylglyoxal (MGO) as a cross-linking agent for *in vitro* glycation of individually exposed collagen fibrils from mouse tail tendon. MGO is a late by-product of the physiological Maillard reaction and capable of cross-linking to saturation in mere hours [32]. Fibril mechanics, specifically fibril stiffness, were tested using AFM nanoindentations in PBS, which has not been done on MGO glycated fibrils before. Furthermore, we conducted KPFM surface potential measurements on the very same fibrils to test for changes in surface charges. In order to produce direct, interlinked evidence for the effects of glycation, we prepared two separate slides with fibrils from the same rat tail tendon, from the same fascicle and used one of them as a control group. Ten (10) individual fibrils were then chosen from each slide and the very same fibrils were then measured on the same spots with the two techniques described above *before and after* the glycation step. This allowed us to

do *paired* statistical testing on each fibril, leading to high powered results, along with a control group to compare the observed changes to.

## Structure of this Thesis

In chapter 2 a brief introduction to the general topic of collagen is given, followed by an overview of the general working principles of the two measurement methods used in this study. In chapter 3 the design for the glycation study is presented comprehensively, starting with the general work-flow, schedule and sample preparation, then going into detail on the indentation and surface charge experiments and statistical analysis. Chapter 4 is a stand-alone segment dealing with the work that has been done on the determination of the contact point in AFM force spectroscopy. First, a short introduction to the topic is given, followed by a presentation of a few state-of-the-art methods. Deep convolutional neural networks are then briefly introduced as a machine learning technique and the architecture and training of the network designed in this work are presented. The section closes with the evaluation of the new technique, comparing results to two other methods. Results of the glycation study are presented in chapter 5 showing changes in the fibrils indentation modulus, surface potential and their dry and hydrated diameter. They are then discussed and interpreted in chapter 6 followed by a final conclusion on the present and future relevance of this work in chapter 7.



Die approbierte gedruckte Originalversion dieser Diplomarbeit ist an der TU Wien Bibliothek verfügbar.  
The approved original version of this thesis is available in print at TU Wien Bibliothek.

## 2. Background

### 2.1. Collagen

Collagen is the most abundant and arguably most important structural protein in (but not exclusive to) mammals contributing  $\sim 30\%$  of the protein mass [1]. It is most prominently found in load-bearing tissues like bones, tendons, ligaments, cartilage or dentin but to a lesser extent also plays a vital role in many other organs like the skin, blood vessels, general connective tissues, muscle or the cornea of the eye [2]. Beneath its structural role in the shape, mechanics and organization of the extracellular matrix it also interacts with cells via several receptor families to regulate their proliferation, migration and differentiation [1]. The collagen superfamily comprises 28 different types with collagen type I being the most abundant contributing around  $\sim 90\%$  of the total collagen mass. Type I is the main collagen constituent in skin, tendons, vascular vessels and bone.

Typical for organs made primarily out of fibrillar collagen are the emergent multiscale, in part self-similar, hierarchical structures as shown in figure 2.1 for tendon.

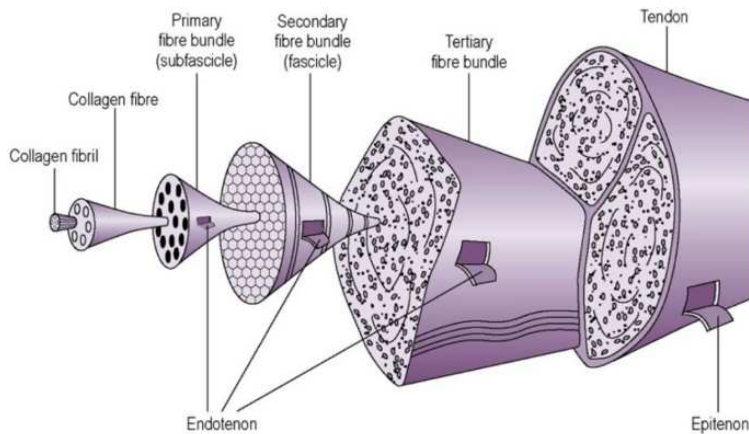


Figure 2.1.: Typical multiscale hierarchical structure found in tendon. [33]

### 2.1.1. Structure

The basic chemical make-up of a single collagen polypeptide chain is characterized by a repeating amino acid motif of  $(Gly - X - Y)_n$  where Gly is glycine and X or Y are other amino acids, most commonly proline, alanine, hydroxyproline or glutamic acid. Each polypeptide molecule has the form of a left handed chain. Three of those chains together form a right handed triple helical superstructure, also called tropocollagen, where the glycine side chains usually face inwards in an aqueous environment due to their hydrophobic nature, while the X and Y amino acids side chains mostly determine molecular interactions with the environment.[34]

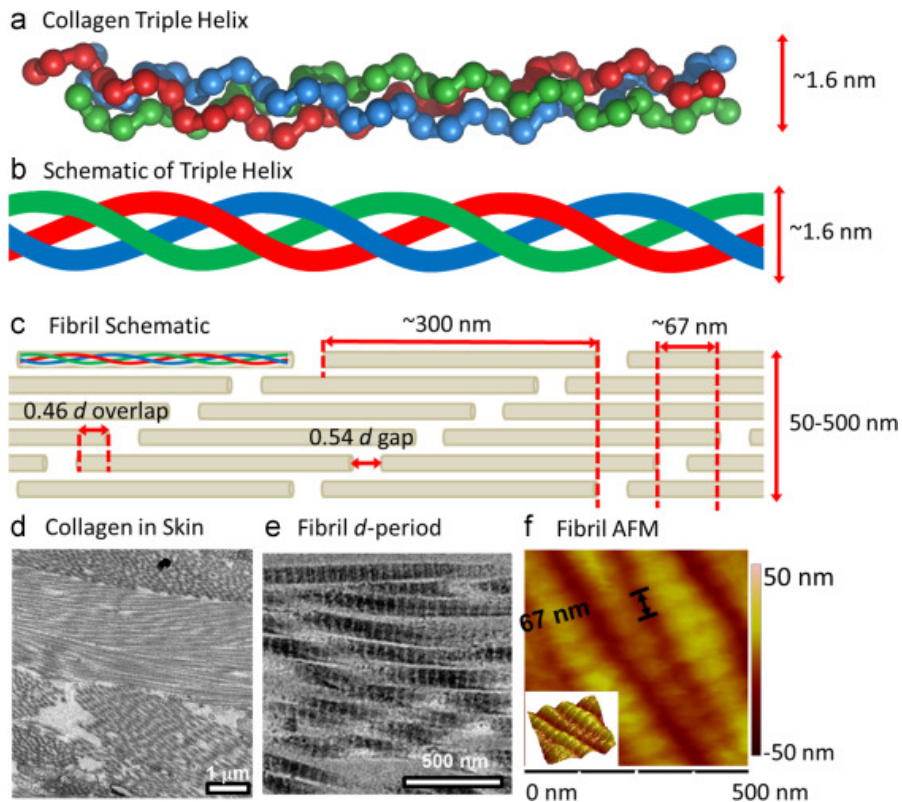


Figure 2.2.: Sub-micrometer hierarchical structure of collagen. (a) and (b) show how three left handed polypeptide chains form the right handed triple helix, while (c) illustrates how these typically 300 nm long triple helices arrange themselves into fibrils by stacking in a staggered manner creating regions of full overlap followed by gap regions leading to the typical d-banding period of  $\sim 67 \text{ nm}$  as seen in (e) and (f).[34]

Tropocollagen is typically found to have a length of  $\sim 300 \text{ nm}$ , most of which

is found in the above described triple helical domain, while its tail ends, called telopeptides, show a more disorganized, less twisted structure. The tropocollagen arranges into fibrils stacking in a staggered manner, where there is a small gap of around  $\sim 36 \text{ nm}$  between neighbouring (tail to tail) molecules that, together with the staggered stacking, lead to the so called d-banding pattern (see fig. 2.2), a periodically alternating pattern between gap and overlap regions with an overall period of  $d \approx 67 \text{ nm}$ .

The resulting fibrils vary widely in diameters between  $50 - 500 \text{ nm}$  and are themselves arranged into larger fiber bundles held together by a matrix of proteoglycans, heavily glycosylated proteins, as seen in figure 2.3.[34][35]

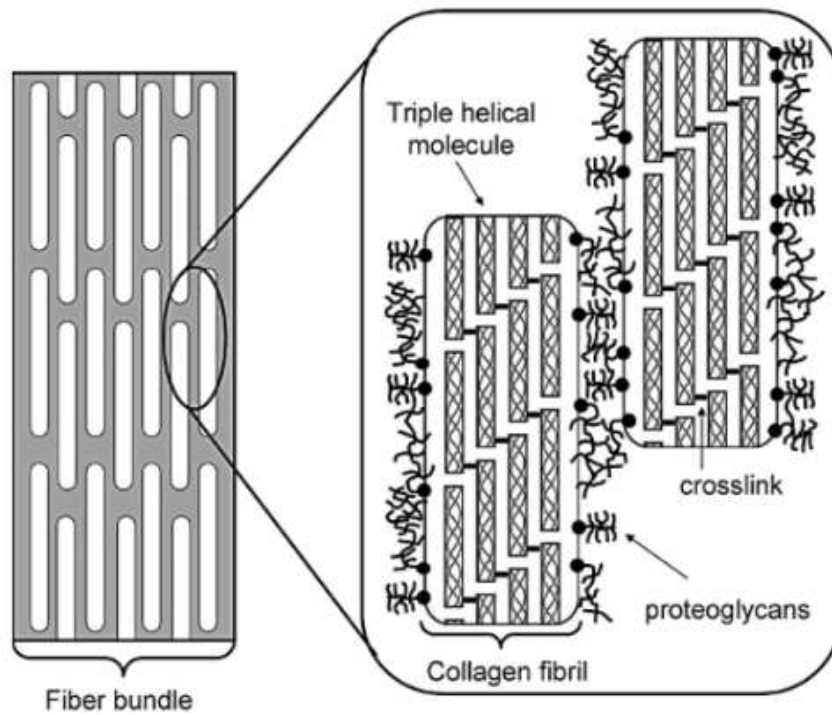


Figure 2.3.: Fiber formation through embedding of collagen fibrils in a matrix of usually highly hydrated proteoglycans.[2]

The biosynthesis of collagen is a complex process that starts with the formation of procollagen in the ribosomes, followed by the formation of the typical triple helix. The molecule is mainly stabilized through the hydrogen bonds formed during hydroxylation of proline and hydroxyproline. The procollagen triple helices then get transported out of the cell in vesicles through the Golgi apparatus. During this transportation the removal of the procollagen propeptides occurs.

Fibril formation is a self-assembly process that mainly takes place in the extra-

cellular matrix, though some research hints at intracellular formation [36]. Once formed, fibrils are subsequently stabilized by enzymatic covalent bonds, formed at the telopeptide of one tropocollagen molecule and linking to the helical domain of a neighbouring one [34][5].

In addition to covalent bonds, it is well established that hydration also plays a major role in structure and mechanics of fibrils. Collagens have many donor and acceptor sites for H-bond formation and are therefore able to keep structurally bound  $H_2O$ , even when fully dried. If submerged in PBS at physiological pH 7.5, fibrils can swell up by a factor of 1.5-2 in diameter compared to their fully dried state (see figure 5.6). This is because of water's high dielectric constant, effectively reducing overall free energy when accumulating in intrafibrillar spaces between tropocollagen molecules. Andriotis et al. (2018 [37]) have tested mechanical differences in fibrils at varying hydration levels by tuning intrafibrillar water content through external osmotic pressure. An up to 24-fold difference in nanoindentation stiffness and a 6-fold difference in tensile stiffness were found between the most extreme states of (de)hydration.

### 2.1.2. Mechanics

The mechanics of collagenous tissues are complex and largely determined by the hierarchical interplay of its individual constituents at different length scales. Arrangement of fibrils and fibers can vary vastly from tissue to tissue at the macroscale and lead to a wide range of mechanical properties, while properties of fibrils themselves can also vary significantly between the different known types of the collagen superfamily.

Parallel orientation of highly aligned fibers and fibrils in tendon and bone, for example, can lead to transverse isotropic behaviour in both, while both materials still have very different mechanical responses to loading due to the fact that bone is mineralized. Skin on the other hand shows a less oriented, less aligned arrangement of collagen fibers leading to it almost having no initial stress response to applied strains, because the fibers get re-oriented before they contribute to the tissue's mechanical response. Figure 2.4 illustrates the striking difference in the order of magnitudes between the three materials with an elastic modulus in the linear domains of the stress-strain curves of  $E_{Bone} \approx 20 \text{ GPa} > E_{Tendon} \approx 1 \text{ GPa} > E_{Skin} \approx 50 \text{ MPa}$ . What most collagenous tissues have in common, though, are their highly non-linear and, related to high hydration, viscoelastic behaviour. Bone and dentin are the exception because of their mineralization with hydroxyapatite, leading to overall stiffer and less tough tissues.[2][34]

At the nanoscale, meaning at the fibril level, mechanical response largely depends on the initial straightening of the kinks in tropocollagen molecules caused by the additional lateral freedom in the gap regions (toe region, see fig. 2.5 green



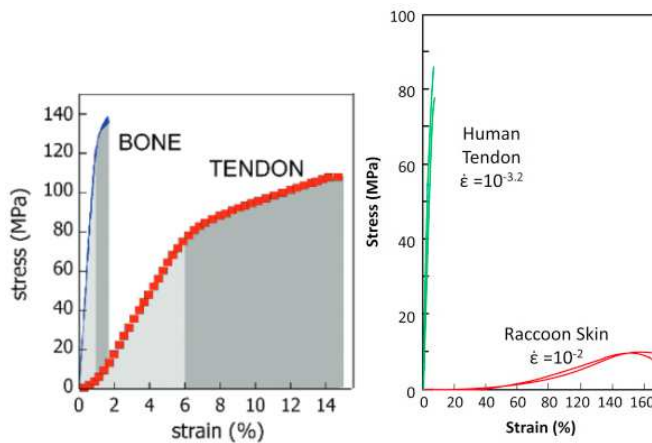


Figure 2.4.: Stress-strain curves for tendon-vs-bone (left) and tendon-vs-skin (right) illustrate the vast range of properties of collagenous tissues. Note for example how the ultimate strain of bone lies around 2%, while skin doesn't even show any significant stress response up until 50% strain.[34][2]

arrows), followed by a linear region dominated by the molecular sliding between molecules, a not yet well understood mechanism in part also involving the covalent bonds between molecules [38]. The ultimate strength of fibrils has been shown to depend on the amount of covalent bonds [39]. Figure 2.5 illustrates typical stress-strain curves of individual fibrils in tensile tests.[2]

There has been a number of different studies exploring the mechanics of individual collagen fibrils. Atomic force microscopy (AFM, see section 3.1.2) has been very popular in these studies, given its many different probing techniques: AFM nanoindentation can be used to determine radial indentation moduli of fibrils in air [41][42][43][44][45][46] (reported moduli between 1 and 12 *GPa* in unmineralized fibrils) as well as in more physiological environments such as PBS [42][47][43][48][49][50] (reported moduli between 0.5 and 200 *MPa* among others depending on indentation speed, salt concentration in solution, osmotic pressure) non destructively; a drawback is the fact that radial loading is not the main loading type that fibrils experience *in vivo*. AFM-based tensile tests, however, have also been done in air and liquid [40][51][52] and can test for more relevant properties like tensile modulus and whole stress-strain curves up until fibril failure. To the techniques detriment, fibril preparation is time consuming though and destruction of the specimen is unavoidable. Microelectromechanical systems (MEMS) have similar advantages and disadvantages, with even more effort needed during preparation [53][52]. A recent advancement in AFM mechanical testing have been

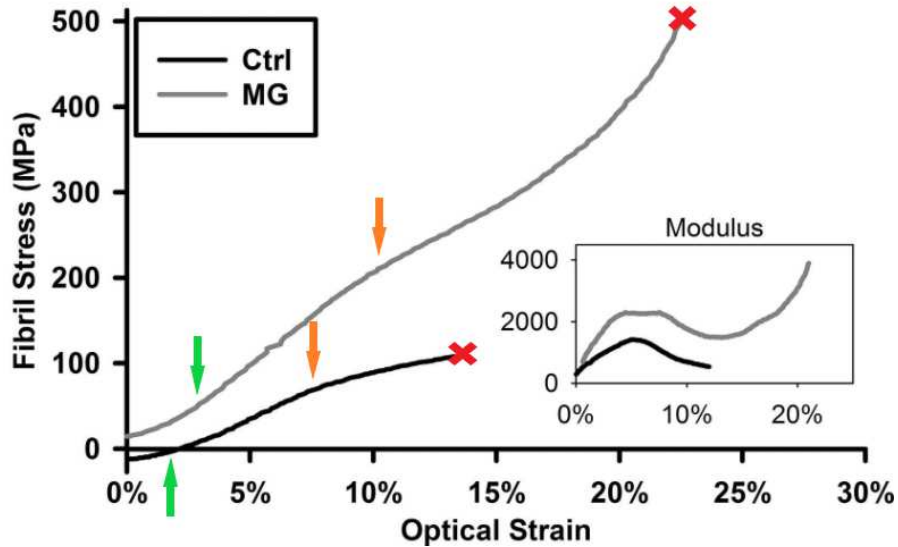


Figure 2.5.: Individual fibril nanotensile tests (load to failure) done on rat tail and achilles tendon by Svensson et al. 2013 [40]. The black curve depicts the stress-strain relation of an untreated fibril from a control group, while the gray curve's fibril was treated with methylglyoxal (MGO) leading to AGE cross-links (see Section 2.1.3). The green arrows depict the transition from the toe region to the linear region and the red crosses mark fibril failure. The orange arrow in the control fibril marks the yield point, with the curve overall showing a two phase behaviour. In the gray curve it marks the onset of a distinct third phase, that was mainly found in treated fibrils, but also in untreated ones with high ultimate strength.

bowstring experiments [54][55][56], first proposed by Quigley et al. (2016 [57]), where fibril sections are fixated on both ends with epoxy resin and then strained to failure by laterally pulling them with the AFM cantilever tip. Even though this technique does not produce stress-strain curves, it allows for easy post and pre failure testing with other mechanical/imaging methods. Optical fibril properties, such as fibril alignment, D-banding period or growth of mineral crystals in collagen from bone or dentin, have been extensively tested via small angle X-ray scattering (SAXS) [58][59][60][61].

### 2.1.3. Glycation

In addition to enzymatic cross-linking, which happens predominantly in the early life cycle after collagen biosynthesis, there are also non-enzymatic cross-linking mechanisms known to occur in collagen. These are subsumed under the umbrella term glycation. The resulting covalent cross-links are called advanced glycation end products (AGEs). Non-enzymatic glycation is mainly connected to the Maillard reaction, a complex chemical reaction cascade based on the interactions of free amino groups in proteins with reducing sugars, as shown in figure 2.6. The Maillard reaction starts with the formation of a reversible Schiff base between a carbohydrate and the functional groups of lysine or hydroxylysine, predominantly, over the span of hours followed by the Schiff bases transitioning into more stable keto-amines, called Amadori products. From there on, over the span of weeks to even years, in a not yet well understood series of reactions, the metabolic glycolysis of these products leads to a wide range of by-products, including methylglyoxal (MGO), the cross-linking agent used in present work, that can then form AGEs in extracellular proteins.[5][62][6]

The glucose-derived AGE cross-link glucosepane is thought to be the most common species found in-vivo. Two MGO-derived crosslinks, MODIC and MOLD, have also been found in-vivo, though at lower concentrations than glucosepane. While MODIC and glucosepane are both lysine-arginin cross-links, MOLD forms between two lysines.[20][63][64][65]

AGEs are believed to play a central role in tissue deterioration during ageing and in metabolic diseases, such as diabetes. Their presence in collagenous tissues is believed to affect them in two ways; mechanically and biologically, regarding cell interaction [5]. At the macroscale, tissues with high amount of AGEs show little variation in stiffness, but diverge greatly from less non-enzymatically cross-linked tissues in their viscoelastic properties, their denaturation temperature and their mode of tensile failure, as can be seen in figure 2.7. At the nanoscale of collagen fibrils, however, stiffness is believed to significantly increase through glycation.[5]

The biological effects of AGEs are closely related to cell interaction with the extracellular, collagen rich matrix. Disrupted intermolecular recognition between

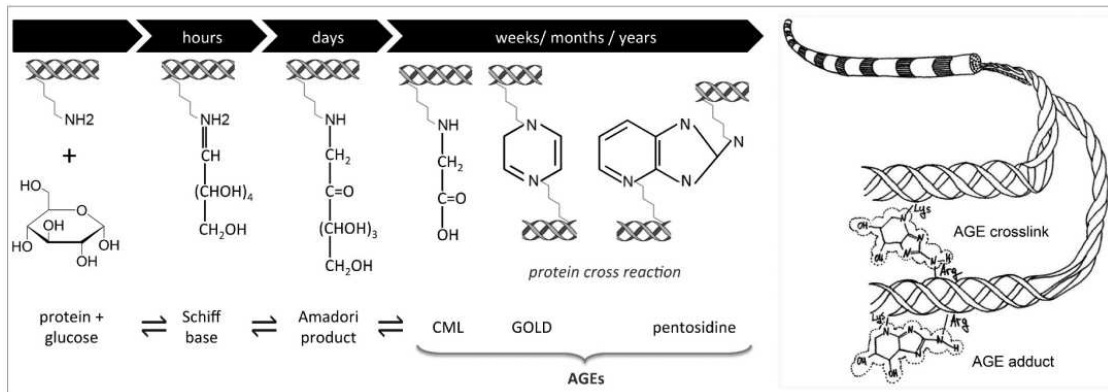


Figure 2.6.: Schematic of the sequence of chemical reactions (left) that lead to AGE adducts or cross-links, in this case pentosidine, in collagen (right). [5]

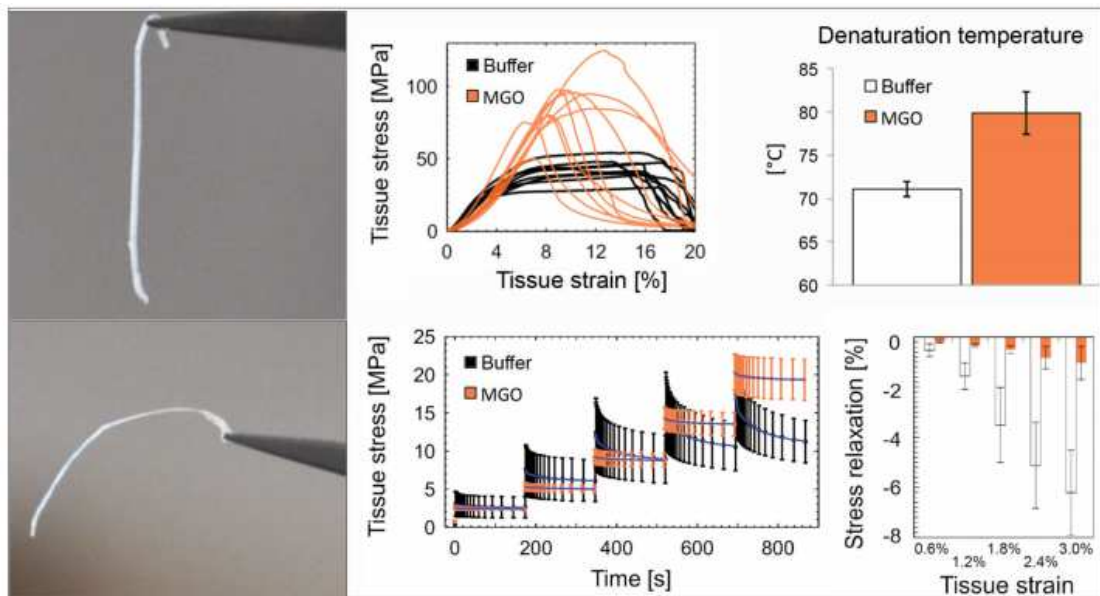


Figure 2.7.: Rat tail tendon before (top left) and after (bottom left) glycation. The tissue shows decreased stress relaxation (bottom two graphs), as well as increased denaturation temperature (top right) and altered mode of tensile failure (top middle). (Snedeker et al. 2014 [5])

amino groups and cell integrins, but also proteoglycans and certain enzymes (e.g. collagenases) have been hypothesised to attribute to decreased cell adhesion, migration, collagen turnover and wound healing, while being linked to inflammation. [5][10][28][9]

## 2.2. Atomic Force Microscopy

Atomic force microscopy (AFM) is a versatile imaging technique based on 'feeling' a sample as opposed to 'seeing' it, as it is the case in e.g. light or electron microscopy, that involve some sort of light/particle source that, guided by arrays of lenses, reflect from or get transmitted through a sample.

AFM makes use of a cantilever with a tip attached to its end, that interacts with the sample through direct physical contact (mostly Pauli repulsion) in some operating modes, and through several overlaid short range forces in others (see explanations of different modes below).

The cantilever acts as a simple spring with spring constant  $k$ , such that the force between tip and sample can directly be related to the cantilever deflection, which in the AFMs used in this work is measured by a laser beam focussed on the end of the cantilever and reflecting off its surface onto an array of four photodiodes (see fig. 2.8). From the combined voltage signal from the diodes, the normal  $F_N$  and lateral  $F_L$  forces can be determined, amplified, processed by a digital signal processor (DSP) and ultimately fed to the controller software, that can in response adjust movement at the piezoelectric actuators, that drive cantilever position relative to the sample. The control feedback loop is usually operated at a fixed clock rate, in modern systems up to 100  $kHz$  and higher, where the control response is based on a proportional and an integral correcting term (PI-Feedback). A common AFM setup is shown in figure 2.8.[66]

In the liquid AFM system used in the nanoindentation measurements this study the cantilever is the part being moved by the piezoelectric actuators, while the sample stays still, submerged in a liquid cell. The liquid-air interface can be perturbed by surface waves resulting in an unsteady laser signal at the detectors, as illustrated in figure 2.9 (A). This can be mitigated by mounting the cantilever to a glass block cantilever holder, that is itself submerged in the liquid (fig. 2.9 (B)). The laser is then channelled through the stable liquid-glass interface.

An AFM can be operated in several modes, that can be generally classified as static or dynamic. Contact mode (CM-AFM) is a static and historically first used operation mode for AFM. It works by bringing the cantilever tip into direct contact with the surface, applying a constant setpoint force, which is then the variable that is to be kept constant by the PI feedback loop. While in contact, the tip is then moved in a grid-like pattern over a selected area and the recorded cantilever head

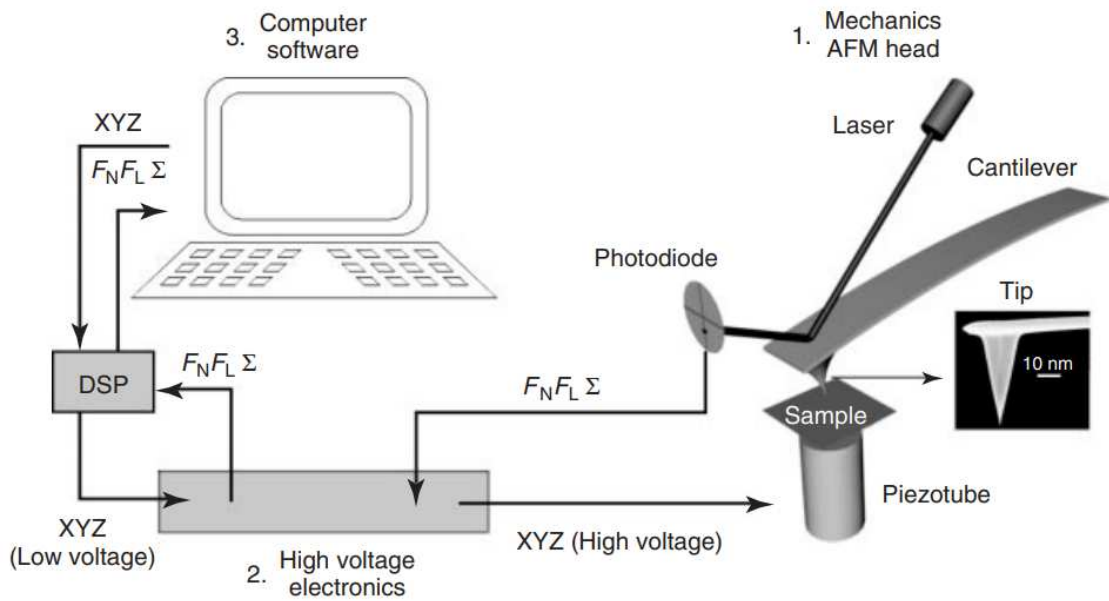


Figure 2.8.: Basic setup for a standard AFM device. Note that in liquid AFM the *cantilever* is usually the part that is actively moved over the sample by piezo elements. [66]

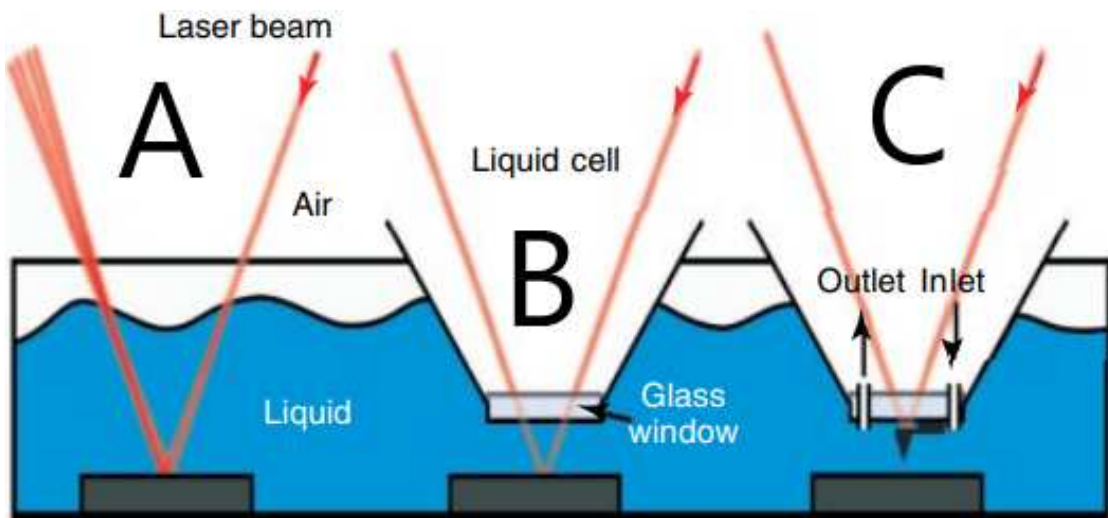


Figure 2.9.: Laser interaction with the liquid-air interface (A) can be bypassed by submerging a glass window into the liquid cell (B), which usually holds the cantilever and can have additional inlets and outlets for liquid exchange (C). [66]

height produces a 3D image of the sample topography. Additionally other sample properties can be explored through the lateral cantilever deflection, giving a measure of tip-to-surface friction.

The dynamic operation modes can be distinguished mainly by the signal, that is used in the feedback loop. Another distinction can be made between intermediate and non-contact operation, where the tip has temporary or no contact to the sample surface.

In amplitude modulated AFM (AM-AFM) the cantilever is being externally driven at a fixed frequency  $f_0$  slightly below its resonance frequency  $f_R$ , while scanning over the sample surface. When the cantilever oscillates freely, without the sample surface in its vicinity, the drive frequency will produce a fixed amplitude  $A_0$ . As soon as the tip comes near (non-contact mode) or temporarily touches (intermediate mode) the sample surface, the amplitude  $A$  decreases because of sample to tip interactions. Using this, one can choose an amplitude setpoint, at which the feedback loop then tries to keep the amplitude at, thereby keeping the tip at a constant distance to the surface. An example image recorded in this mode can be seen in figure 2.11.

The other basic variant of the dynamic modes is the frequency modulated AFM (FM-AFM), which works very similarly except for the fact that the drive amplitude is now constant and the shift in frequency relative to the free oscillation frequency is controlled by the feedback system. [66][67]

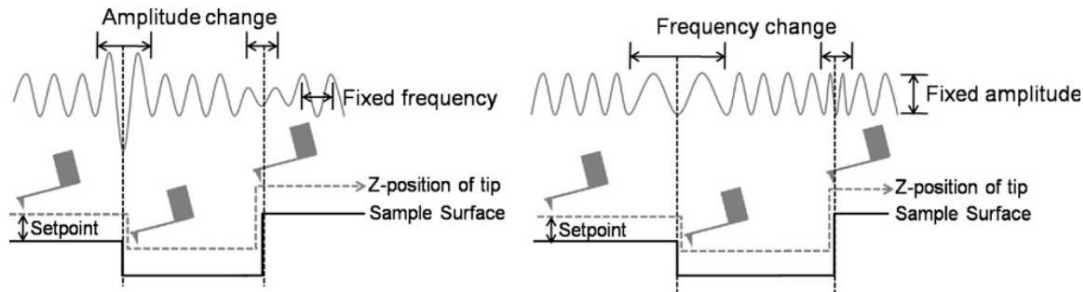


Figure 2.10.: Illustration of the working principles of AM-AFM (left) and FM-AFM (right) [67]

### 2.2.1. Force Mapping Principles

The force mapping mode can be understood as a quasistatic imaging mode, where the main focus lies not on the topological make-up of the sample, but its mechanical properties. As a form of force spectroscopy, it is essentially a series of



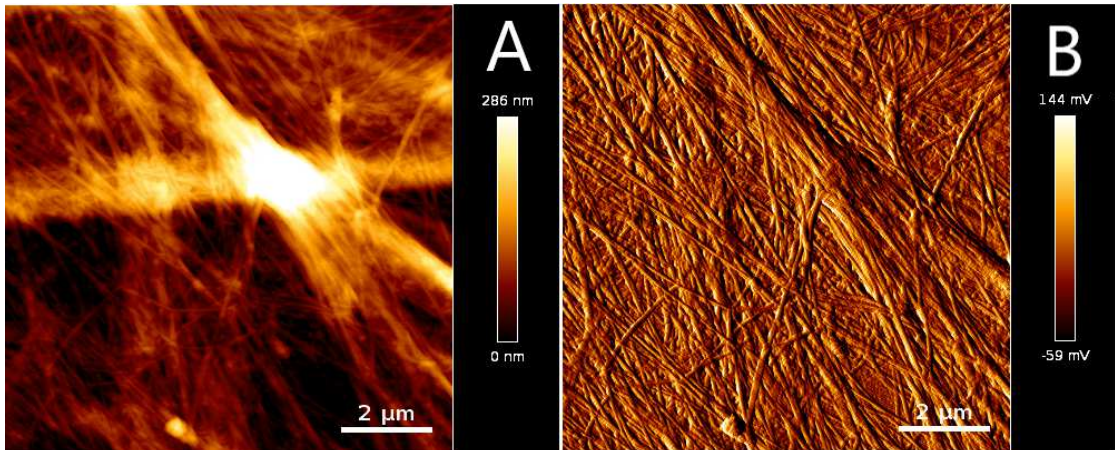


Figure 2.11.: AC-mode AFM image of a mesh of collagen fibrils from mouse tail tendon recorded during a pre-trial experiment. (A) is the height map, showing the overall profile, and (B) the error signal, highlighting more local features.

nanoindentations in a grid-like pattern, where the tip is pressed into the sample in a fully vertical motion, just moving between grid points when the tip is not in contact. A typical force map of a collagen fibril from mouse tail tendon in liquid is shown in figure 2.13.

To truly understand the force curves obtained from force mapping, there is a myriad of complex tip-sample interactions, some relevant only in air, some only in liquid, some in both, to be accounted for.

Most importantly, there is the interaction of the tip with the bulk material of the sample when pressing into it, which is the quantity that is usually sought after in indentation experiments. A reliable method to decouple this interaction from the other tip-sample forces is discussed in section 3.1.2.

The most important non-bulk interaction in air are the capillary forces that are exercised by a small water layer on the sample surface, caused by ambient humidity, that lead to the sudden snap-in effect during approach of the tip, by building a water meniscus between tip and sample (see Fig. 2.12). They also cause tip adhesion to the sample surface when withdrawing the tip (fig. 2.12 (a)). They can be partly eliminated by controlled low humidity environment but completely disappear, when both tip and sample are fully submerged in water (fig. 2.12 (b)).

The van-der-Waals force (vdW) is a relatively long-range attractive force, that is felt by the tip in air as well as in liquid and is caused by induced dipoles. Its potential shows a  $\propto 1/z^6$  relationship to the distance  $z$  and is relatively weak



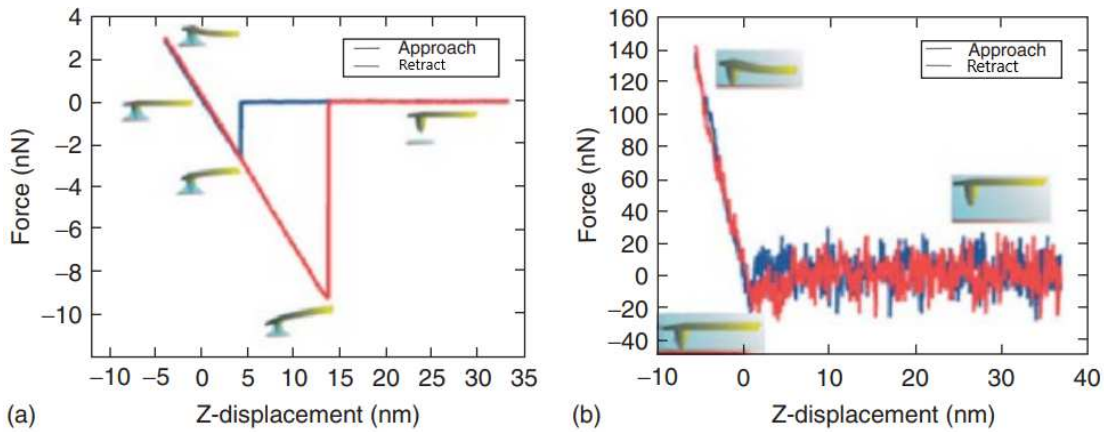


Figure 2.12.: Force curves obtained on mica in air at ambient conditions (a) and in PBS buffer (b). The main attractive force in ambient air are the capillary forces between tip and a liquid layer on the sample surface, forming a meniscus that leads to the sudden snap-in effect during approach and keeps the tip attached during retraction. [66]

compared to other forces discussed here. The Lennard-Jones-Potential  $V_{LJ} = \epsilon \left( \left( \frac{r_m}{z} \right)^{12} - 2 \left( \frac{r_m}{z} \right)^6 \right)$  is a common approximation for the intermolecular potential between otherwise chemically unbound, neutral atoms or molecules. It subsumes the vdW potential  $\propto 1/z^6$  with the Pauli repulsion potential  $\propto 1/z^{12}$ ,  $\epsilon$  and  $r_m$  being fitting parameters representing the depth of the potential well and the distance of its deepest point, respectively.

Another long range force is the one caused by the electrostatic double layer of counterions that builds up when a dielectric liquid comes into contact with a either positively or negatively charged solid surface.

Other, less important and small range forces are among others steric, hydrophobic or solvation forces. [66]

## 2.2.2. Kelvin Probe Force Microscopy

In Kelvin probe force microscopy (KPFM) the contact potential difference  $V_{CPD}$  between a conducting tip and the sample is measured. For conductive samples it is defined as

$$-eV_{CPD}(x, y) = \Phi_{tip} - \Phi_{Sample}(x, y) \quad (2.1)$$

where  $\Phi_{tip}$  and  $\Phi_{Sample}$  are the potential differences between the respective material's Fermi levels  $E_F$  and the vacuum energy level  $E_V$  (Fig. 2.14 (a)) and  $e$  is the electron charge. Figure 2.14 illustrates the electronic energy levels of the tip-sample system in three states: If sample and tip are brought into conductive contact (Fig. 2.14 (b)), a current builds up to negate the differences in Fermi levels of the two materials, but thereby leaving an effective charge on them, which in turn leads to a potential  $V_{CPD}$ . By applying a DC-voltage  $V_{DC} = V_{CPD}$  to the tip, the net charges can be nullified (Fig. 2.14 (c)).[67]

To translate these effects into measurable quantities using the standard AFM setup, an AC voltage  $V_{AC}$  is applied to the cantilever at a frequency  $\omega$  slightly below resonance. The cantilever will then feel an electrostatic force

$$F(z) = -\frac{1}{2}\Delta V^2 \frac{\partial C(z)}{\partial z} \quad (2.2)$$

with  $\frac{\partial C(z)}{\partial z}$  being the gradient of the capacitance between tip and sample with respect to the tip height and

$$\Delta V = (V_{DC} - V_{CPD}) + V_{AC} \sin(\omega t). \quad (2.3)$$

By inserting eq.2.3 into eq.2.2 and expanding the square, eq.2.2 can be divided into three parts, differing in their frequency dependency:

$$F = F_{DC} + F_{\omega} + F_{2\omega} \quad (2.4)$$

with

$$F_{DC} = -\frac{1}{2} \frac{\partial C(z)}{\partial z} (V_{DC} - V_{CPD})^2 \quad (2.5)$$

$$F_{2\omega} = -\frac{1}{2} \frac{\partial C(z)}{\partial z} V_{AC}^2 \sin^2(\omega t) = \frac{1}{4} \frac{\partial C(z)}{\partial z} V_{AC}^2 (\cos(2\omega t) - 1) \quad (2.6)$$

$$F_{\omega} = -\frac{\partial C(z)}{\partial z} (V_{DC} - V_{CPD}) V_{AC} \sin(\omega t) \quad (2.7)$$

A lock-in amplifier can then be used to just detect cantilever vibrations at  $\omega$ . As is usual for lock-in amplifiers, it outputs a DC-signal directly proportional to

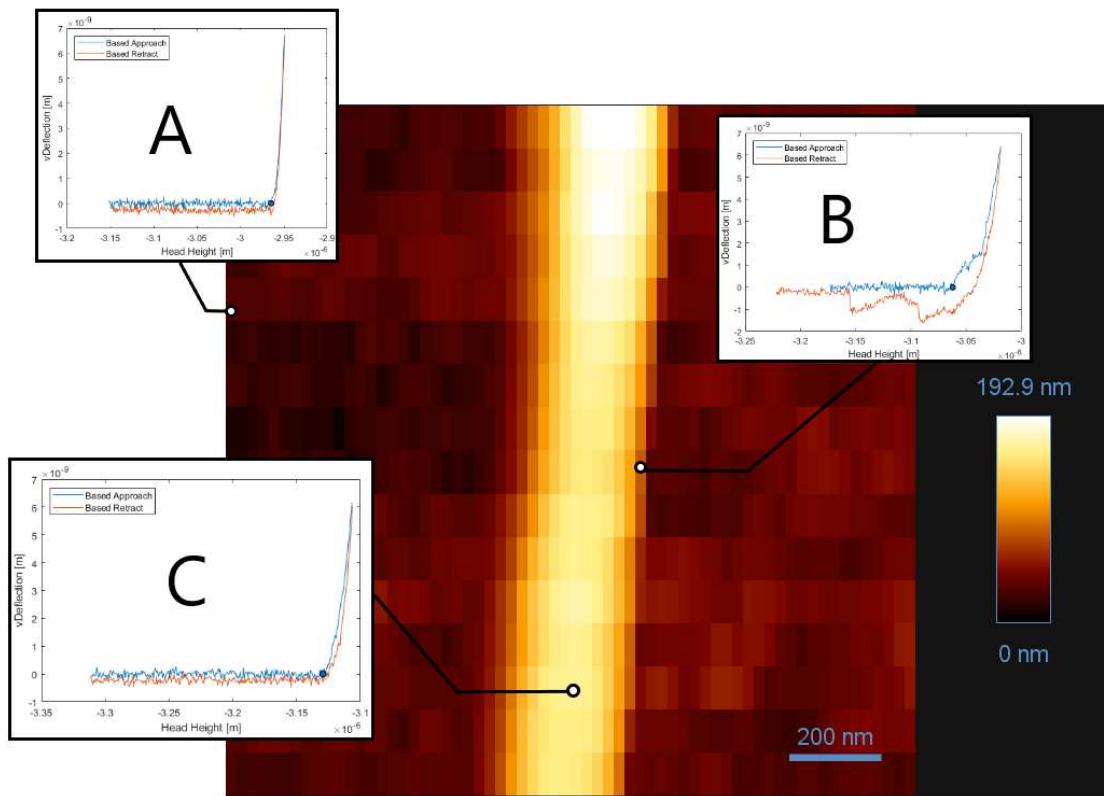


Figure 2.13.:  $6 \times 6$  pixel force map on an individual mouse tail tendon fibril overlaid with selected pixel's indentation force curves. (A) is a force curve from the glass slides surface. Its HeadHeight-vs-vDeflection slope is close to 1 and loading and unloading curves look almost identical due to the glass being a highly linear elastic material, showing little to no viscoelastic effects. (B) comes from the fibril edge: due to the steep topography cantilever tip slip-off events are very common as can be seen in the approach curve after initial contact. The unloading curve shows greater stiffness than the loading curve due to the fibril being a highly viscoelastic material. Also, the unloading curve shows events of molecular unfolding, an effect that happens when long chained molecules - usually proteoglycans on the surface of fibrils - attach to the tip creating a downward pulling force when it separates from the sample. (C) is a force curve from the apex of the fibril: there is no slip-off or molecular unfolding events to be seen, but viscoelasticity is observable between the loading and unloading part.

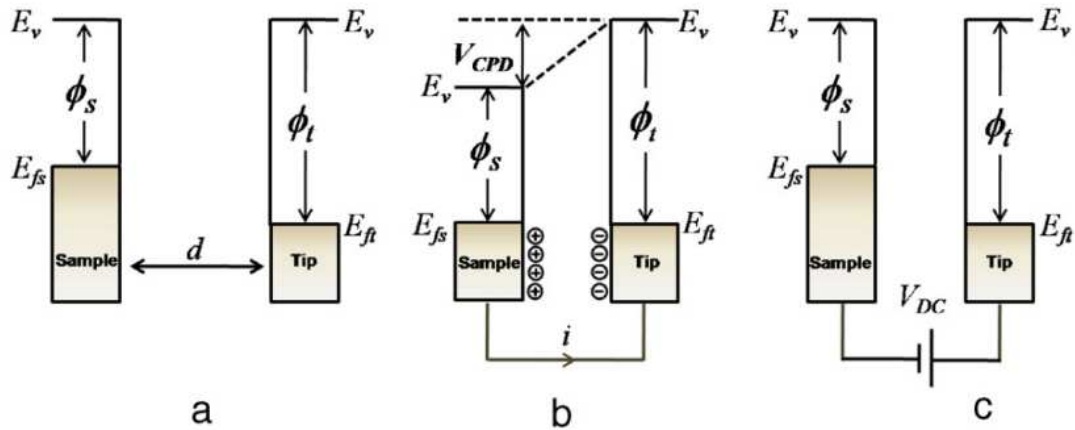


Figure 2.14.: Three states of the tip-sample system. (Description in full text body)[67]

the amplitude of the  $\omega$ -portion of the input AC-signal from the photodiodes. This signal can then serve as error signal for the feedback loop, which keeps adjusting the voltage  $V_{DC}(x, y)$  to nullify the amplitude of the  $\omega$ -vibration to zero, across all surface points  $(x, y)$  accordingly.  $V_{DC}$  is then equal to  $V_{CPD}$ .

For nonconductive materials like biomolecules, their effective surface potential can still be derived, by placing them on a conductive sample holder with constant fermi levels everywhere  $V_{CPD}(x, y) = V_{CPD}$  (fig 2.15 (C)). The equations above still apply, but the contact potential difference  $V_{CPD}$  is instead expanded by the biological sample's surface potential  $\Phi(x, y)$  deriving from fixed charges on the molecule's surface, leading to  $V'(x, y) = V_{CPD} + \Phi(x, y)$ . [67]

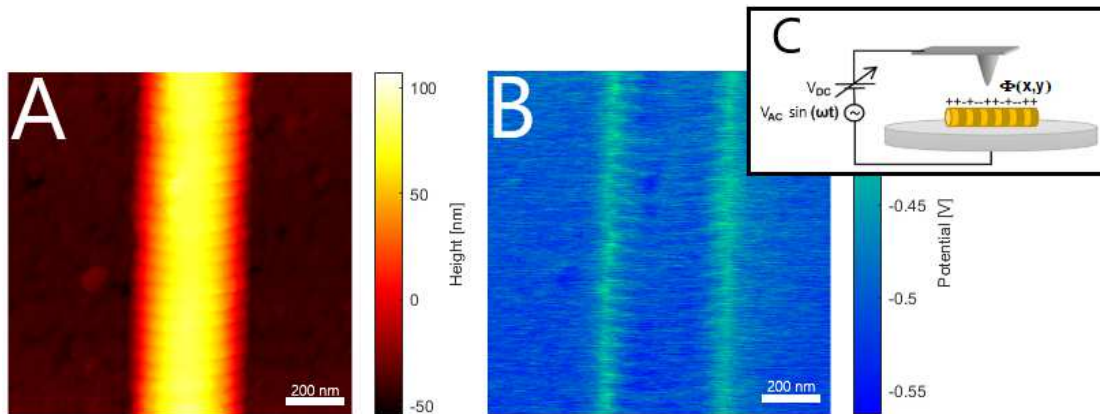


Figure 2.15.: KPFM surface potential map of an individual fibril from mouse tail tendon recorded in interleave mode. (A) is the height map and (B) is the surface potential map. At the edges of the fibril in (B) typical edge effects, caused by the cantilever tip's small horizontal distance to the sample surface, can be seen. (C) Schematic of the KPFM setup for non conducting samples, in this case collagen fibrils, with fixed surface charges leading to a surface potential  $\Phi(x, y)$  [30]



Die approbierte gedruckte Originalversion dieser Diplomarbeit ist an der TU Wien Bibliothek verfügbar.  
The approved original version of this thesis is available in print at TU Wien Bibliothek.

# 3. Materials and Methods

## 3.1. In Vitro Glycation of Collagen Fibrils

### 3.1.1. Sample Preparation and Experiment Work-Flow

Tail tendon from one 5 month old wild type male mouse was used for the experiments described in this thesis. The already severed tail was stored frozen at  $-84^{\circ}\text{C}$ . For sample preparation, the severed tail was skinned by first making a small incision along the tail length at the proximal end of the tail with a scalpel, then skinning it by hand and with the help of tweezers. Out of the so exposed tail tendons an approx. 1-2 cm long section was obtained by making careful incisions above and below the chosen section and then separating it from the tail, inserting and sliding fine tweezers between tendon and underlying muscle. The tendon was then washed thoroughly with deionized water to get rid of unwanted cellular material.

From this point on, the material was to be kept in a hydrated state, applying drops of deionized water, since handling turned out to be much easier this way. The tendon section could now be further broken down into its fascicles and fibers with fine tweezers and cut into pieces of a few millimetres of length with a scalpel. These sections of, ideally, single fibers could then be deposited on conventional soda lime glass microscope slides (Marienfeld, Königshofen, Germany [68]).

The deposition of fibers is arguably the most important step during preparation and was done under a low-magnification stereo microscope using two very fine tweezers. Once the fiber was placed on the slide it was carefully broken apart by the tweezers tips and 'smeared out' on the glass in a single continuous motion, exposing individual fibrils, results can be seen in figure 3.1. The amount of mechanical manipulation in this step was to be kept at a minimum in order to not damage the fibrils. Additionally, this step needed to be carried out swiftly since the small fiber sections, especially after being broken up, tend to dry out very quickly and dried out fibrils tend to not adhere to the glass surface or break during manipulation.

For the subsequent study, two separate slides were prepared from the same mouse and same section of fascicle, one for the test group and one for the control group.

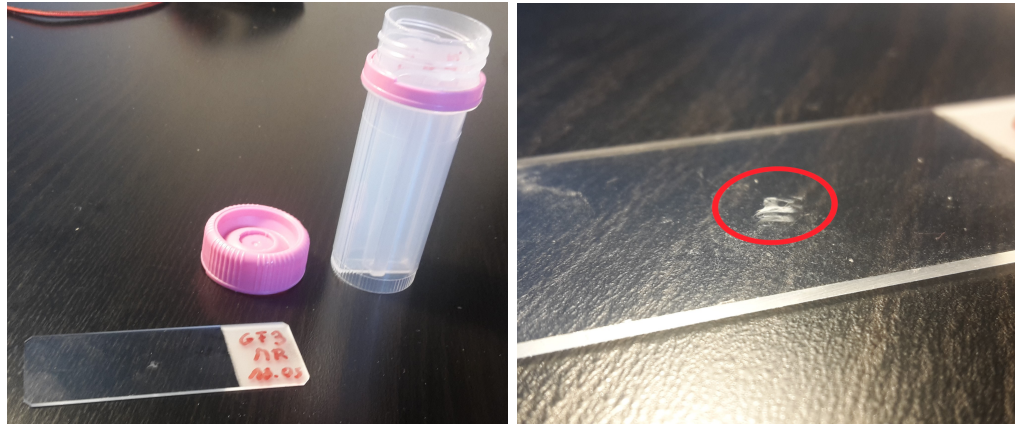


Figure 3.1.: Standard glass slide holding the smeared out tendon section (circled in red on the right) beneath a seal-able plastic tube, similar to the ones used for MGO/PBS-incubation(left picture).

Once the fibrils were deposited on the two microscope slides, they were once more carefully washed in deionized water and then placed in a buffer solution containing 10mM/L of PBS (Phosphate Buffered Saline) (Sigma-Aldrich, St. Louis, MO, USA [69]) and 5mM/L of EDTA (Ethylenediaminetetraacetic Acid) at 34°C for 2 hours, where EDTA takes the function of binding metal ions that can potentially catalyse metallo-enzymatic denaturation processes in biological tissues [70]. This incubation step was deemed necessary because it has previously been shown in another ongoing study that fibril indentation modulus increases over time when incubated in a buffer solution [50]; the effect flattens out after about 2 hours of incubation. The slides were afterwards stored in a low vacuum desiccator (VWR International, Radnor, PA, USA [71]) (see fig. 3.2) for at least a full day to completely dry out for the following measurements.

The AFM and KPFM measurements themselves (section 3.1.2 and section 3.1.3) were spread out over 3 days, with the hole experiment spanning 8 days including the preparation and initial desiccation day (see fig. 3.4). The first measurement day was reserved for just the pre-incubation Kelvin Probe AFM (KPFM) measurement followed by a 6 day desiccation period, due to scheduling restrictions; A minimum of 24 hours of desiccation between experiments were set for this study, as it was believed to be enough time for the dehydration process to plateau. As a potentially crucial study design decision, both AFM nanoindentation measurements, the one before, and, the one after incubation, were scheduled to be done on the same day, which implies that incubation in MGO and control buffer,





Figure 3.2.: Low Vacuum Glass Desiccator [71] used to dry out collagen fibrils on microscope slides at multiple points in the experimental process before and between measurements. The vacuum is applied at the upper valve by an external vacuum pump.

respectively, was to be done in between these measurements and on that same day. This was done in order to mitigate an additional drying and rehydrating step, for both nanoindentation measurements (before and after incubation with MGO/control buffer) were taken in a hydrated state using a fluid cell. In this case this was a 3D-printed ring of  $\sim 0.5$  cm in height and a diameter about as wide as the glass slides (see fig. 3.3). The ring was glued on to the slides with a two-component silicone adhesive and then filled with PBS.

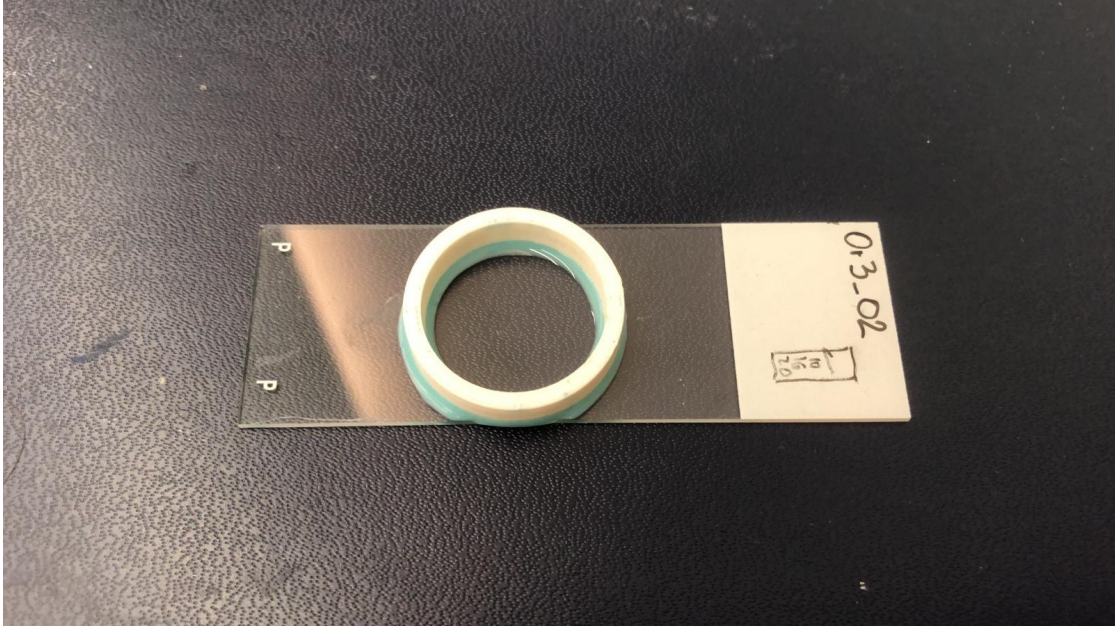


Figure 3.3.: Glass slide with the glued on fluid cell, that is used in nanoindentation measurements in PBS. The glue is a medical grade two component silicone rubber. The slide depicted on the image is unrelated to the present study.

The incubation period for both, the glycation as well as the control group was 4 hours at  $34^{\circ}\text{C}$  in a temperature-controlled incubation chamber. The incubation temperature of  $34^{\circ}\text{C}$  was chosen to be well below typical mouse body temperature of  $38^{\circ}\text{C}$  and above infra-red measured tail skin surface temperature  $32^{\circ}\text{C}$  [72] as an estimate for typical physiological tail tendon temperature. This incubation temperature also might circumvent denaturation issues, that were shown to appear in collagen type I at body temperature (Leikina 2002 [73]).

The solution used for the glycated group consisted of 5mM/L EDTA (Ethylenediaminetetraacetic Acid) and 20mM/L MGO (Methylglyoxal) dissolved in 10 mM/L PBS (Phosphate Buffered Saline), while the solution for the control group was

identical but without the MGO. The pH of the MGO solution was adjusted to 7.4 at 34°C.

Finally, the second KPFM measurement was conducted on the third day after a 24 hour drying period in the desiccator, concluding the experiments.

Figure 3.4 illustrates the exact workflow.

### 3.1.2. AFM Force Mapping

The AFM workstation consists of a JPK Nanowizard Ultra Speed A (Bruker Corp., Billerica, MA, USA [74]) AFM mounted on a Zeiss Axiovert (Carl Zeiss AG, Oberkochen, Germany [75]) inverted microscope. For the AFM experiments a 3D-printed ring was mounted on the slides around the spot of collagen tissue, as mentioned above, which was filled with a 10 mM/L PBS solution as soon as the slide could be placed on the microscopes stage. Prior to the first measurement, the whole system was left to equilibrate for about 30 minutes; the inverted microscope illumination was kept at 2.8 V for all measurements to ensure a constant temperature in the fluid cell.

#### Cantilever and Calibration

For Force Mapping a Nano World PNP-DB cantilever (NanoWorld AG, Neuchâtel, Switzerland[76]) with a pyramid shaped tip was used. The chip features 4 cantilevers, two different ones on each side. For the experiment, the smaller, stiffer cantilever with the length, width and thickness of  $100 \times 40 \times 0.5 \mu\text{m}^3$ , nominal stiffness of  $0.48 \text{ N/m}$  and nominal resonance frequency of  $67 \text{ kHz}$  was used. The tip has a height of  $3.5 \mu\text{m}$  and a nominal tip radius of  $< 10 \text{ nm}$ .

Prior to the actual measurement on preparation day, the exact tip shape was determined by contact mode imaging the TGT-1 test grating (NT-MDT Spectrum Instruments, Zelenograd, Moscow, Russia [77]), an array of sharp, cone-shaped tips with an opening angle of  $50 \pm 10$  degrees on an Si wafer. The cantilever tip shape was then recovered from the image of a single cone tip by applying a deconvolution algorithm proposed by Keller and Franke (1993) [78] in post processing with an in-house Matlab code implemented by Andriotis et al [41].

Immediately before indentation measurements, after centring the laser on the cantilever, the cantilever stiffness was first determined in air using the Sader method as described by Sader et al. 1999 [79], given in the JPK software. As soon as the cantilever was submerged in PBS the laser had to be re-centred due to the changed refraction index.

From here on, the cantilever optical sensitivity was to be determined before mea-

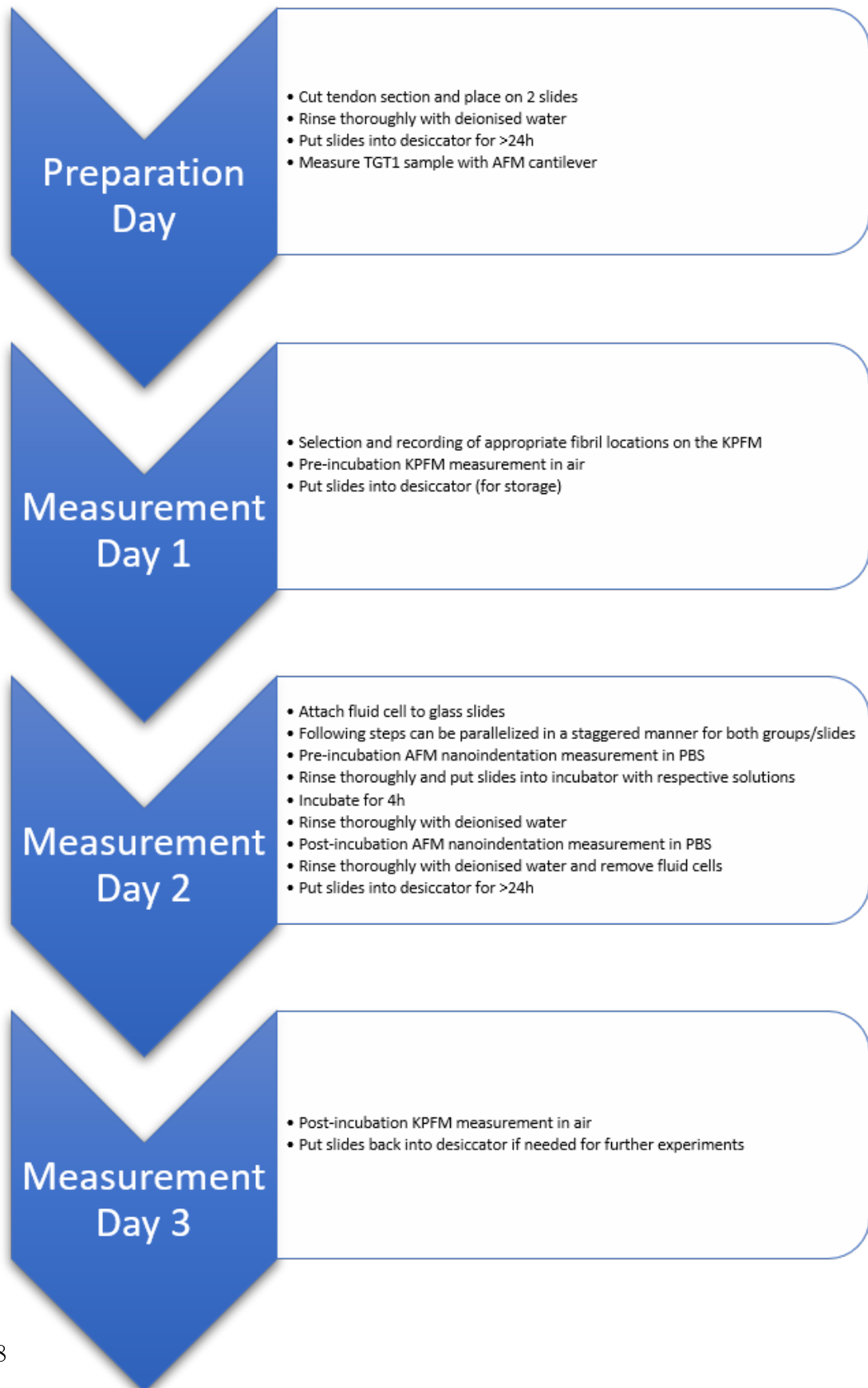


Figure 3.4.: Time layout of the whole experiment summarized in bullet points.

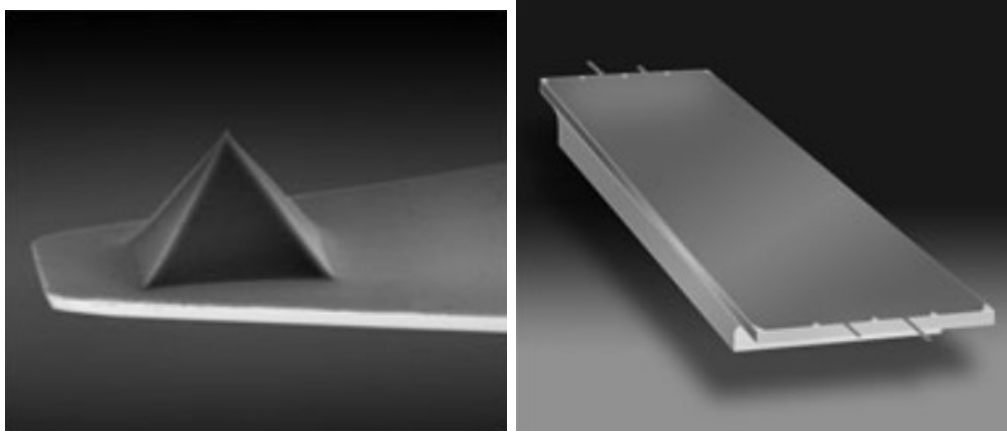


Figure 3.5.: Scanning electron image of the pyramid shaped tip (left) on a four cantilever Nano World PNP-DB chip (right).[76]

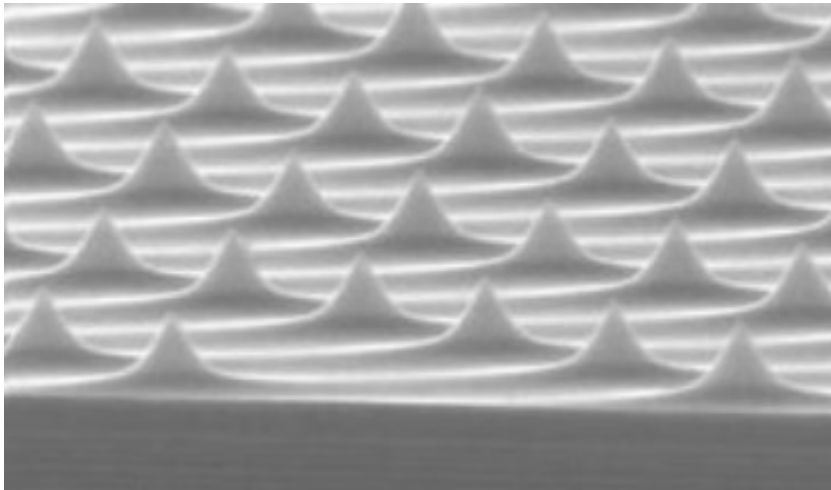


Figure 3.6.: Scanning electron image of a TGT-1 cone grating used for tip shape reconstruction.[77]

surement of every individual fibril using a contact based method [41], taking 16 deflection curves from a small area of a few  $100 \times 100 \text{ nm}^2$  of glass slide surface and then taking the slope of the HeadHeight-vs-Deflection curve as the inverse optical lever sensitivity (InvOLS). This method works on the assumption that the cantilever spring constant is orders of magnitude smaller than the contact stiffness of the glass surface, making the indentation depth negligible. The calibration force curves are to be done on the same settings as the actual fibril measurements.

## Force Maps

For fibril force mapping the fast scan direction was oriented perpendicular to the fibril direction for easier data processing. The applied indentation load was  $1 \text{ nN}$  in all experiments - chosen such that the indentation depth does not exceed 10% of the fibrils diameter [41] - and a scanning area of  $1.5 \times 1.5 \mu\text{m}^2$  with a resolution of  $64 \times 16$  pixels, 16 along the long axis of the fibrils, 64 perpendicular to it, was chosen. An exemplary map is shown in figure 3.7(B). Extension and retraction speed was set at  $2 \mu\text{m}/\text{s}$  at a sampling rate of  $2060 \text{ Hz}$  and no holding time was applied.

To ensure that the same spots could be found in all measurements, including in KPFM measurements, the  $1.5 \times 1.5 \mu\text{m}^2$  measurement windows were chosen at a fixed distance, between  $1 - 3 \mu\text{m}$ , to fibril crossings that could themselves be easily found on microscope images.

## Data Processing

While calibration during the measurements was done in the data processing software provided by JPK all the post-processing was performed using custom in-house Matlab R2020a code, written specifically for this work, mostly adapting methods from earlier in-house code provided by Orestis Andriotis [41].

The `-jpk-force-map` files recorded by the software accompanying the AFM have data channels from several sensors available: for the present work, the `'capacitiveSensorHeight'`-channel was used for the cantilever head height and the `'vDeflection'`-channel for the cantilever deflection.

First, the height profile of the force map was recreated using the lowest value of the `'capacitiveSensorHeight'`-channel on every approach force curve and then leveled using a plane fit of all data points from the glass slide surface. Which points belong to the glass slide was determined using a custom fibril masking algorithm. The software then includes a masking step for manual exclusion of regions that are deemed to be debris on the fibril that should not be analysed. It is the only step during analysis that relies on the operators judgement, trying to keep operators bias to a minimum.

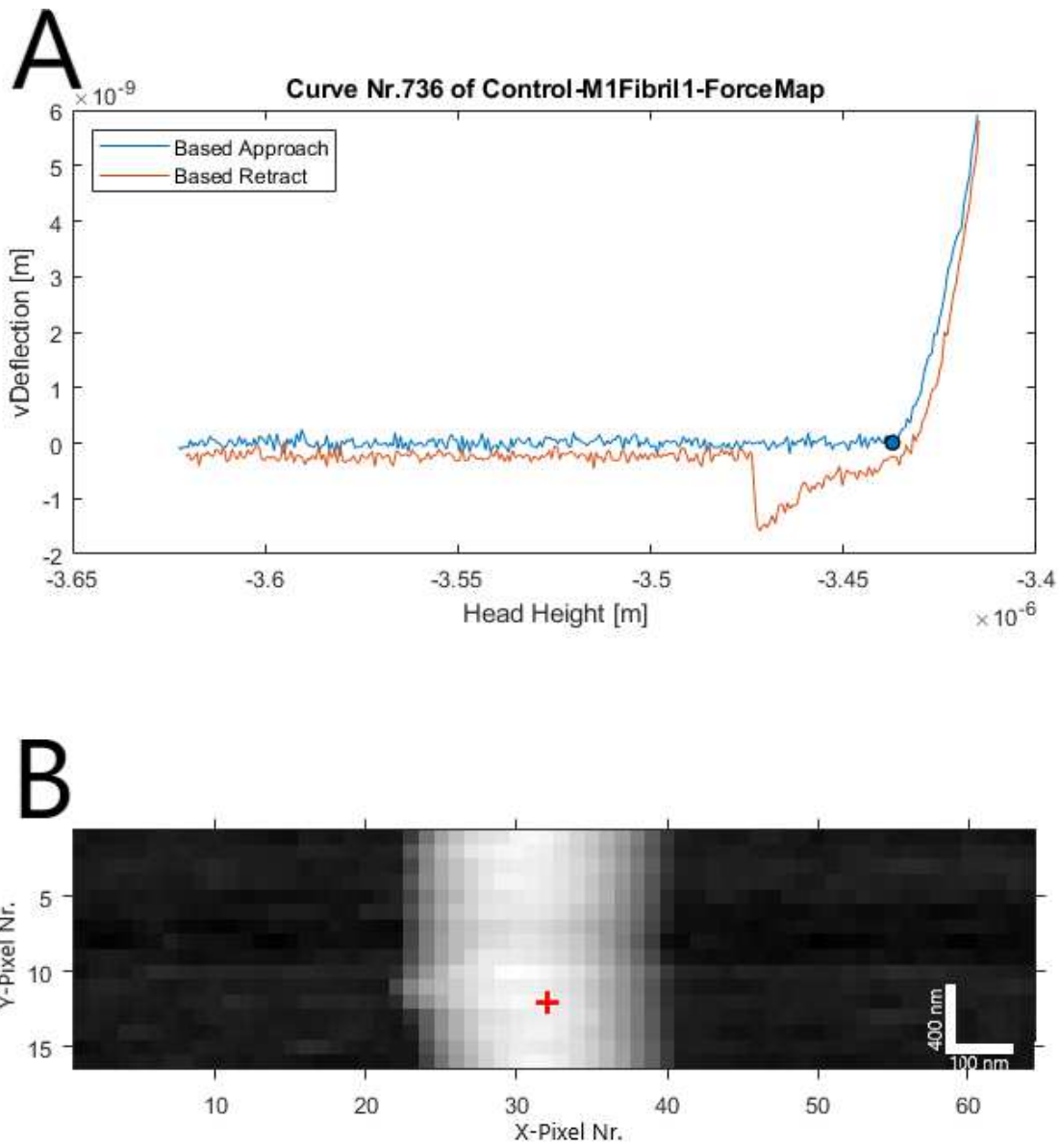


Figure 3.7.: Force Map showing the chosen resolution and fibril orientation of a random control group fibril before treatment (B) with the force curve of a randomly chosen pixel from the fibril apex (A). The blue dot in (A) represents the contact point.

The force curves then undergo a base line and tilt correction, subtracting a linear fit line done on the no-contact domain of the approach curve. Subsequently, the contact point is determined and subtracted from the force curves using the machine learning algorithm, also developed in the course of present work and described below in section 4.3.

For the calculation of the indentation modulus a method based on the work of Andriotis et al. (2014)[41] was used: The Method is based on the mechanical model for indentation experiments described by Oliver and Pharr (1992, 2004)[80][81] that assumes a purely elastic initial unloading curve with constant contact Stiffness  $S_c$ . The model then predicts a reduced indentation modulus of the contact between two spheres

$$E_r = \beta * \frac{\sqrt{\pi}}{2} \frac{S_c}{\sqrt{A_c}} \quad (3.1)$$

with projected indenter area  $A_c(h_c)$ , which can be determined from the reconstructed tip shape as a function of the effective indentation depth  $h_c$ , and correction factor  $\beta = 1.0226$  [80]. The effective contact depth accounts for a sink-in morphology [80] of the substrate and can be determined by

$$h_c = h_{max} - \epsilon \frac{P_{max}}{S_c} \quad (3.2)$$

where  $h_{max}$  is the distance between contact point and maximum Z-displacement at full load  $P_{max}$  and  $\epsilon$  a correction factor accounting for the tip shape. The indentation modulus of the fibril can then be determined via the relation of the reduced modulus to the real indentation modulus of the contacting materials

$$\frac{1}{E_r} = \frac{(1 - \nu_{Sample}^2)}{E_{Sample}} + \frac{(1 - \nu_{Indenter}^2)}{E_{Indenter}} \quad (3.3)$$

with  $\nu_{Sample}, \nu_{Indenter}$  being the materials Poisson ratio and  $E_{Sample}, E_{Indenter}$  their elastic moduli where the second term can be ignored given that  $E_{Indenter} \gg E_{Sample}$  [45] which leads to

$$E_{Sample} = \frac{1}{\beta} \frac{\sqrt{\pi}}{2} (1 - \nu_{Sample}^2) \frac{S_c}{\sqrt{A_c}} \quad (3.4)$$

The contact stiffness  $S_c$  cannot be taken as the actual slope of the unloading curve since the Z-displacement data does not just represent the actual tip indentation depth, but also the cantilevers deflection itself. Using the aforementioned method [41] the actual contact stiffness can be recovered from the uncorrected unloading slope by subtracting a reference slope that is determined from the force curves originating on the slides glass surface, since the tip can be assumed to only



indent it to a negligible depth making the curves slope representing solely the cantilever deflection itself. The contact stiffness is then

$$S_c = \frac{k_c}{\frac{1}{S_{uncorr}} - \frac{1}{S_{ref}}} \quad (3.5)$$

with  $k_c$  the cantilever spring constant,  $S_{ref}$  the averaged slope of all the force maps glass surface curves,  $S_{uncorr}$  the slope of the linear fit to the upper 75% of the unloading curve as seen in figure 3.8.

### 3.1.3. KPFM Surface Potential Measurement

Surface potential measurements were done on a Bruker Dimension FastScan AFM operated by a Bruker Nanoscope V Controller (Bruker Corp., Billerica, MA, USA [82][83]) in air in the KPFM mode, meaning a topography scan is performed by intermittent contact mode, followed by an interleave phase on the same line for imaging of the surface potential as described in section 2.2.2. The cantilever used was a Olympus AC-200TN-R3 (Olympus K.K., Shinjuku, Tokio, Japan [84]) with a length, width and thickness of  $200 \times 40 \times 3.5 \mu\text{m}^3$ , a nominal spring constant of  $9 \text{ N/m}$ , a nominal resonance frequency of  $150 \text{ kHz}$  and an aluminium reflex coating for an improved laser signal.

The same scanning area of  $1.5 \times 1.5 \mu\text{m}^2$  on the same spots as in the AFM measurements - as validated by measuring at the same distance to the recorded fibril crossings (see section 3.1.2), give and take a few  $10 - 100 \text{ nm}$  due to drift and operator inaccuracy - was recorded at a tip scan speed of  $0.25 \mu\text{m/s}$  with 128 lines and 512 data points per line. The relatively slow tip scan speed was crucial in order to minimize edge effects on the surface potential images. The intermittent contact mode drive frequency of  $153.54 \text{ kHz}$ , slightly below the measured resonance frequency, was chosen by the accompanying software while the the drive amplitude of  $926.8 \text{ mV}$  as well as the amplitude setpoint of  $344.7 \text{ mV}$  were adjusted manually to optimize image quality and eventually slightly readjusted at different stages of the experiment. The lift height of the interleave scan was set to  $0 \text{ nm}$ . Similar to the AFM force maps the fast scanning angle was chosen to be perpendicular to the fibril direction for the same reasons.

### Data Processing

The height and surface potential data first had to be extracted into `-.sdf` files from the KPFM's output files using the freeware image data analysis program Gwyddion [85] using the PyGwy console, a module for custom python scripting in Gwyddion. From there, all remaining data processing was done in a Matlab

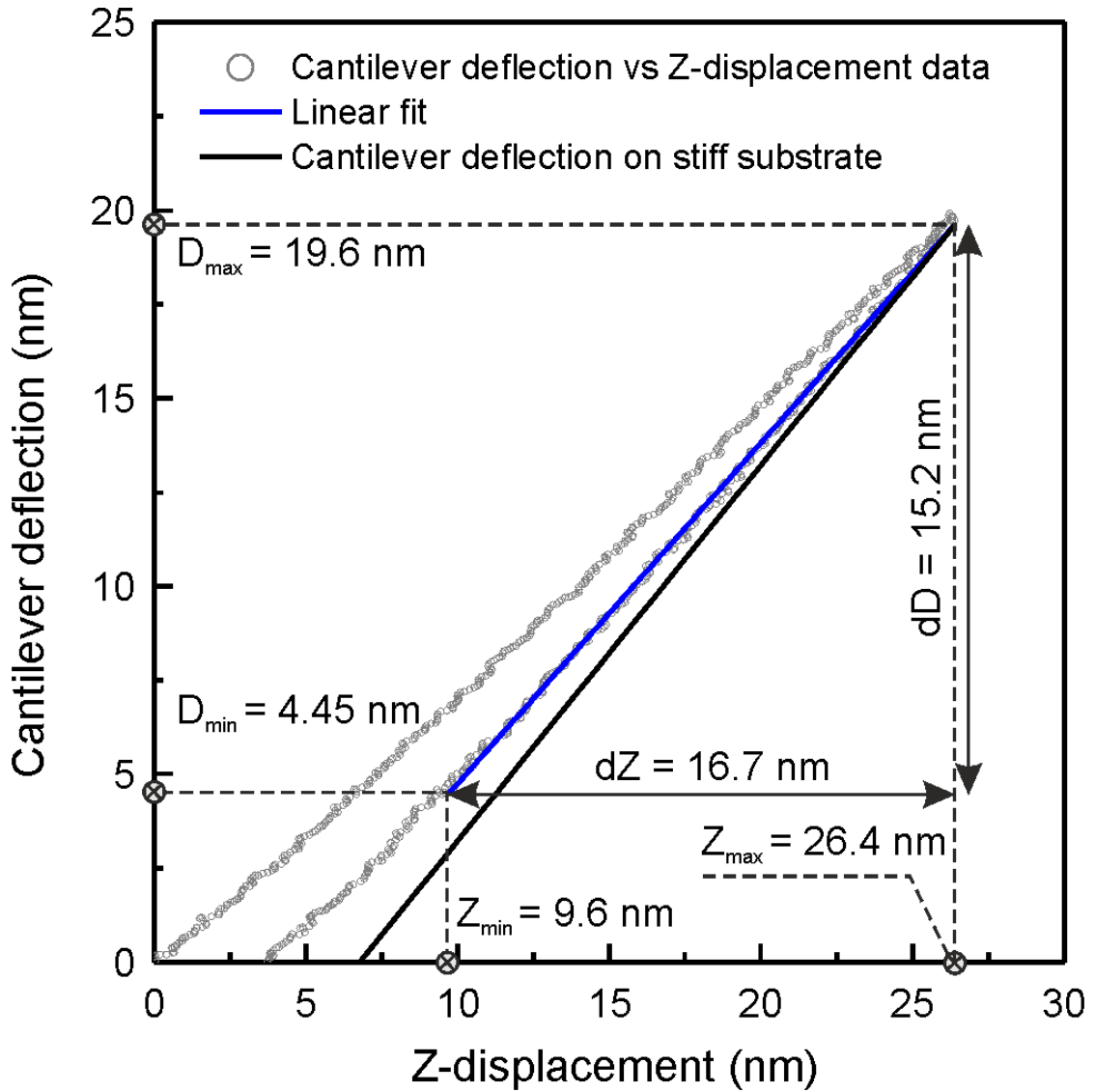


Figure 3.8.: The figure illustrates how the contact stiffness  $S_c$  can be indirectly determined from the unloading part of the displacement-deflection curve with the reference slope from a stiff substrate[41]. The linear fit is done on the upper 75% of the unloading curve.

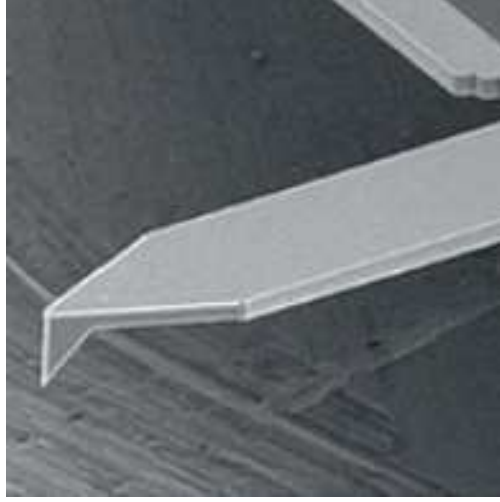


Figure 3.9.: Scanning electron image of the Olympus AC-200TN-R3 cantilever [84]

R2020a script, developed for this work.

Similar to the processing of the AFM force maps, after an initial manual exclusion step of areas suspect of being debris, the fibril was first masked with a custom algorithm to then use just the data points from the glass surface for plane fitting and levelling the height map.

The apex points of the fibril could then be determined by choosing the highest point on every line profile and by averaging over their height, the fibril diameter could be determined.

Following the Nyquist criterion for the sampling of spacial frequencies, the images' line resolution of  $\frac{1.5 \mu m}{128} = 11.71 \text{ nm}$  allow for a spacial sampling frequency  $\lambda_{sampling} = \frac{1}{11.71} \frac{1}{nm}$  well below twice the typical D-banding period of  $\lambda_{D-band} \approx \frac{1}{67} \frac{1}{nm}$ , which means that D-Banding could be examined by Fourier analysis of the apex line using the Fast Fourier Transform algorithm (FFT).

For the study of the surface potential only a relative approach could be taken by assuming unchanging surface potential of the glass surface between measurements and then subtracting the mean glass surface potential from the mean fibril surface potential:

$$\bar{\Phi}_{RelFibPot} = \bar{\Phi}_{Fib} - \bar{\Phi}_{Glass} \quad (3.6)$$

To not include edge effects in the calculations but also in order to avoid operator bias, the masks for the glass potential were automatically chosen to be all glass area at least 3 fibril diameters away from the fibril masks edge and the fibril potential mask was a stripe of one fibril diameter centred around the apex line, with the

diameter being derived from the average apex fibril height relative to the plane fitted glass slide area. Note that due to scanning tip envelope effects the apparent diameter of the fibril on the image is far wider than the actual calculated fibril diameter, leaving a thin stripe relatively safe from edge effects as seen in figure 3.10 (bottom right).

### 3.1.4. Statistical Analysis

Regarding AFM nanoindentations, for the statistical analysis of the calculated indentation moduli only force curves from the very apex of the fibril were considered. The apex points were determined by choosing the highest point of the height profile of the fast scanning axis, which in this case amounted to a maximum of 16 analysed force curves, given that none were excluded for coming from random debris in the selection step earlier. The indentation moduli of the apex points were then tested for outliers, excluding all values  $\pm 2.5 \times IQR$  (IQR, interquartile range). Subsequently, the mean of the apex indentation moduli that passed these criteria were used as the overall fibril modulus, which was then used in the main statistical analysis.

For the KPFM experiments the mean relative fibril potential  $\bar{\Phi}_{RelFibPot}$  was determined as described above and subsequently used in the main statistical analysis. Fibril diameters were calculated from the mean of the apex points height, taken from the KPFM experiments for the dry diameters and from the AFM force maps for the hydrated diameters.

D-banding values were obtained from the apex profile of the KPFM height maps using FFT.

The sets of fibril properties, determined as described above, for each of the four groups (Control Before, Control After, MGO Before, MGO After -  $N = 10$  in each) were probed for normality in a Kolmogorov-Smirnov test. The before-after-glycation-difference of the properties in the control as well as in the glycation group could then be assessed in a paired, right-tailed T-test.

The relevant metric to be explored however, was the difference of differences between glycation and control group and could be obtained in a two-sample T-test comparing the set of before-after-glycation-differences between the two groups.

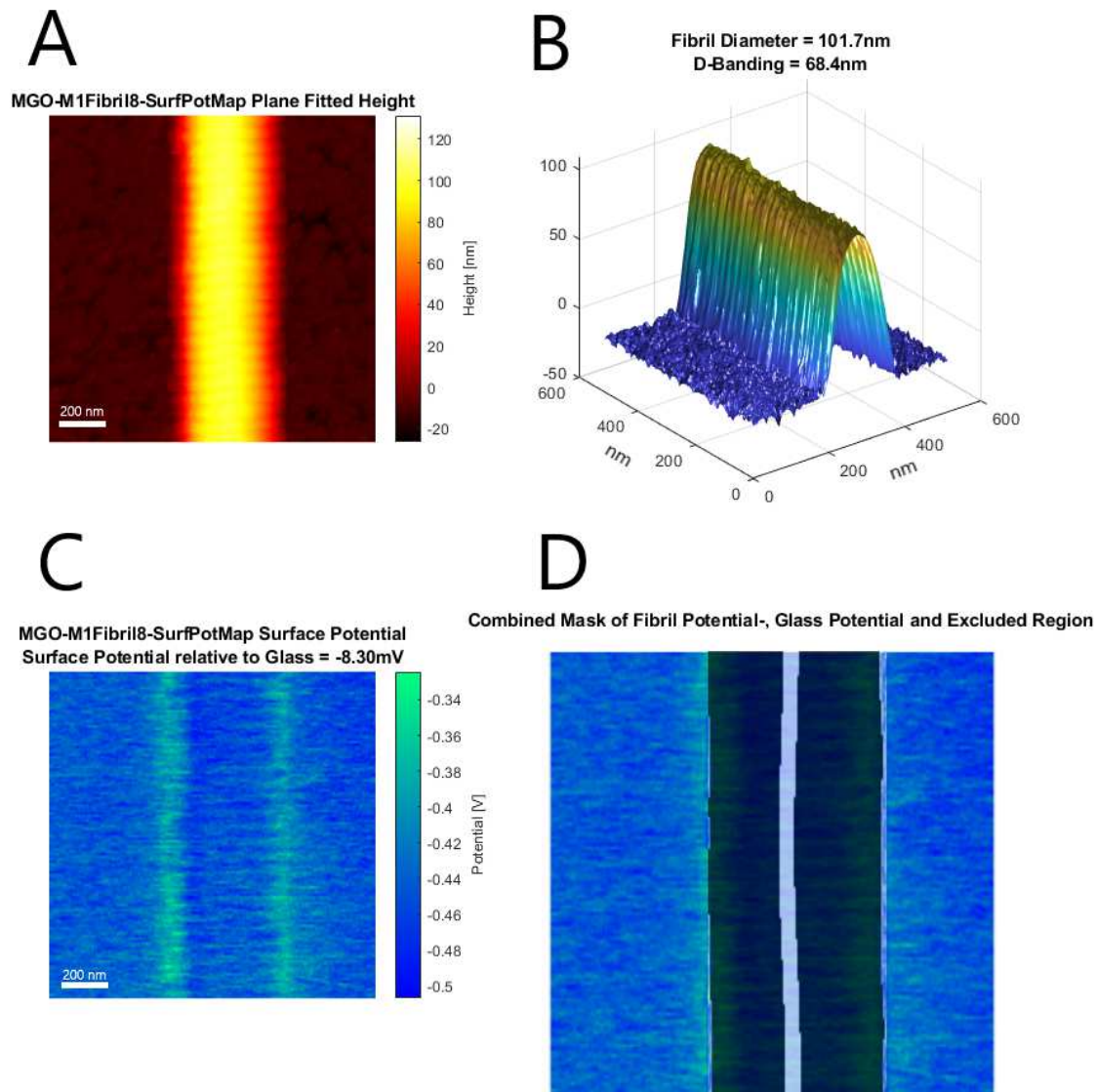


Figure 3.10.: Summary of the analysis done on one of the KPFM measurements. (A) is the height map and (B) a 3D surface plot of the KPFM height profile scan. (C) is the KPFM surface potential.(D) shows the masks that were used for the calculation of the potential difference overlaid onto (C). To avoid edge effects the fibril area was restricted to a thin area around the apex of the fibril.



Die approbierte gedruckte Originalversion dieser Diplomarbeit ist an der TU Wien Bibliothek verfügbar.  
The approved original version of this thesis is available in print at TU Wien Bibliothek.

## 4. Contact Point Determination via Convolutional Neural Network

Since its invention, AFM force spectroscopy has found a wide range of applications in science and industry. One variant is AFM based nanoindentation, which allows for acquisition of vast amounts of indentation data. One of the main properties that can be derived from nanoindentation data is the indentation modulus of the probed material. To do so in a robust and effective way, fully automated data processing is highly sought after.

Regardless of the mechanical model used for the determination of the indentation modulus, the distinction of the domains where the cantilever tip is in contact with the sample from the ones where it is still approaching, the dividing point being called 'contact point', is of utter importance. The position of the contact point has a non-linear relationship to the derived indentation modulus and leads to severe differences in its estimation, if misplaced.[86][87]

In this chapter I present a novel approach to the determination of the contact point, using well established deep machine learning techniques, translating the problem into an image regression task, which can be handled by convolutional neural networks with great accuracy and robustness. Additionally, the special network architecture used allows for an estimate of the networks uncertainty to be obtained, highlighting interesting cases, that could otherwise stay buried in the vast amounts of indentation data.

### 4.1. Contact Point: State of the Art

Below, four state of the art methods for contact point estimation are shortly presented. These are the methods that were considered for comparison to the newly developed one. Two of them, the goodness of fit and the combined method, were discarded during pretests for being too computationally expensive, while only showing less than mediocre results. It is important to mention that these are not the only state of the art approaches found in literature and comparisons presented here are not fully exhaustive [88][89][90][91][92].

## Ratio of Variance RoV

The ratio-of-variance method (see fig. 4.1) works by taking every point  $d_i$  of the force-distance curve,  $d_i$  being the  $i$ -th force or alternatively deflection value, and then calculating the variance of a window of  $N$  points before and after  $d_i$  and taking its ratio:

$$RoV_i = \frac{var(d_{i+1}, d_{i+2}, \dots, d_{i+N})}{var(d_{i-1}, d_{i-2}, \dots, d_{i-N})}. \quad (4.1)$$

The point with the highest RoV is then chosen as contact point as seen in figure 4.1 (B). The sliding window size  $N$  is a hyperparameter and the efficiency of the method relies on it being chosen large enough to provide stability against noise, while simultaneously not being larger than the number of data points after the actual contact point, since the RoV is only well defined for the data  $N+1$  points away from the start and end of the curve. The sliding window in this work was chosen to be  $N = 20$ .

## Derivative STD SD6

This method tries to estimate a metric for the noise of the noncontact domain of the curve and then choosing the contact point as the one, exceeding this threshold (see fig. 4.2). It takes the numerical derivative of the force curve, essentially acting as a high-pass filter, then calculates the standard deviation of the derivative values of the points in the first 50% of the curve, prior to contact between tip and sample. The threshold is then set to the standard deviation times a constant factor that is a hyperparameter of this method and conventionally chosen as 6, hence the name SD6.

## Goodness of Fit GoF

The goodness-of-fit method works by choosing an analytic formula from a mechanical model of the indentation curve and fitting said model to the data (see fig. 4.3). In this work the Hertz-Sneddon model for a parabolic cantilever tip shape [93] was used. Every single data point is then treated as a hypothetical contact point, subsequently calculating a set of fits for each one. The R-squared value of the fits is then taken as a metric to decide, which contact point produces the best fit (fig. 4.3 (B)).

The method is computationally very expensive and was left out of consideration for present work. Pretests also showed that for this method to work accurately a more accurate mechanical model is needed, since at the scale of the indentations in this work non-contact forces become very dominant near the actual contact point neighbourhood.



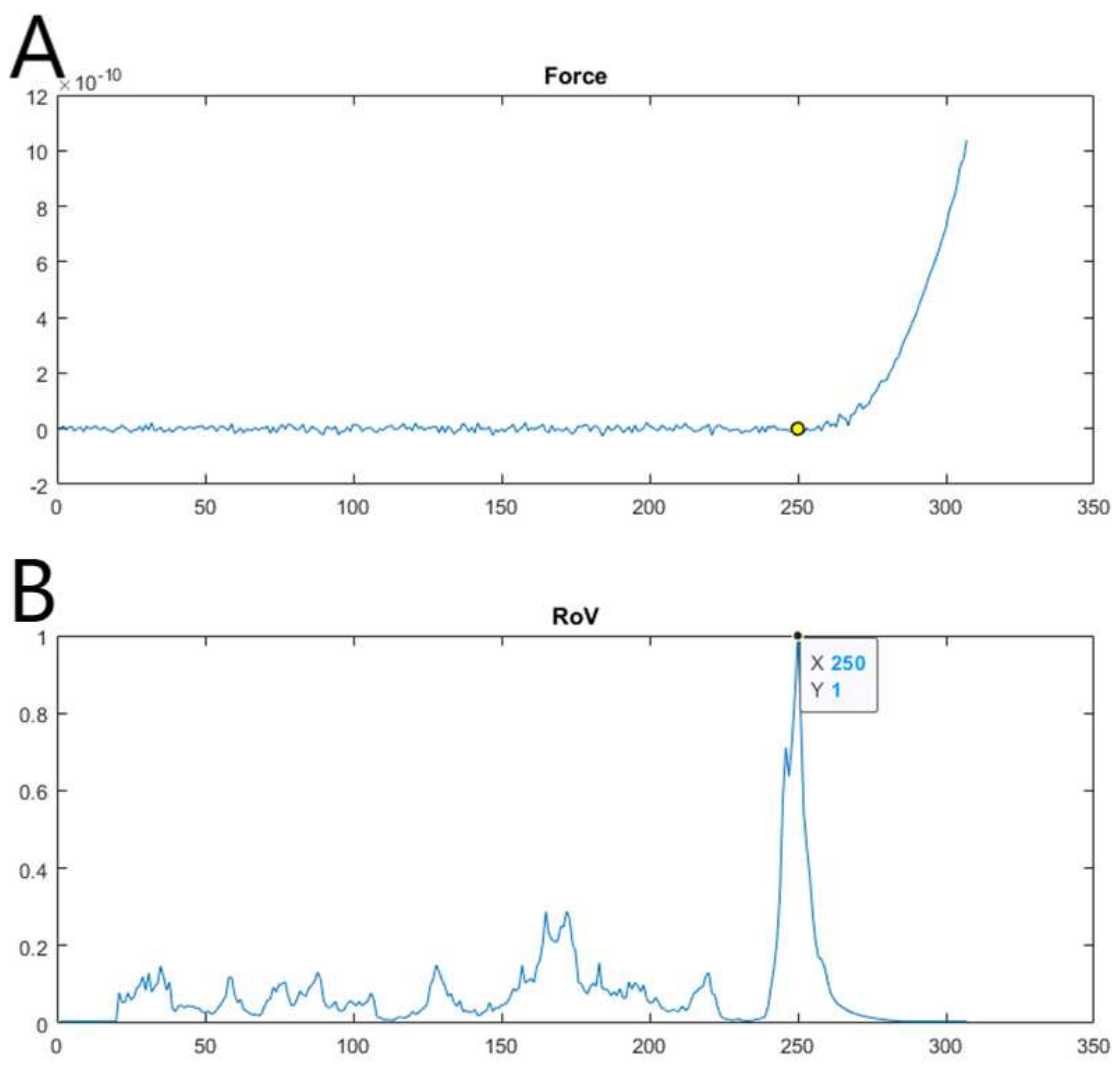


Figure 4.1.: Graph (A) shows the approach part of the force curve with the contact point determined by the RoV-method, while (B) is the normalized RoV graph.

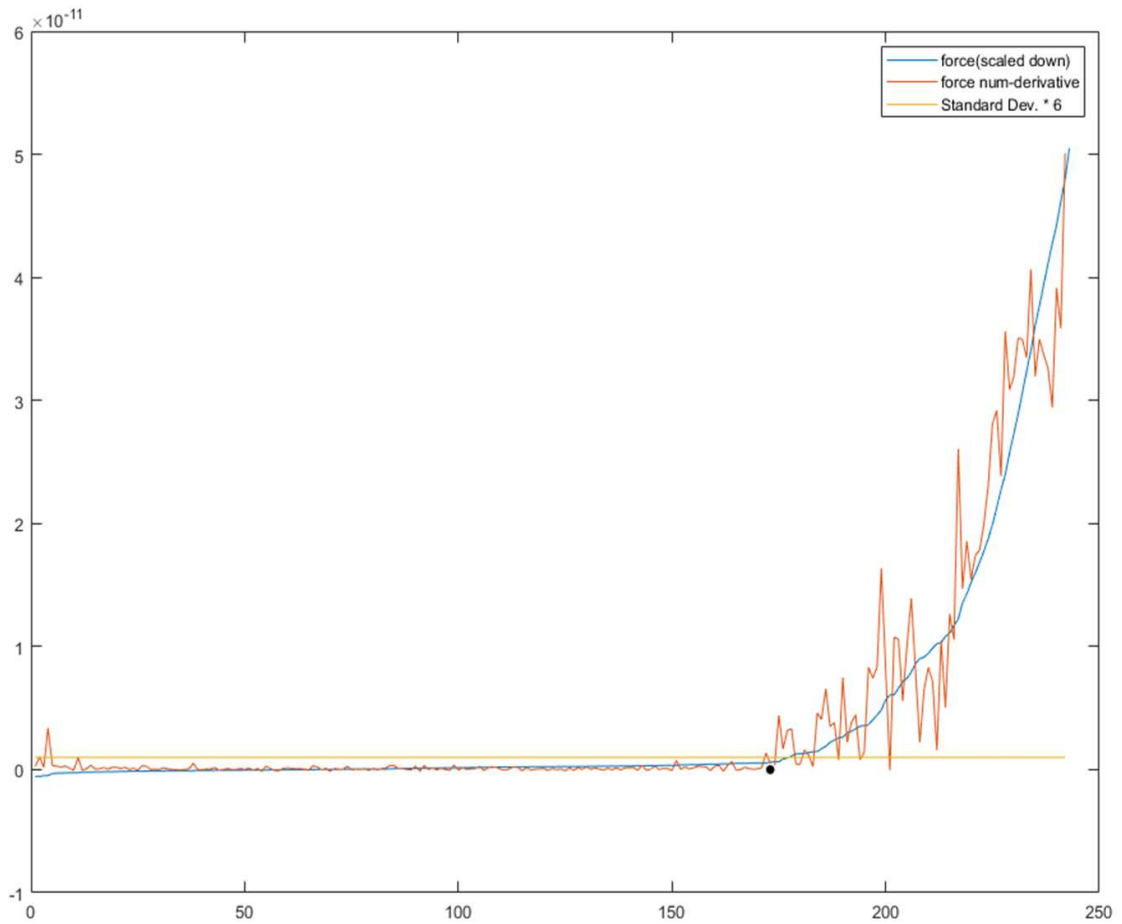


Figure 4.2.: The orange curve is the numerical derivative of the force curve while the yellow line shows the threshold determined by the method. The blue curve shows the scaled down and smoothed force curve for reference together with the resulting estimate for the contact point.

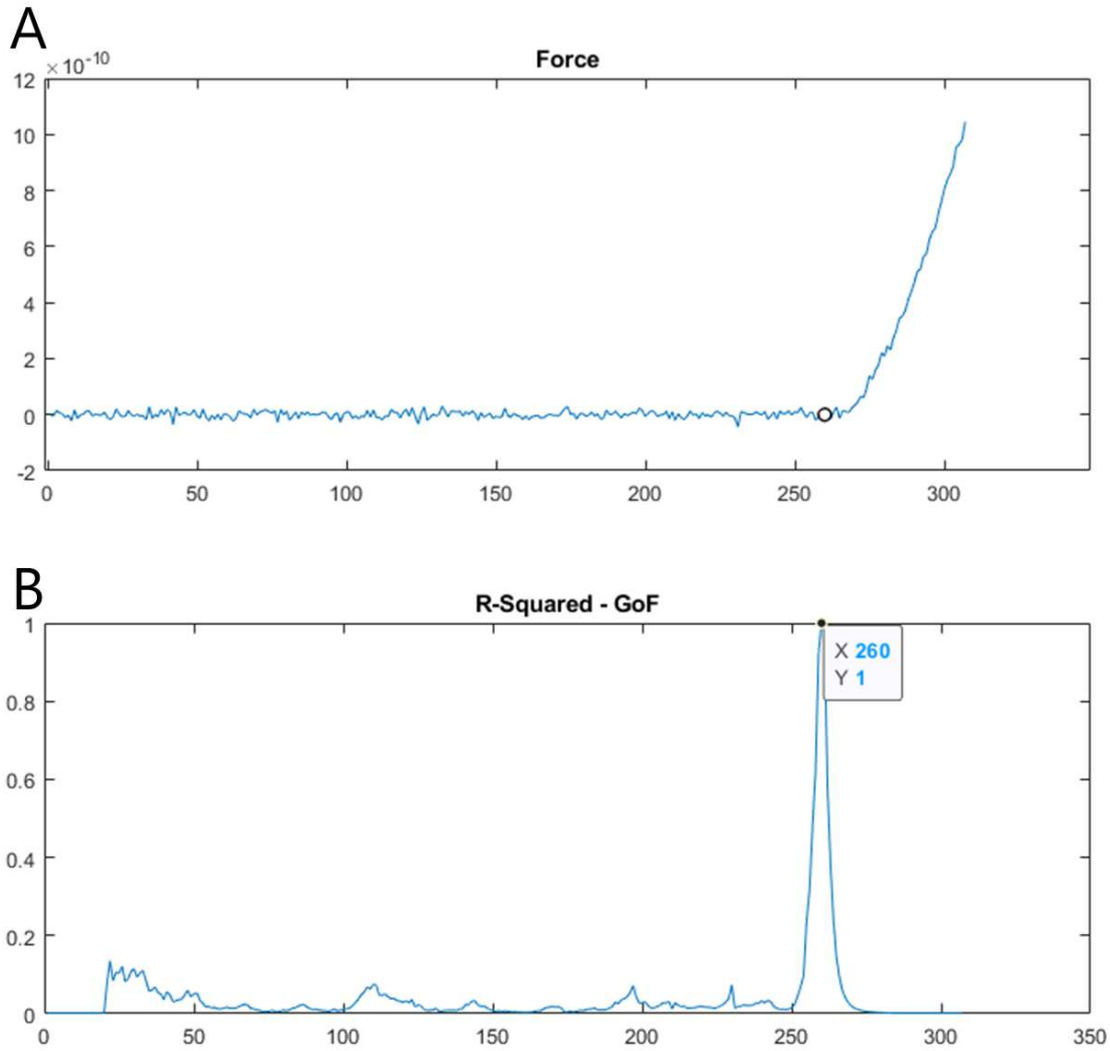


Figure 4.3.: Graph (A) shows the approach part of the force curve with the contact point determined by the GoF-method, while (B) is the normalized GoF graph.

## Combined RoV and GoF

Several variants of combined methods have been tested by Gavara et al.(2016)[87] for indentation experiments on biological cells. This variant works by just multiplying the GoF curve with the RoV curve and then taking the highest resulting value. Since GoF has been deemed infeasible and underperforming for this work, the combined method was also not tested.

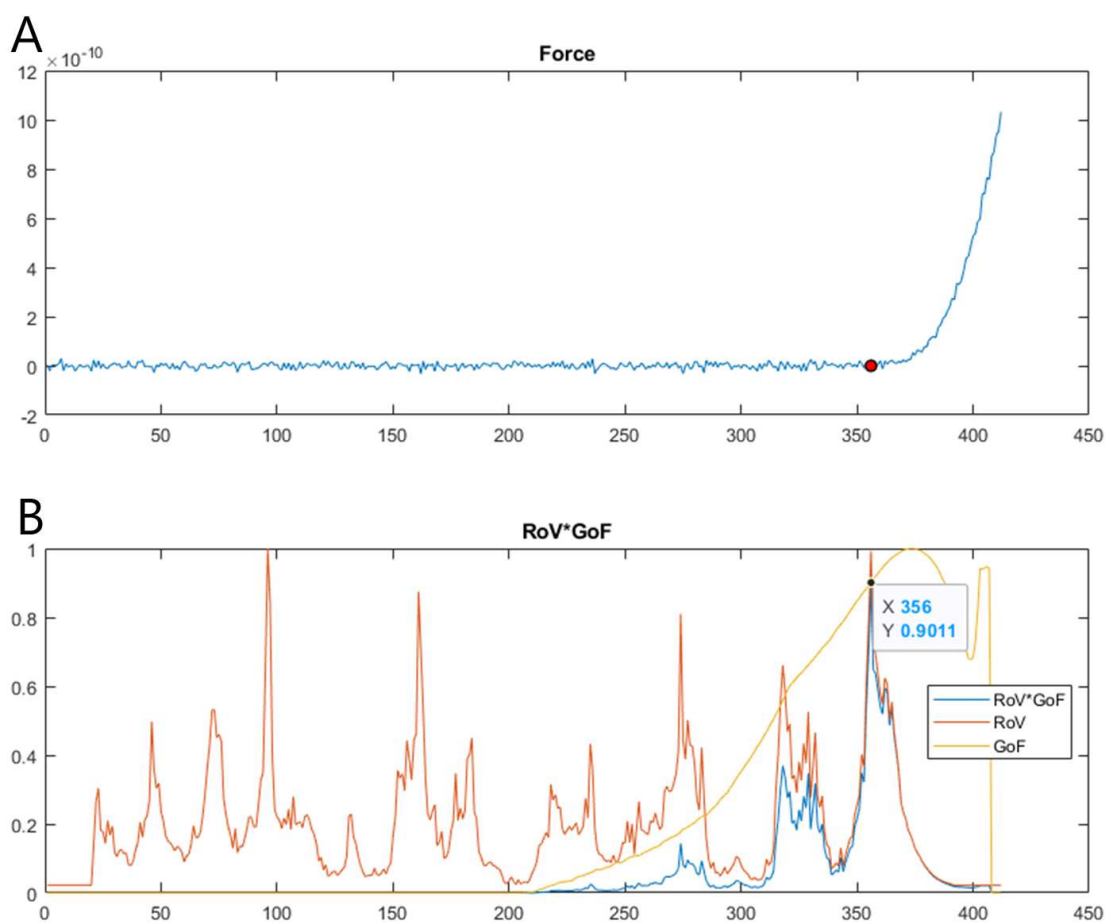


Figure 4.4.: Graph (A) shows the approach part of the force curve with the contact point determined by the combined method, while (B) is the GoF (yellow) and RoV (Orange) graph as well as their product (blue).

## 4.2. Deep Convolutional Neural Networks

Deep learning is a machine learning technique that uses artificial neural networks (ANNs) with many hidden layers and millions to billions of connections for difficult data and image processing tasks. Especially deep convolutional learning has seen great success, since the historic AlexNet paper (Krizhevsky 2012 [94]) has been released with, at the time overwhelming, benchmarks in the ImageNet competition. The basic working principle of the prediction process in an ANN is a set of neurons with weighted connections, as seen depicted in figure 4.5, that sum up the weighted value of all their input neurons and pass the resulting value to the next layer of neurons after first going through a non-linear function, like the currently popular ReLu function  $f(x) = \max(0, x)$ . To train such a network under the supervised learning paradigm, one needs to define a loss- or cost-function, that evaluates the ANNs predictions by assigning a loss value to the output, that then in turn determines how the weights and biases need to be updated. This process of repeated predicting, evaluating and weight updating is subsumed under the term backpropagation.

Since fully connected layers, where every neuron maps to every neuron in the adjacent layers, lose every sense of spatial correlation in data inputs like images, thereby becoming very inefficient and slow during training, the use of so called convolutional layers has become very popular. In a convolutional layer the neurons only connect to a window of selected pixel size, therefore becoming restricted to small spatial feature recognition. In this way, a deep convolutional network is naturally restricted to highlight local, low level features of the input in the early layers, while learning high level features in the deeper layers. The idea is then to make deeper and deeper networks to deal with tasks that require high abstraction. Figure 4.6 depicts a simple, shallow architecture illustrating the basic principle of convolutional networks.

When making ANNs very deep, one faces the problem of vanishing gradients, meaning the weight updates made during backpropagation merely affect the deepest layers (closest to the output), while the upper layers don't learn anything new. To avoid this problem (He et al. 2015)[97] proposed so called residual blocks (see fig. 4.7). The blocks have a forking structure that pass the input through one channel into one or more layers with learnable parameters, while additionally going through the other channel, which is a so called skip connection. Skip connections transport the output from previous layers directly to the next one, bypassing the residual blocks learnable layers. Before getting passed on to the next residual block, the outputs of both channels get added together. This way, the weight updates of the backpropagation algorithm have a direct connection to the upper layers.

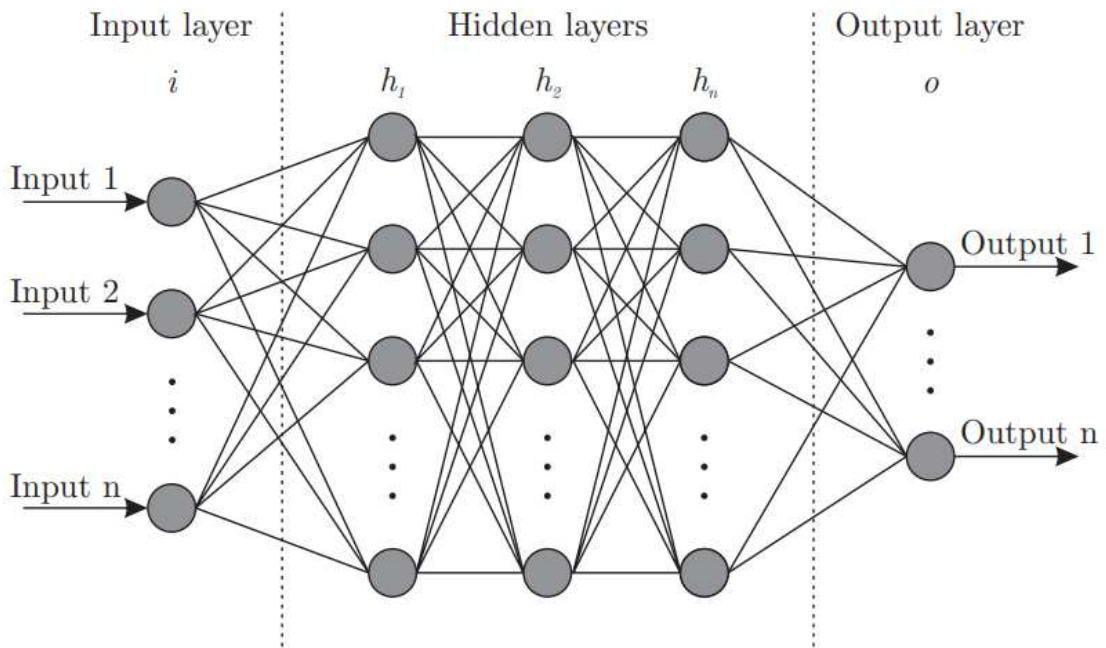


Figure 4.5.: Basic structure of a fully connected neural network with three hidden layers. The numbered inputs could represent anything from pixel values in image recognition tasks to a set of variables in, for example, weather modelling (eg. pressure, temperature, humidity). [95]

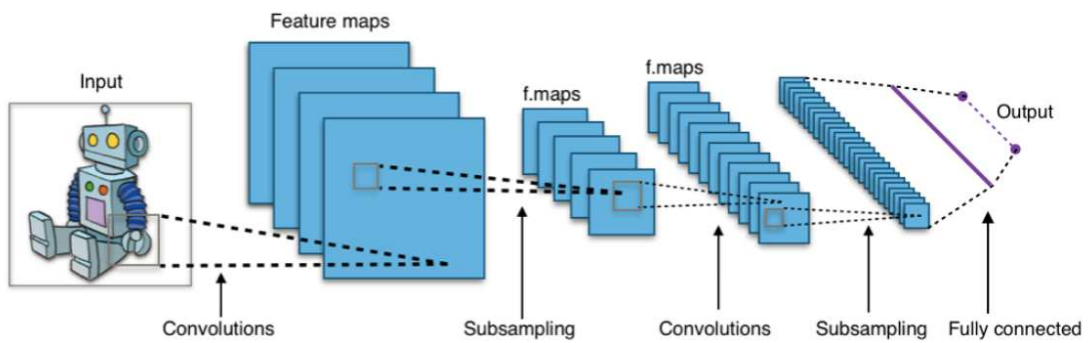


Figure 4.6.: Convolutional layers scan a sliding window over previous layers to preserve spatial features in the input image. The deeper the network is layered, the more high level features can be extracted. [96]

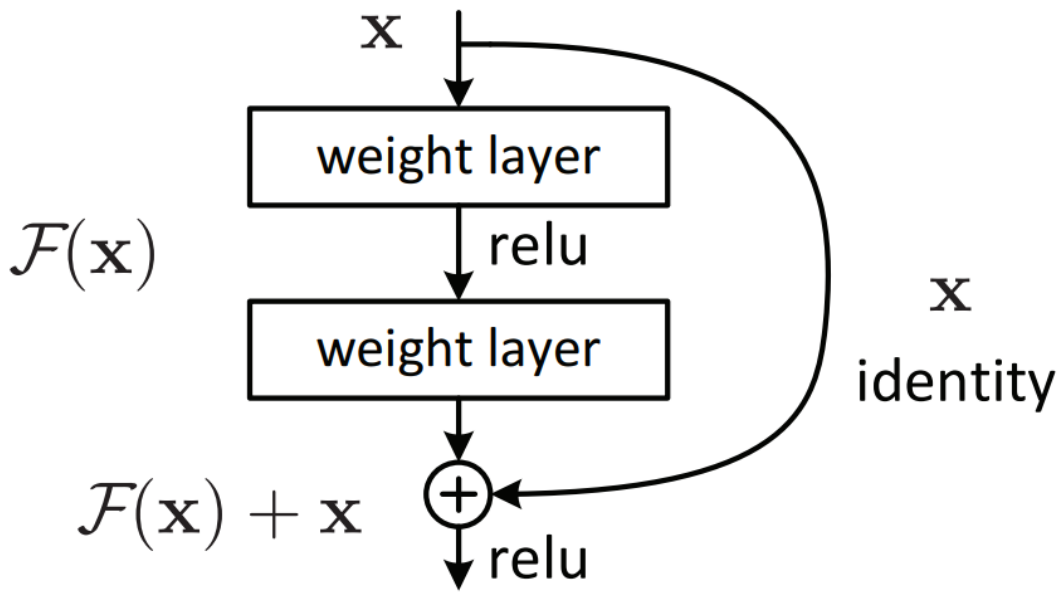


Figure 4.7.: Skip connections transport the output from previous layers directly to the next one, bypassing the residual blocks learnable layers.[97]

### 4.3. Contact Point Estimation via Convolutional Neural Network

For the estimation of the contact point, the exact point in a Z-displacement-vs-force curve when the AFM cantilever tip comes into contact with the specimens surface, a novel approach to the state of the art was sought since accurate contact point determination has been shown to be very important for accurate analysis [86]. Deep Convolutional Neural Networks (CNNs) represent a potent tool for image classification [94] and, in this case, regression tasks, and were developed and deployed in present work.

The CNN was developed, trained under the supervised learning paradigm and tested using the Matlab R2020a Deep Learning Toolbox [98], a mid to high level API for deep learning tasks.

The contact point estimation and indentation moduli derived with the new method were then compared to the ones calculated from the in-house standard method and another state of the art method, the ratio-of-variance method (RoV) [87].

### 4.3.1. Architecture

For the network, several different architectures were explored and tested: Along with several CNN designs also a LSTM (Long Short-Term Memory) architecture using the force curve data points as sequential input. The design that prevailed in the end was a deep residual network [97] with 6 residual blocks and a monte carlo style dropout [99] architecture.

In order to input the force curves to the CNN as images the data sequence of 2-tuples of 'capacitiveSensorHeight' and 'vDeflection' had to first be converted into a downsampled grayscale force curve image with a custom algorithm. The result is a  $128 \times 128$  pixel image downsampled via bilinear interpolation as seen in figure 4.8.

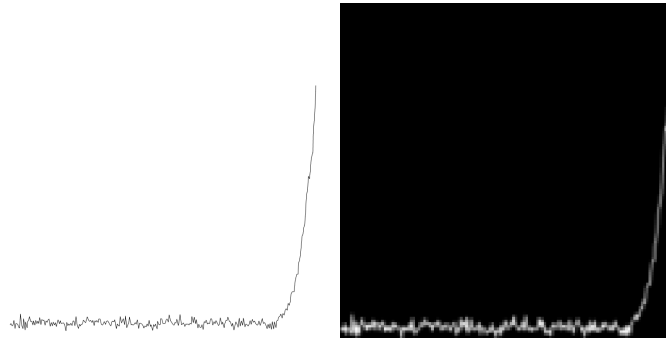


Figure 4.8.: Example of a typical force curve (left) converted into the required  $128 \times 128$  grayscale input image format(right).

The network architecture as visualized in figure 4.9 follows a ResNet-like design, meaning that most of the layers with learnable parameters are embedded in so called residual blocks, that incorporate skip connections, that pass the original input of the block on to the next one unafflicted. This has been shown to massively facilitate and improve the training process by dealing with a lot of the problems associated with 'vanishing gradients'[97].

On top of this base structure, the network was also designed to be operated in a monte carlo style fashion [99], meaning that every single layer with learnable parameters is preceded by a so called dropout layer, that gives every single connection within a given layer a 20% chance of being set to 0 during a forward pass. While dropout layers usually only take the function of a regularizer during training and are switched off when deployed, they remain active in the monte carlo method leading to a probabilistic output of the network during inference. This fact can then be used to generate a distribution of possible outputs with an aver-



age and standard deviation that can be interpreted as the networks contact point estimation together with a measure of its uncertainty respectively.

### 4.3.2. Data Set and Training

The data set used for training consisted of 4110 hand labelled force curves, with 512 originating from indentation experiments done on tick cement (related research by Suppan, Nürnberger et al.[100]) in air and the rest from PBS indentation experiments on collagen fibrils during development of the experiment protocol for present work.

For the training of the network the whole data set was randomly divided into  $\frac{3}{4}$  training set and  $\frac{1}{4}$  validation set. The network was trained using the 'ADAM' optimizer algorithm [101] with a mini batch size of 100, reshuffling batches after every epoch and an initial learning rate of 0.002 with a learn rate drop factor of 0.5 after every 100 steps. There was no cut-off validation error set to define when to halt the training process. The training was done over several hours over night and halted, as soon as there was no significant improvement to be seen for several epochs.

## 4.4. Results and Comparison

In figure 4.10 one can see typical activation patterns of the convolutional neural network (CNN) in some randomly sampled channels of the second convolution layer of the second residual block (see figure 4.9) using the Matlab R2020a 'activations'-function from the Deep Learning Toolkit [98].

Interestingly, some layers don't seem to respond to the input at all, while the ones that do respond, highlight either the curve itself or seem to highlight some sort of curve envelope. Some channels seemingly doing nothing, however, does not translate to them being useless, as they could activate on other types of inputs or correspond to dealing with special cases.

In deeper layers, such as the second convolution layer of the last (deepest) residual blocks as seen in figure 4.11, the image is already compressed down into  $8 \times 8$  pixels but 256 channels broad and the activations seem to mainly activate on the bottom right area, showing convergence to the contact point

To see if the Monte-Carlo-Dropout method for inference of the CNN successfully correlates 'problematic' curves with a high standard deviation of Dropout predictions - problematic in the sense that the curve would be deemed unreliable for E-mod calculation due to slip-off events or similar defects - curves with exception-

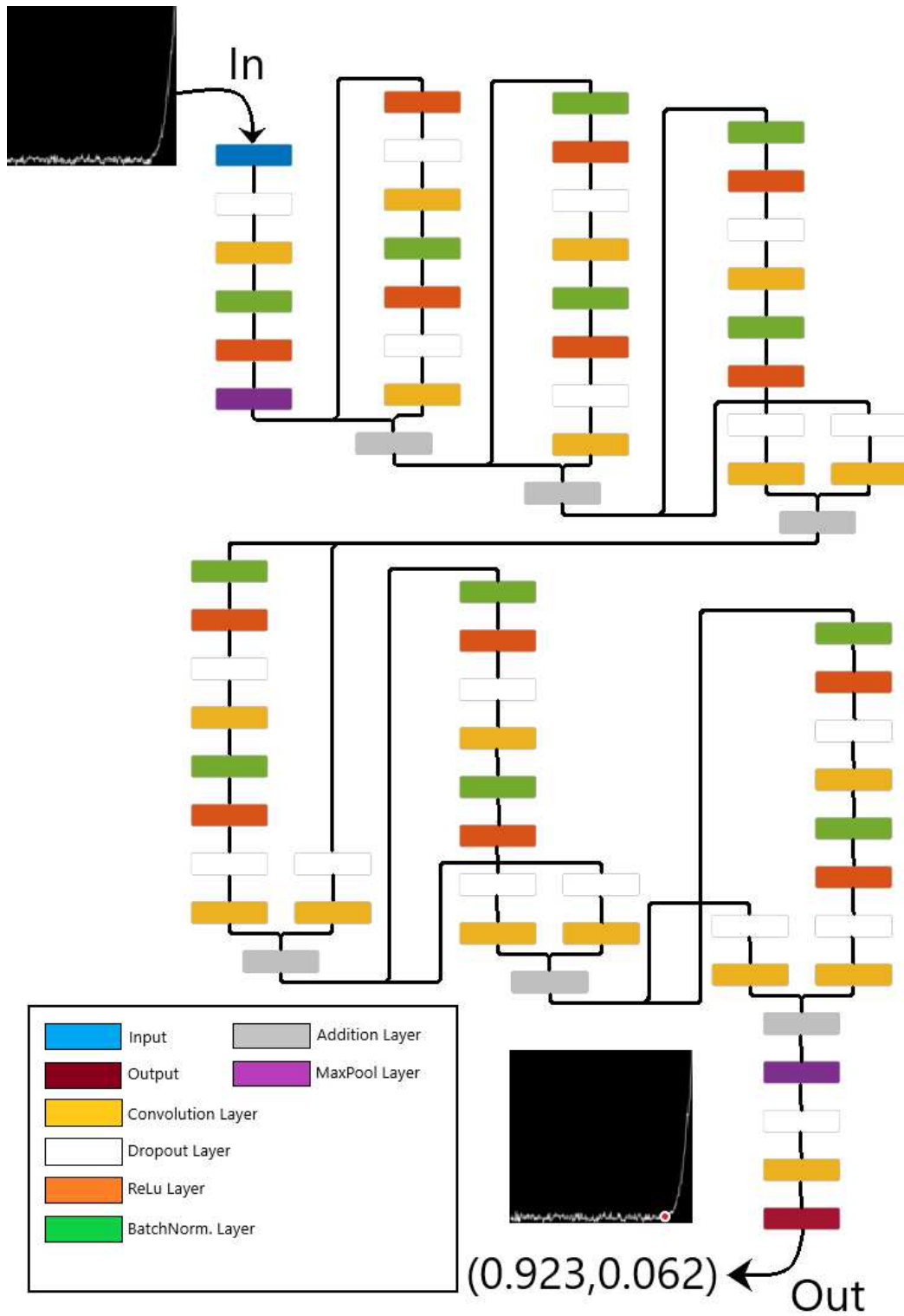


Figure 4.9.: Illustration of the ResNet-like network-architecture. After an initial downsampling process through a convolutional layer of window size  $7 \times 7$  and a stride of 2 the image goes through 6 residual blocks, with the occasional downsampling also occurring in the skip connection, then goes through a final layer of global average pooling (violet) followed by one fully connected layer (yellow) that brings the network dimension down to 2 output values, representing the horizontal and vertical position on the image. Note that for the monte carlo method to work every layer with learnable parameters needs to be preceded by a dropout layer (white).

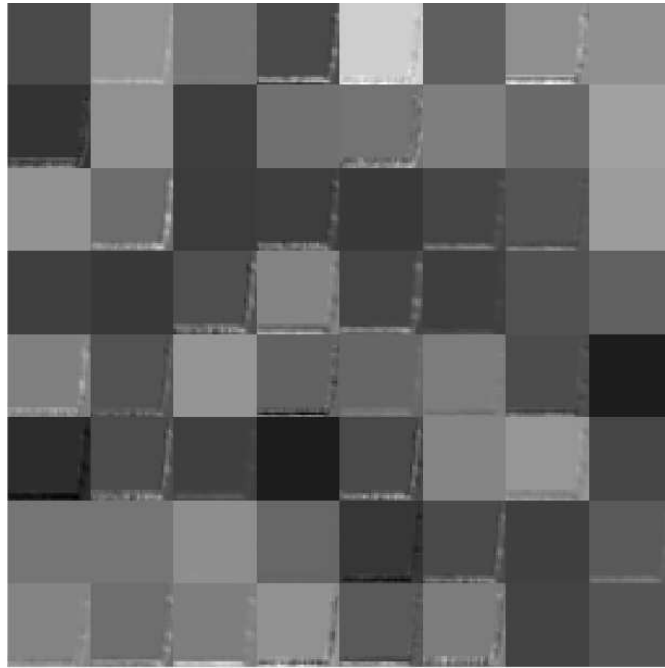


Figure 4.10.: Activations of the second convolution layer in the second residual block of the CNN (without Dropout) showing the networks response to a randomly picked force curve.

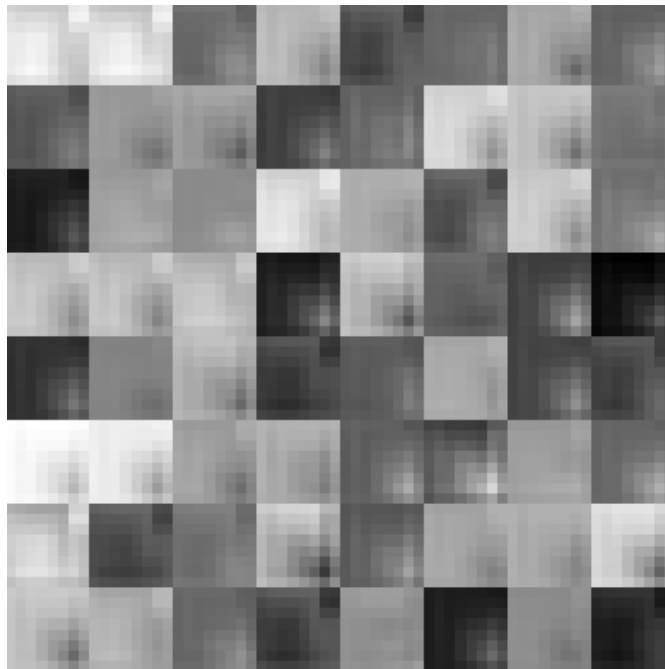


Figure 4.11.: Activations of the second convolution layer in the last residual block of the CNN (without Dropout) showing the networks response to a randomly picked force curve.

ally high as well as ones with very low uncertainty and some in between would be looked at in attempt to find patterns in the networks uncertainty predictions. Uncertainty mean over all 40960 force curves of the experiment was  $(3.31 \pm 0.3) \text{ nm}$ . Exemplary curves for the found patterns can be seen in figure 4.12:

(A,B) Curves that are generally well behaved and come from the soft fibril surface, resulting in greater indentation depths, tend to have a very low uncertainty. (C,D) Uncertainty on problematic curves depends greatly on where in the curve the irregularity occurs: if it happens higher up in the curve and the area around the contact point is normal, the system still outputs very certain predictions, while if there are slip-off events or similar disturbances in the lower parts around the contact point, standard deviation of dropout predictions tends to get large. Note that even though uncertainty in the curve (C) is high, the mean estimate still somewhat manages to ignore the slip-off event allowing for a sensible E-mod calculation. The opposite is true for curve (D), since true indentation depth is probably vastly different. (E,F) Interestingly, the CNN has great uncertainty in curves, that derive from the glass surface and generally curves that have a big slope right after contact.

Finally the new method was compared to two other established methods of contact point determination, the ratio-of-variance method (RoV) and the established in-house method, for the lack of a better alternative, referred to as derivative-STD method (SD6).

After an extensive investigation of the contact point estimates for a substantial part, about 25%, of 640 total fibril apex curves, an exemplary collection of typical curves showing common problems for the different methods was put together in figure 4.13. The RoV-method is generally the most error prone of the three:

In (A) it is demonstrated how the random noise in the no-contact domain can produce a false RoV maximum by having a region of high variance follow one of exceptionally low variance. (B) shows how this effect can also occur, if the onset of the contact-part happens gradually enough; an exceptional difference in variance between following noise-windows isn't even needed. Generally, the RoV method produces lower indentation modulus estimates compared to the other two methods presented here.

The SD6-method is overall very stable but prone to error from two sources: as seen in (A), a sufficiently big noise-spike in the no-contact part after the first 50% of the curve will lead to a false detection of the contact point. This effect can only cause false estimations towards lower indentation moduli. The second error source is the fairly strong dependence on the first 50% of the whole curve, where the method gets its threshold estimate from. Graph (E) shows how a large scale non-linearity in the first part of the curve leads to a substantially overestimated

## Monte Carlo Dropout Uncertainty

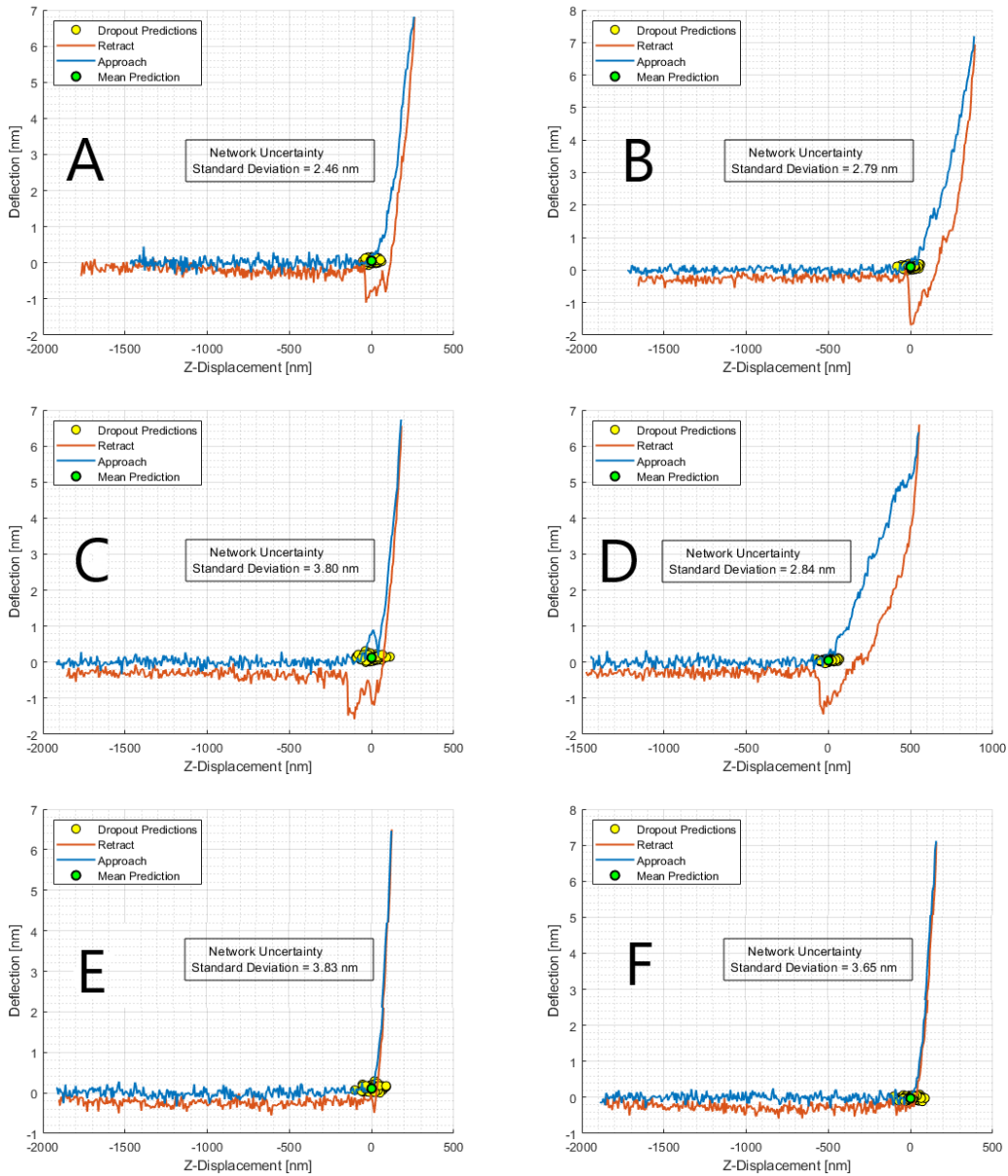


Figure 4.12.: Six exemplary force curves showing, what makes the CNNs prediction more or less certain about its prediction. For reference, overall uncertainty mean in the experiment was  $(3.31 \pm 0.3) \text{ nm}$ . (more detailed description in full text body)

CP-Est. Method Comparison for $\Delta E_{MGO} - \Delta E_{Control}$ [MPa]			
	MC Dropout CNN	Ratio of Variance	Derivative STD
$\Delta Mean$ [MPa]	0.34	0.30	0.33
$p - value$	0.0184	0.0051	0.0023
$Power \beta$	68.87%	85.4%	91.86%

Table 4.1.: Table highlighting the differences in the results of the statistical analysis on the force maps indentation moduli caused by different choice of contact point determination method.

noise threshold, leading to the contact point being set too far into the curves contact domain after the actual contact point. Contact point determination using the monte carlo dropout CNN proved to be the most robust and accurate one and no really bad example could be found during investigation. A small bias towards estimates being below the actual curve and a bit too far to the right of the actual contact point could be determined and is shown in graphs (C), (D) and to some extent (B).

One interesting case was graph (F) where the curve shows a pretty distinct slip-off event. While the RoV- and SD6-method put their estimate at the beginning of the slip-off event, the CNNs large scale awareness of the contact domain of the curve makes it nudge the estimate further to the right towards the contact point of the actual contact domain.

In appendix A.1 the statistical analysis of the indentation moduli based on the alternative methods of contact point determination are given. Surprisingly, both, the RoV-, as well as the SD6-method yield *more significant* results, also at higher power levels. The CNN method overall produces bigger absolute differences, though. Table 4.1 shows the relevant differences of the methods.

## Comparison to State of the Art Methods

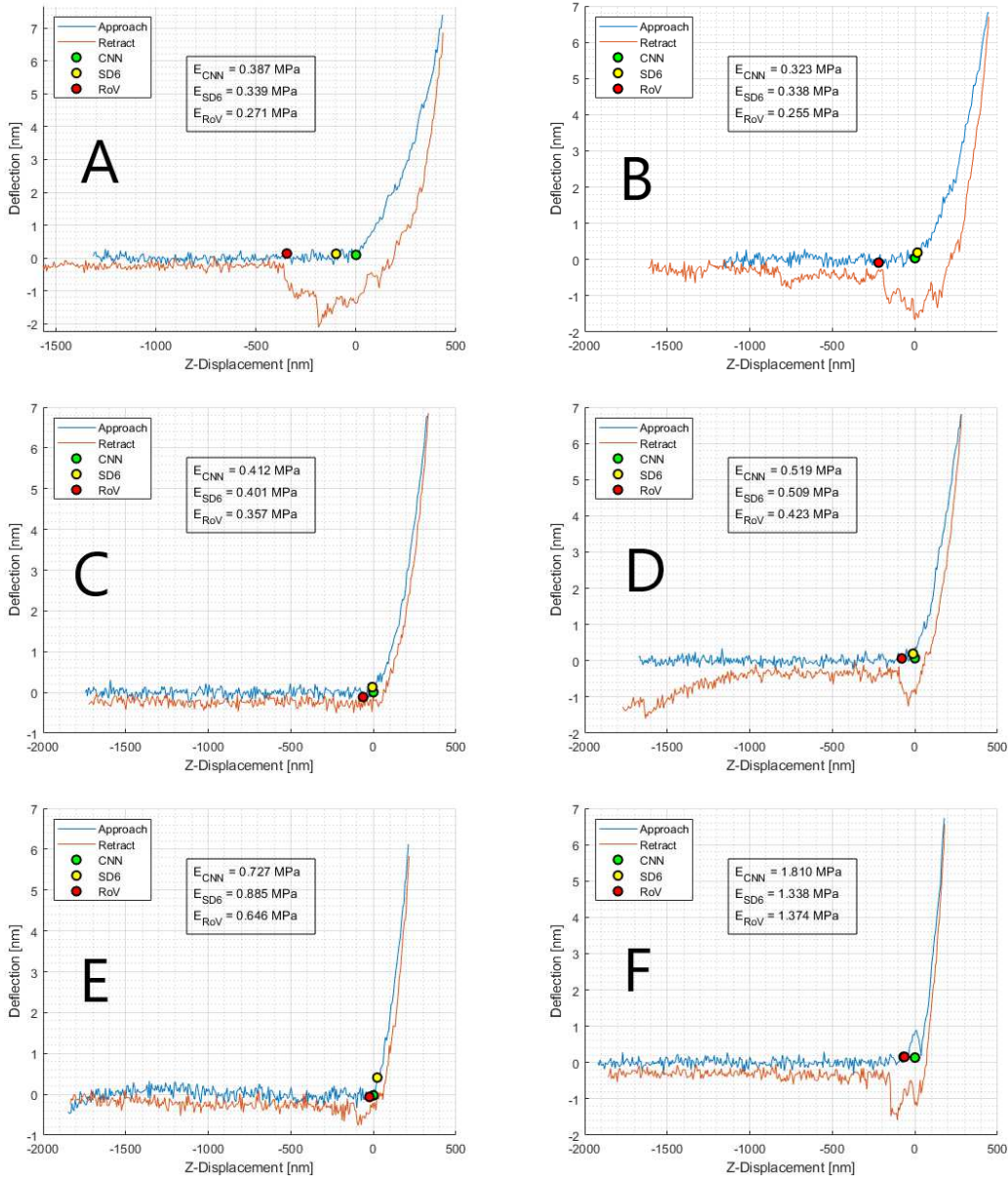


Figure 4.13.: Six exemplary force curves demonstrating the weaknesses and problems with the tested methods (more detailed description in full text body)



Die approbierte gedruckte Originalversion dieser Diplomarbeit ist an der TU Wien Bibliothek verfügbar.  
The approved original version of this thesis is available in print at TU Wien Bibliothek.



# 5. Mechanics and Surface Potential of Individual Collagen Fibrils as a Function of In Vitro Glycation

Table 5.1 shows a summary of all the metrics that were extracted from the data. Note that the experiment was designed for the exploration of changes in indentation modulus and surface potential. Other findings should be treated with caution regarding their statistical significance, as suggested by Ioannidis et al. 2005 [102].

## 5.1. Changes in Fibril Indentation Modulus through Glycation

AFM nanoindentation measurements have been done on collagen fibrils at an indentation set point force of 1  $nN$ . All tested sets passed the test for normality, while force curves with indentation modulus outside  $2.5 * IQR$  (interquartile range) of an individual fibril have been excluded as outliers. At a mean effective indentation depth of  $12.4 \text{ nm} \pm 2.3 \text{ nm}$  for unglycated (N=30) and  $10.2 \text{ nm} \pm 1.6 \text{ nm}$  (N=10) for glycated fibrils and an overall mean hydrated fibril diameter of  $191 \text{ nm} \pm 39 \text{ nm}$  the measurements have been successfully kept below the 10% safety threshold for the model of a semi-directionally infinite substrate [41]. Mean values of the individual test groups can be found in table 5.1.

Indentation modulus is shown to increase significantly in both test groups, albeit being almost unnoticeable in the control group: An increase by 15% in the control group ( $p = 0.043$ ) and by 42% in the MGO group ( $p = 0.002$ ) as shown in figure 5.1.

To conclude, that the difference in indentation modulus after glycation in the MGO group was indeed caused by glycation and not by mere chance, the difference of differences between control and MGO group was tested statistically. A two sample T-test of the two before-after-differences reveals the effect of glycation to indeed be significant ( $p = 0.018, \beta = 69\%$ ).

Measured Collagen Fibril Properties				
	Control Group $N = 10$		MGO Group $N = 10$	
	Before	After	Before	After
$E_{mod}$ [MPa]	$0.775 \pm 0.26$	$0.892 \pm 0.36$	$1.08 \pm 0.39$	$1.53 \pm 0.13$
$\Delta E_{mod}$ [MPa]	$+0.171 \pm 0.192$		$+0.452 \pm 0.36$	
<b><math>\Delta E_{MGO} - \Delta E_{Control}</math> [MPa]</b>	<b><math>0.335 \pm 0.27</math> p = 0.018</b>			
$\Phi$ [mV]	$-30.1 \pm 8.3$	$-24 \pm 8.4$	$-12.1 \pm 9.1$	$-33 \pm 8.6$
$\Delta \Phi$ [mV]	$+6.1 \pm 6.4$		$-20.9 \pm 10.4$	
<b><math>\Delta \Phi_{MGO} - \Delta \Phi_{Control}</math> [mV]</b>	<b><math>-27.02 \pm 8.1</math> p = <math>1.62 * 10^{-6}</math></b>			
$D_{dry}$ [nm]	$91.3 \pm 14$	$86.7 \pm 22$	$97.2 \pm 26$	$128.3 \pm 29$
$\Delta D_{dry}$ [nm]	$-4.5 \pm 12$		$+31 \pm 9$	
$\Delta D_{dry MGO} - \Delta D_{dry Control}$ [nm]	$35.6 \pm 17$			
$D_{wet}$ [nm]	$177.7 \pm 39$	$186.4 \pm 39$	$195.0 \pm 37$	$205.2 \pm 42$
$\Delta D_{wet}$ [nm]	$+8.6 \pm 11$		$+10.1 \pm 10$	
$\Delta D_{wet MGO} - \Delta D_{wet Control}$ [nm]	$1.5 \pm 12$			
$S_R$ [%]	$194 \pm 28$	$221 \pm 47$	$205 \pm 31$	$161 \pm 12$
$\Delta S_R$ [%]	$+27 \pm 36$		$-44 \pm 22$	
$\Delta S_R MGO - \Delta S_R Control$ [%]	$-71.4 \pm 28$			
$D_B$ [nm]	$66.7 \pm 2.1$	$65.8 \pm 1.7$	$66.3 \pm 2.7$	$67.2 \pm 3.6$
$\Delta D_B$ [nm]	$-0.9 \pm 1.6$		$+0.8 \pm 5.3$	
$\Delta D_B MGO - \Delta D_B Control$ [nm]	$1.77 \pm 3.71$			

Table 5.1.: The table shows a summary of the analyzed metrics as means  $\pm$  standard deviation.  $E_{mod}$  is the indentation modulus derived with the Oliver Pharr method [80] [81],  $\Phi$  is difference between glass and fibril surface potential,  $D_{dry}$  is the fibril diameter in air,  $D_{wet}$  is the fibril diameter in PBS,  $S_R$  is the relative swelling of the fibril diameter and  $D_B$  is the D-Banding period.

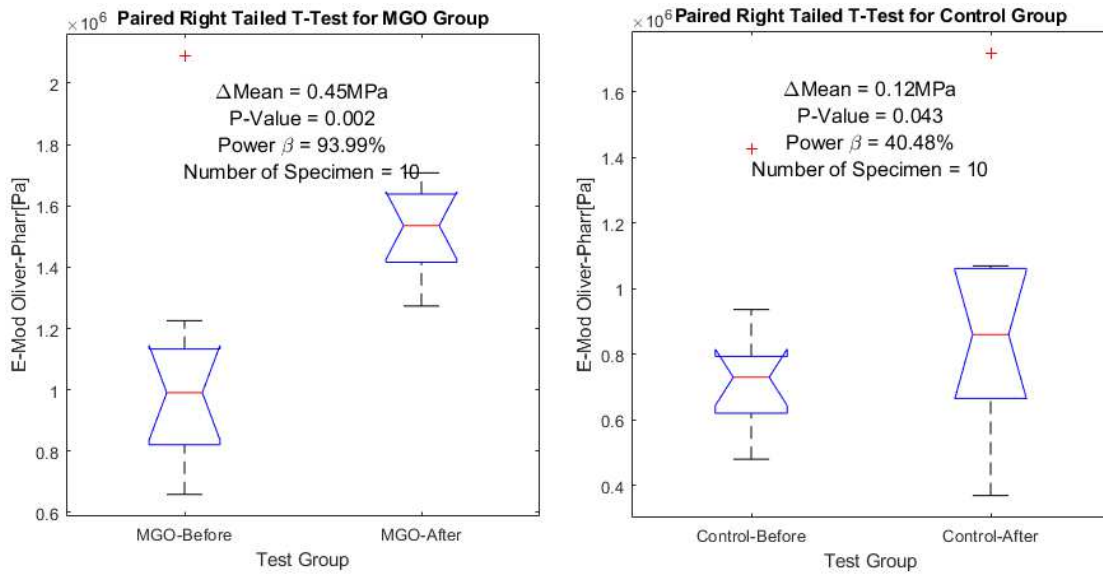


Figure 5.1.: Boxplots of the changes in indentation modulus between before and after the glycation process of both MGO and control group are being shown. Even though both groups show a significant increase in  $E_{mod}$ , the MGO groups is significantly larger.

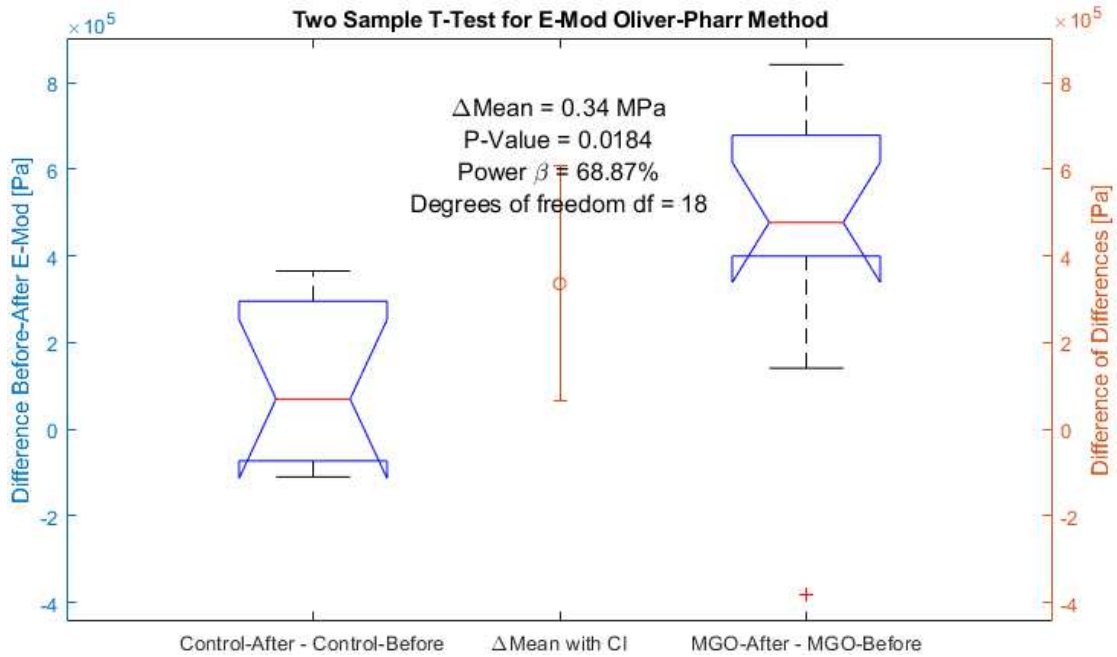


Figure 5.2.: Two sample T-test of the difference of differences (Orange dot in the middle  $\Delta \text{Mean} \pm 95\% \text{ Confidence Interval}$ ) showing the  $E_{mod}$ -increase in the MGO group to be significantly higher than the control groups.

Generally, on the reading of box plots: On each box, the central red mark indicates the median, and the bottom and top edges of the box indicate the 25th and 75th percentiles, respectively. The whiskers extend to the most extreme data points not considered outliers, and the outliers are plotted individually using the red '+' symbol. Notches display the variability of the median between samples.

The vertical width of a notch is computed so that box plots whose notches do not overlap (as above) have different medians at the 5% significance level. The significance level is based on a normal distribution assumption, but comparisons of medians are reasonably robust for other distributions. (From Matlab R2020a Documentation [103])

Figure 5.3 shows a randomly chosen fibril out of the MGO group before and after glycation to illustrate the changes: (A) shows the height map of the fibril along with the 16 apex points that are used for analysis, (B) shows one specific force curve of the map, corresponding to the green star on the height map, along with its indentation modulus derived from the Oliver-Pharr method. (C) is a box plot representing all of the apex points indentation moduli. (D) shows the slope of the Deflection-vs-Z-Displacement curves along with the averaged reference slope derived from the glass force curves. Ideally the reference slope is 1 and the fibrils slopes are around 0.5. (E) plots the indentation modulus against the indentation depth, while (F) relates the indentation depth to the projected area of the reconstructed cantilever tip.

## 5.2. Changes in Fibril Surface Potential through Glycation

KPFM measurements were done on the same collagen fibrils as above with a lift height of 0 *nm* to reveal relative-to-glass changes in fibril surface potential in air and at room temperature. Human decision making on the choice of areas to be analysed has been almost eliminated from data processing via automated image masking algorithms. While results (table 5.1) show a small but significant increase in surface potential in the control group  $\Delta\Phi_{Control} = 6.1 \text{ mV}$  ( $p = 0.015$ ), the MGO-glycated test group shows a significant and comparatively larger shift in the opposite direction  $\Delta\Phi_{MGO} = -20.92 \text{ mV}$  ( $p = 0.00013$ ). A two sample T-test for the difference of differences shows it to be very unlikely for this result to have happened by chance ( $p = 1.62 * 10^{-6}$ ) (see fig. 5.4). Figure 5.5 shows the typical changes that were observed in the MGO group after glycation. The typical downwardshift in relative surface potential, in this case from an average of  $-8.3 \text{ mV}$  to  $-29.77 \text{ mV}$ , is well pronounced and can be seen by the naked eye.

## 5.3. Other Metrics

In addition to the two observations the experiment was designed for, the effects of glycation on fibril swelling and D-Banding could be examined as well.

As can be seen in the full statistical analysis in appendix A.2 and in an exemplary case in figure 5.5 and fibril D-Banding, derived from Fast Fourier Transform (FFT) on the apex line, appears to be almost unaffected: with a D-Banding period of 68.4 *nm* before and 68.2 *nm* after glycation and accounting for the fact that with the given resolution and, additionally, curved apex lines D-Banding determination through Fourier analysis of the apex line isn't expected to be very accurate. The

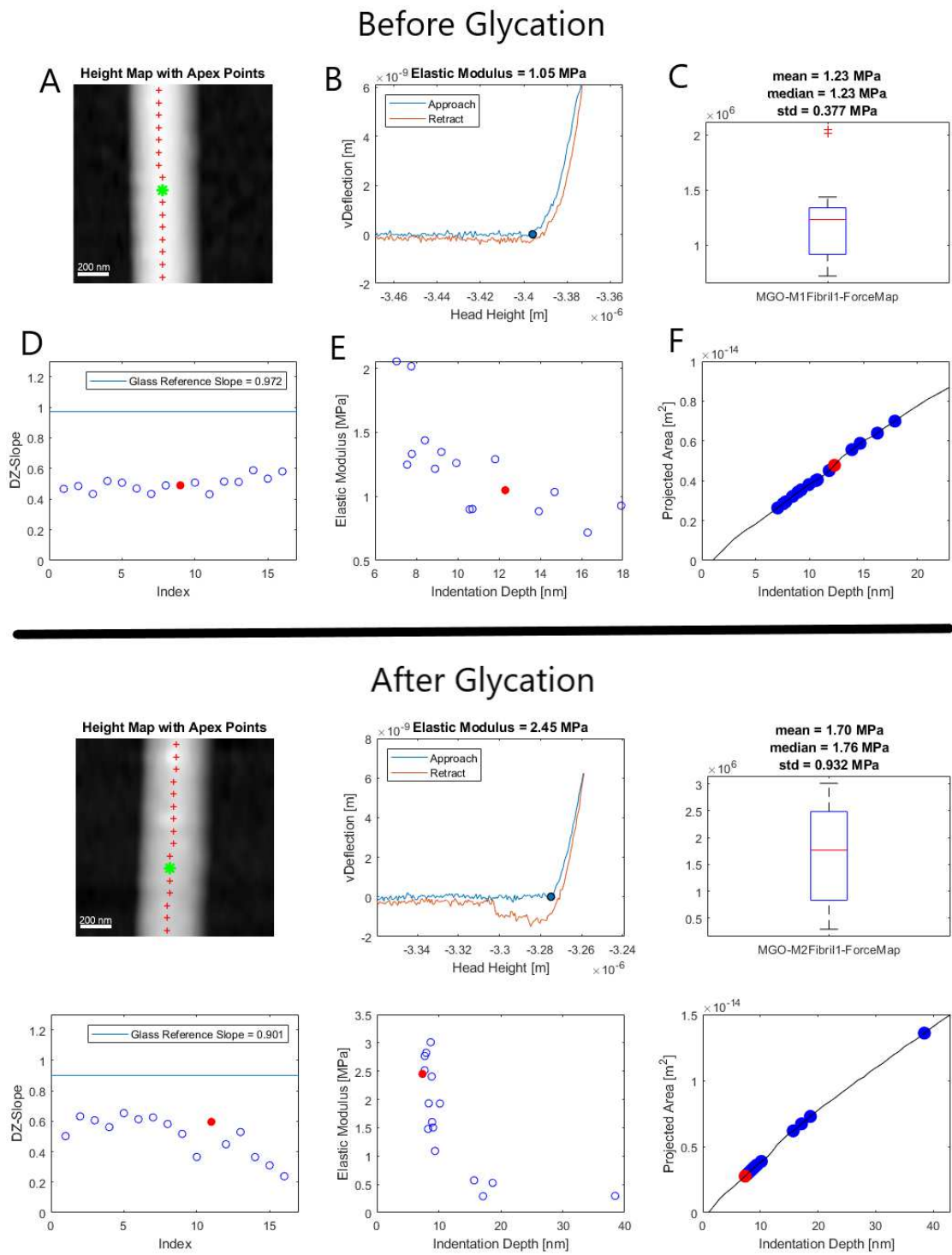


Figure 5.3.: (Figure description in full text body)

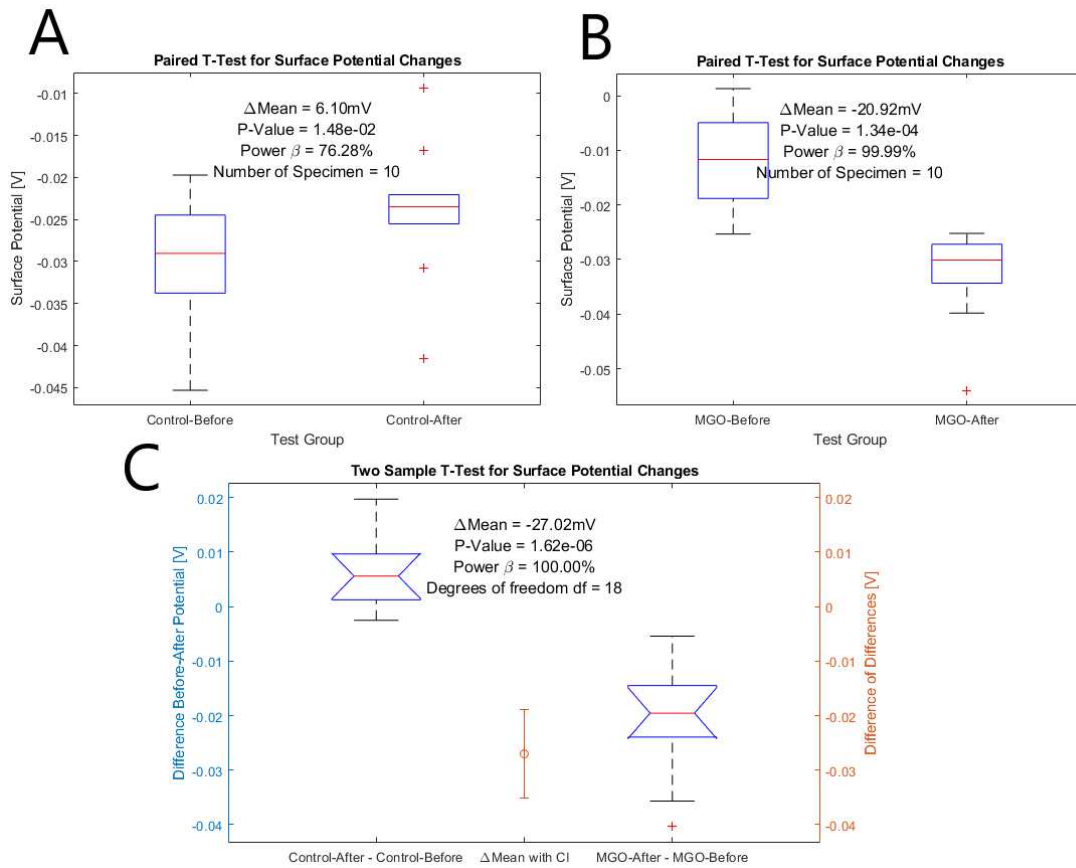


Figure 5.4.: Statistical analysis of the difference in relative surface potential before and after glycation in both groups (A,B) and difference of differences with 95% confidence interval (C).

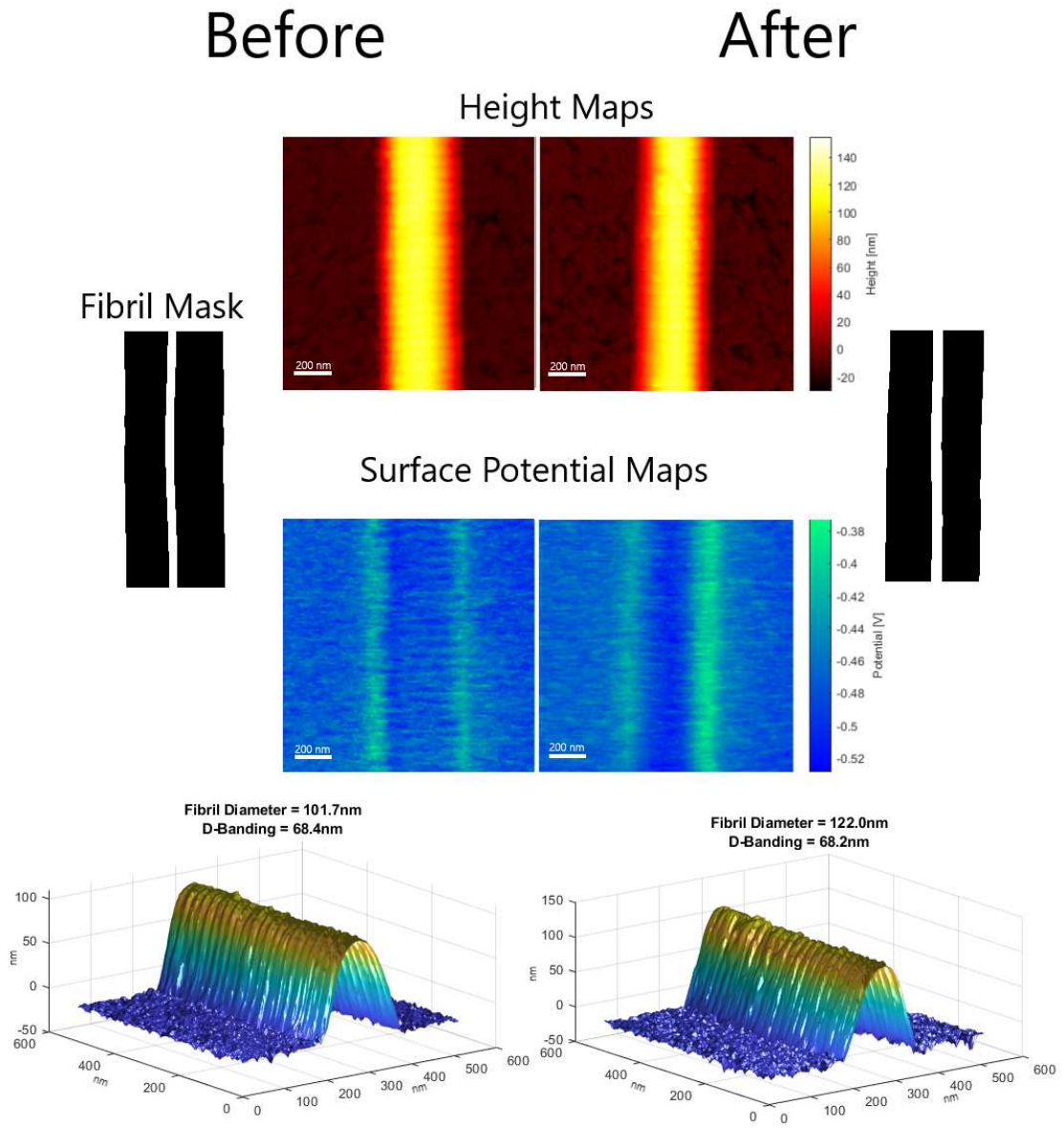


Figure 5.5.: Exemplary specimen taken from the MGO group illustrating the changes happening between before and after glycation of a collagen fibril. (Exhaustive description in full text body)



overall statistics over both test groups show no significant changes in either direction nor group as seen in table 5.1.

Fibril height and swelling, however, do seem to undergo substantial changes through glycation. Dry height in the control group went from  $(91.3 \pm 14) \text{ nm}$  to  $(86.7 \pm 22) \text{ nm}$  and from  $(97.3 \pm 26) \text{ nm}$  to  $(128.2 \pm 29) \text{ nm}$  in the MGO group, while hydrated height went from  $(177.7 \pm 39) \text{ nm}$  to  $(186.3 \pm 39) \text{ nm}$  and from  $(195 \pm 38) \text{ nm}$  to  $(205.2 \pm 41) \text{ nm}$  respectively as shown in figure 5.6. This means that significant change in height only occurred in the **dry** fibril diameter in the MGO group.

Accordingly, relative swelling  $S_R$ , defined as

$$S_R = \frac{D_{hydrated}}{D_{dry}}, \quad (5.1)$$

decreases significantly in the MGO group (figure 5.7 and 5.6).

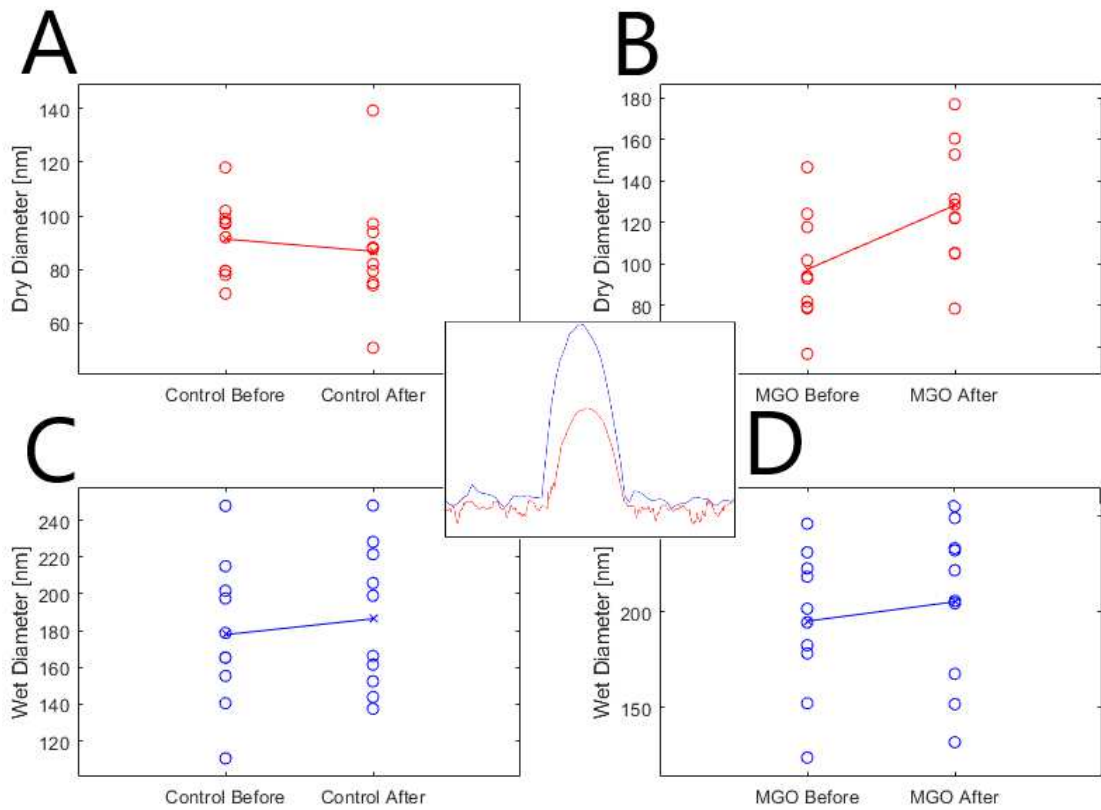


Figure 5.6.: Changes in fibril diameter, dry and hydrated, over the course of the experiment: Control group dry (A) and hydrated (C); MGO group dry (B) and hydrated (D). The overlaid image in the middle depicts the cross section of a random fibril during the KPFM (dry, red) and the AFM (wet, blue) measurement.

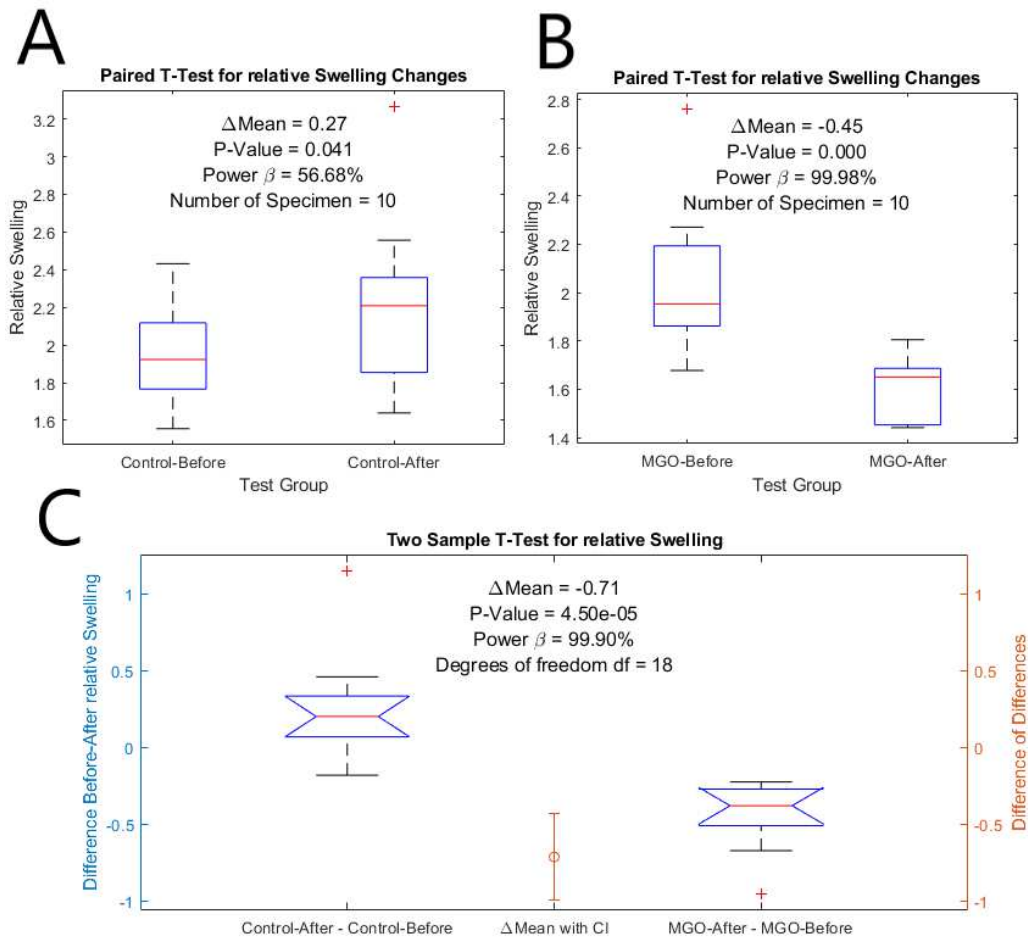


Figure 5.7.: Statistical analysis of the before-after differences, respectively, in the control (A) and the MGO (B) group, and of the difference of differences with 95% confidence interval (C). Due to a noticeable increase in dry height in the MGO group, swelling goes down.



Die approbierte gedruckte Originalversion dieser Diplomarbeit ist an der TU Wien Bibliothek verfügbar.  
The approved original version of this thesis is available in print at TU Wien Bibliothek.

## 6. Discussion

The goal of presented study was the design and execution of an experiment that accurately models the mechanical and surface-electrical effects of physiologic, AGE-inducing agents in individual collagen fibrils derived from mouse tail tendon. It was designed to provide high statistical power through repeated measurements of the *very same* fibrils at every step of the experiment, therefore allowing statistically *paired* observations. The additional measurement of a control group provides a useful baseline to compare the results against, thereby minimizing the effect of systematic errors or changes unrelated to glycation happening during experiment work-flow. In a well set up laboratory environment the experiment is easily reproducible and hinges on techniques that are well tried and documented [66][104][67][105].

### Glycation

One limitation of the study is the choice of methylglyoxal (MGO) as AGE crosslinking agent: MGOs high reactivity [106] and capability to saturate AGE crosslinking in the span of mere hours, while still being an intermediate product in the Maillard reaction, that leads to AGEs in living tissue [21][32], makes it a convenient tool in an experimental setting and, in the present work specifically, allows for before-after AFM force mapping measurements on the same day, without intermediate de- and rehydration steps. Usage of just MGO as crosslinking agent may potentially skip relevant processes and interactions that happen during the Maillard reaction. Therefore, one may miss-model in vivo physiological changes. Repeating this experiment with more physiologic reacting agents, like glucose - with noticeable glycation after months - , or pentoses such as D-ribose - with noticeable glycation after days/weeks - , all else equal, could lead to more accurate modelling of non-enzymatic collagen crosslinking and possibly interesting findings, relating the different reaction agents to one another.

### AFM Force Maps

For the first time, AFM nanoindentation measurements in liquid (PBS) directly revealed mechanical changes in indentation modulus in mouse tendon fibrils through glycation. The derived indentation moduli of hydrated fibrils are comparable to

other studies, probing similar materials [48][43][23], though many reported values in literature derive from experiments on dried collagen fibrils in air (e.g. [41][44]) and cannot be compared to the data presented here. Specifically, stiffening of the fibrils following AGE inducing crosslinking agents is a well documented phenomenon [23][20][107].

Comparing to ongoing research by Ehrenberger et al. [50], the observed significant increase in indentation modulus in the control group seems surprising: even though the MGO group could be shown to have stiffened significantly ( $p = 0.018$ ) more,  $\Delta E_{MGO} \approx +42\%(\pm 33\%SD)$  compared to  $\Delta E_{Control} \approx +15\%(\pm 32\%SD)$ , the increase is unexpected. Given the fact that in aforementioned study [50] rise in indentation modulus seemed to stop after a precautionary PBS(+EDTA)-incubation period of at least 2 hours, which accordingly has also been applied in this study, the change that was observed here might warrant further investigation of the effects that hydration, dehydration and incubation in buffer solutions such as PBS (+EDTA) have on collagen fibrils handled in this way. The effect might possibly be caused by mineralized depositions from PBS. With the effect barely being significant though, -  $p = 0.043$  in a right tailed T-test; a two tailed T-test shows no significance - the increase might also be a statistical fluke.

## KPFM Surface Potential

Kelvin-Probe-Force-Microscopy surface potential measurements of the collagen fibrils relative potential in air at room conditions have successfully shown the effects of MGO induced glycation. The findings match results from previous studies found in literature [30][31], though studies of this kind are to this day relatively rare and deserve reproduction. While the control groups surface potential had a small but significant upshift, the MGO-glycated group experienced a significant downshift in surface potential relative to the surrounding glass  $-20.9 \text{ mV} \pm 10.4 \text{ mV}$  ( $p = 0.00013$ ).

Observations on surface electrical properties are of high interest in the working dynamics of living biological systems because they affect very important biological mechanisms such as cell adhesion and interaction with the extracellular matrix (ECM), which in turn might be relevant for collagen turnover and matrix repair mechanisms [30][108]. Even though KPFM measurements on biological materials in air seem to be a poor model for physiological environments, fixed charges, such as carboxyl (COOH) or amino (NH<sub>2</sub>) groups in proteins, are nevertheless expected to show similar characteristics in both air and aqueous environments [105].

## Swelling and D-Banding

Fibril D-Banding was determined from the KPFM measurements in air only and didn't show any noticeable changes within the accuracy limits owed to the rather low resolution of images. The overall mean of  $66.5 \text{ nm} \pm 2.6 \text{ nm SD}$  seems to reasonably validate findings in literature that have been reported over a variety of different measurement techniques [2].

However, fibril swelling from the combined data of the KPFM (dry) and AFM nanoindentation (wet) measurements seems to show glycation related changes that disagree with previously reported findings: swelling has been found to increase with glycation [23], while present work finds reduced swelling in the MGO-after group (figure 5.7).

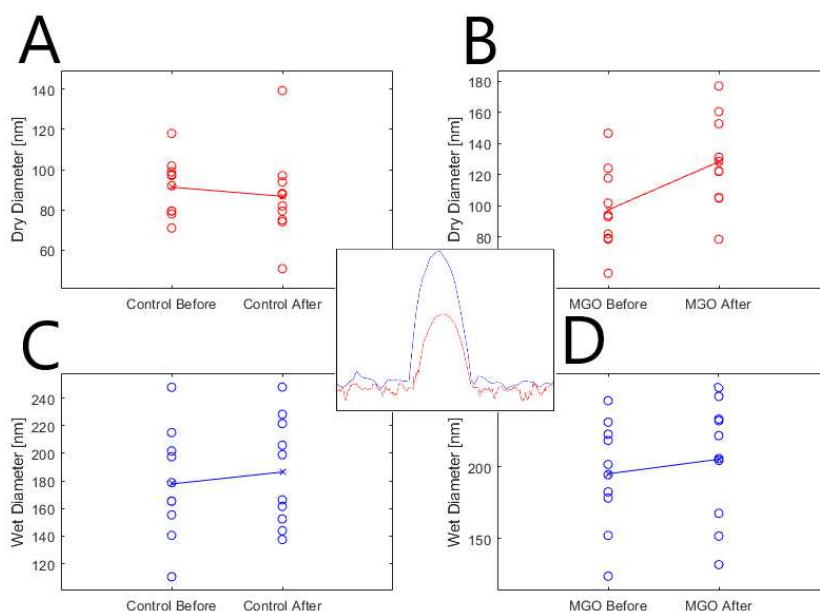


Figure 6.1.: Changes in fibril diameter, dry and hydrated, over the course of the experiment: Control group dry (A) and hydrated (C); MGO group dry (B) and hydrated (D). The overlaid image in the middle depicts the cross section of a random fibril during the KPFM (dry, red) and the AFM (wet, blue) measurement.

As shown in figure 6.1, it is not the diameter of the hydrated fibril that changed to a significant degree, but the dry diameter. This may be caused by the fibril

being constrained to mostly keep its through hydration expanded structure due to the many additional AGE crosslinks that have been added during glycation. Note that the fibrils were dehydrated in the desiccator for a whole day between the AFM-After and the KPFM-After measurement.

## CNN Contact Point Determination

Looking at the apex force curves and the contact point estimates of all tested methods, the new CNN-based method seems to be by far the most robust and accurate. Ranking the methods by computation time, SD6 is by far the fastest, followed by CNN without Monte Carlo Dropout, followed by RoV and finally Monte Carlo Dropout CNN, which is roughly  $N$  times slower than just CNN, with  $N$  being the number of Dropout predictions ( $N=100$  throughout this work).

Statistical analysis of indentation moduli (see table 4.1 or figure 5.1, 5.2 and appendix A.1) seems to produce lower p-values and higher power in the other two methods (SD6, RoV), though, which is very surprising, especially considering how far off the contact point placement of the RoV-method appears to be a lot of the time.

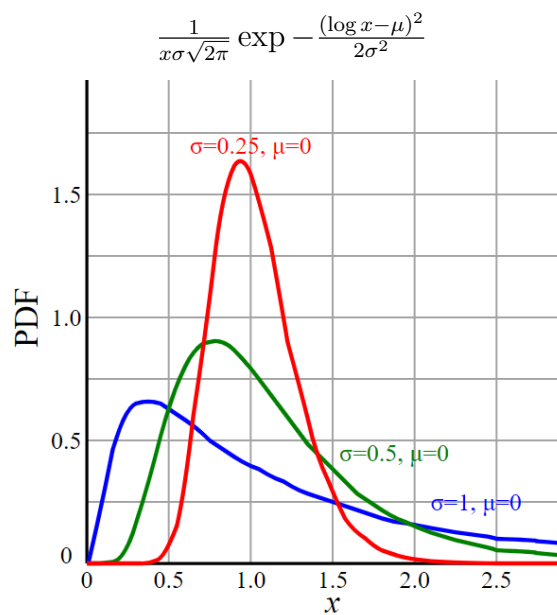


Figure 6.2.: Typical probability density function of a log-normal distribution with  $\mu = 0$  and varying standard deviation  $\sigma$ . [109]



A proposed explanation for this is that assuming the indentation moduli to be normally distributed might be problematic. Seeing that the modulus is a variable bounded by zero and the data distributions having fairly high standard deviations. Therefore, underestimations of the indentation modulus caused by the contact point being set too far to the left are additively not all that far away from the population mean, while being far off in a multiplicative sense.

This effect of bounded variables in biology and economics has been known for a long time and suggests that such variables are log-normally distributed instead [110], meaning that the logarithm of the data is normally distributed.

Figure 6.3 pretty clearly shows, that the log-normal distribution fits the data much better than a gaussian fit, which overestimates the occurrence of low (even below 0) values of the indentation modulus, while giving the higher values a probability that is too low. Gavara (2016) [87] also shows a clear log-normal distribution in their data. Values shown in table 4.1 might therefore not accurately represent the quality of the tested contact point determination methods because the underestimations resulting from the contact point being misplaced to the left non-linearly shifts the elastic modulus to smaller values, whose frequency is overestimated in a normal distribution.

Statistical analysis based on the logarithm of the data instead of the usual approach could be favourable to more realistically evaluate measurements in future experiments and should be subject to further investigation.

Evaluation of the CNN method wasn't the main focus of present work and deserves more rigorous investigation. One weakness of the data and comparisons shown here is that the network was trained on force curves that were done under very similar conditions and AFM settings as the ones in present work. For a more general evaluation, testing on a broad spectrum of AFM force curves should be done and in case of poor performance the training data set should be expanded with more diverse data.

Labelling of the training data itself should be carried out more carefully and with clear guidelines in place, maybe even comparing or averaging over labels done by different researchers. Several data augmentation techniques during training but also during inference could help make the method even more reliable and accurate. Possible uses of the uncertainty metric derived from the Monte Carlo Dropout CNN variant should be explored and, if not found to be useful, the simpler much faster CNN without dropout should probably be preferred as it can be used to deal with much higher data volumes, for example from experiments that don't reduce the number of analysed force curves to a few topologically interesting, e.g. fibril apex in collagen fibril experiments, spots.

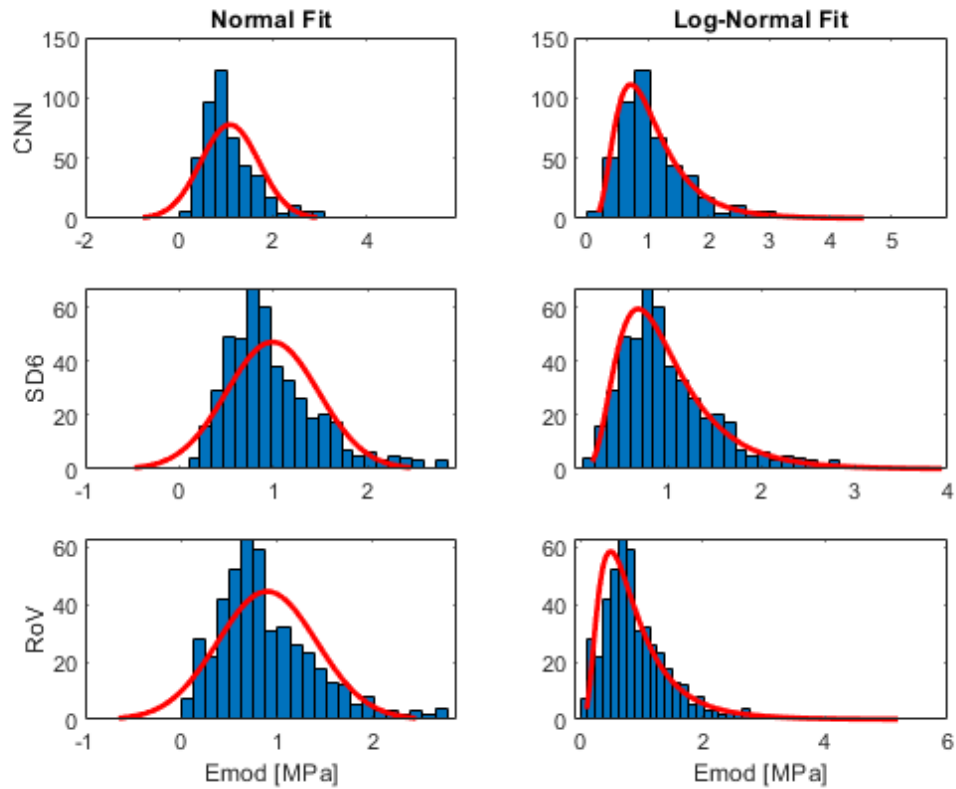


Figure 6.3.: Histogram of all *untreated* apex force curves indentation moduli in the experiment derived from all three methods with a normal (left) or log-normal (right) fit.

## 7. Conclusion

The goal of this study was to give direct evidence of the changes induced by glycation on the level of individual collagen fibrils. To this end, atomic force microscopy (AFM) nanoindentation in phosphate buffered solution (PBS) as well as Kelvin probe force microscopy (KPFM) surface potential experiments in air were performed on collagen fibrils extracted from mouse tail tendon. In the course of data processing, a probabilistic deep convolutional neural network (CNN) for contact point determination in AFM force mapping data analysis has been developed, trained and deployed. Albeit not exhaustive, comparisons to other methods show very promising results. This approach yielded very accurate and robust contact point estimates, making it a possible candidate for improved force map data analysis in wide ranging applications in industry, medicine and research. Regarding the study design, in order to produce direct evidence individual fibrils from the same fascicle were split into a test and a control group (N=10 for both) and probed with the aforementioned techniques before and after treatment. The test group was glycated with methylglyoxal (MGO), a very rapid and potent cross-linker, as a treatment. Indentation moduli went up after treatment in both groups, though significantly more so in the MGO-treated group. To the authors best knowledge, this is the first time glycation induced stiffening of individual fibrils has been tested through nanoindentation in liquid. KPFM experiments revealed changes in the fibrils (relative to glass) surface potential in both groups, with the control groups potential shifting up slightly and the glycated group experiencing a large down-shift. This change is largely attributed to the fact that the amino acids involved in AGE cross-linking, lysine and arginine, both possess positively charged side chains, thereby lowering net surface charges when being occupied with AGEs. From the combined experimental data, interesting changes in fibril diameter and swelling were observed. While hydrated diameters remained virtually unchanged in both groups, dry diameter in the MGO-treated group increased significantly, in consequence leading to reduced swelling. The mechanisms leading to this change remain unclear, though a heightened ability to bind water through H-bonds or, alternatively, structural freezing of the fibrils hydrated diameter through the newly formed cross-links are proposed as candidate explanations. AGE-related changes in fibril properties through the natural ageing process or through elevated blood sugar levels in diabetes patients are of great interest. The tested properties in this study are not only highly relevant for fibril mechanics, as is shown directly through

nanoindentations, but also for biological function through the link between surface charge and cell interaction, proliferation and adhesion. Using presented study protocol, differences between various cross-linkers and types of AGEs could be explored in a comprehensive and effective way, expanding our understanding in these fields of study.

# Bibliography and References

- [1] S. Ricard-Blum. “The Collagen Family”. In: *Cold Spring Harbor Perspectives in Biology* 3.1 (Dec. 2010), a004978–a004978. DOI: 10.1101/cshperspect.a004978.
- [2] *Collagen*. Ed. by Peter Fratzl. Springer-Verlag GmbH, May 10, 2008. ISBN: 9780387739069. URL: <https://www.ebook.de/de/product/8898719/collagen.html>.
- [3] Nicole Verzijl et al. “Effect of Collagen Turnover on the Accumulation of Advanced Glycation End Products”. In: *Journal of Biological Chemistry* 275.50 (Sept. 2000), pp. 39027–39031. DOI: 10.1074/jbc.m006700200.
- [4] Garry J. Rucklidge et al. “Turnover rates of different collagen types measured by isotope ratio mass spectrometry”. In: *Biochimica et Biophysica Acta (BBA) - General Subjects* 1156.1 (Dec. 1992), pp. 57–61. DOI: 10.1016/0304-4165(92)90095-c.
- [5] Jess G. Snedeker and Alfonso Gautieri. “The role of collagen crosslinks in ageing and diabetes - the good, the bad, and the ugly.” In: *Muscles, ligaments and tendons journal* 4 (3 July 2014), pp. 303–308. ISSN: 2240-4554. epublish.
- [6] Allen J Bailey, Robert Gordon Paul, and Lynda Knott. “Mechanisms of maturation and ageing of collagen”. In: *Mechanisms of Ageing and Development* 106.1-2 (Dec. 1998), pp. 1–56. DOI: 10.1016/s0047-6374(98)00119-5.
- [7] WHO. *WHO Europe Diabetes Statistics*. Sept. 16, 2020. URL: <https://www.euro.who.int/en/health-topics/noncommunicable-diseases/diabetes/data-and-statistics>.
- [8] Ravichandran Ramasamy et al. “Advanced glycation end products and RAGE: a common thread in aging, diabetes, neurodegeneration, and inflammation”. In: *Glycobiology* 15.7 (Mar. 2005), 16R–28R. DOI: 10.1093/glycob/cwi053.

- [9] Kristin L. Reigle et al. “Non-enzymatic glycation of type I collagen diminishes collagen-proteoglycan binding and weakens cell adhesion”. In: *Journal of Cellular Biochemistry* 104.5 (Aug. 2008), pp. 1684–1698. DOI: 10.1002/jcb.21735.
- [10] Asheesh Bedi et al. “Diabetes mellitus impairs tendon-bone healing after rotator cuff repair”. In: *Journal of Shoulder and Elbow Surgery* 19.7 (Oct. 2010), pp. 978–988. DOI: 10.1016/j.jse.2009.11.045.
- [11] ALAN W STITT. “Advanced glycation: an important pathological event in diabetic and age related ocular disease”. In: *British Journal of Ophthalmology* 85.6 (June 2001), pp. 746–753. DOI: 10.1136/bjo.85.6.746.
- [12] Melpomeni Peppas, Jaime Uribarri, and Helen Vlassara. “The role of advanced glycation end products in the development of atherosclerosis”. In: *Current Diabetes Reports* 4.1 (Feb. 2004), pp. 31–36. DOI: 10.1007/s11892-004-0008-6.
- [13] Nobuyuki Sasaki et al. “Advanced Glycation End Products in Alzheimer’s Disease and Other Neurodegenerative Diseases”. In: *The American Journal of Pathology* 153.4 (Oct. 1998), pp. 1149–1155. DOI: 10.1016/s0002-9440(10)65659-3.
- [14] M. Saito and K. Marumo. “Collagen cross-links as a determinant of bone quality: a possible explanation for bone fragility in aging, osteoporosis, and diabetes mellitus”. In: *Osteoporosis International* 21.2 (Sept. 2009), pp. 195–214. DOI: 10.1007/s00198-009-1066-z.
- [15] S. Yamagishi, K. Nakamura, and H. Inoue. “Possible participation of advanced glycation end products in the pathogenesis of osteoporosis in diabetic patients”. In: *Medical Hypotheses* 65.6 (Jan. 2005), pp. 1013–1015. DOI: 10.1016/j.mehy.2005.07.017.
- [16] J. M. Forbes. “Role of Advanced Glycation End Products in Diabetic Nephropathy”. In: *Journal of the American Society of Nephrology* 14.90003 (Aug. 2003), 254S–258. DOI: 10.1097/01.asn.0000077413.41276.17.
- [17] G. Kesava Reddy. “Cross-Linking in Collagen by Nonenzymatic Glycation Increases the Matrix Stiffness in Rabbit Achilles Tendon”. In: *Experimental Diabetes Research* 5.2 (2004), pp. 143–153. DOI: 10.1080/15438600490277860.
- [18] G.Kesava Reddy, Lisa Stehno-Bittel, and Chukuka S. Enwemeka. “Glycation-Induced Matrix Stability in the Rabbit Achilles Tendon”. In: *Archives of Biochemistry and Biophysics* 399.2 (Mar. 2002), pp. 174–180. DOI: 10.1006/abbi.2001.2747.

- [19] C. Eriksen et al. “Systemic stiffening of mouse tail tendon is related to dietary advanced glycation end products but not high-fat diet or cholesterol”. In: *Journal of Applied Physiology* 117.8 (Oct. 2014), pp. 840–847. DOI: 10.1152/japplphysiol.00584.2014.
- [20] Rene B. Svensson et al. “Effects of maturation and advanced glycation on tensile mechanics of collagen fibrils from rat tail and Achilles tendons”. In: *Acta Biomaterialia* 70 (Apr. 2018), pp. 270–280. DOI: 10.1016/j.actbio.2018.02.005.
- [21] Yufei Li et al. “Advanced glycation end-products diminish tendon collagen fiber sliding”. In: *Matrix Biology* 32.3-4 (Apr. 2013), pp. 169–177. DOI: 10.1016/j.matbio.2013.01.003.
- [22] Alfonso Gautieri et al. “Advanced glycation end-products: Mechanics of aged collagen from molecule to tissue”. In: *Matrix Biology* 59 (May 2017), pp. 95–108. DOI: 10.1016/j.matbio.2016.09.001.
- [23] Orestis G. Andriotis et al. “Hydration and nanomechanical changes in collagen fibrils bearing advanced glycation end-products”. In: *Biomedical Optics Express* 10.4 (Mar. 2019), p. 1841. DOI: 10.1364/boe.10.001841.
- [24] T.A. Collier et al. “Effect on the mechanical properties of type I collagen of intra-molecular lysine-arginine derived advanced glycation end-product cross-linking”. In: *Journal of Biomechanics* 67 (Jan. 2018), pp. 55–61. DOI: 10.1016/j.jbiomech.2017.11.021.
- [25] Samir Hamaia and Richard W. Farndale. “Integrin Recognition Motifs in the Human Collagens”. In: *Advances in Experimental Medicine and Biology*. Springer Netherlands, 2014, pp. 127–142. DOI: 10.1007/978-94-017-9153-3\_9.
- [26] F. G. Giancotti. “Integrin Signaling”. In: *Science* 285.5430 (Aug. 1999), pp. 1028–1033. DOI: 10.1126/science.285.5430.1028.
- [27] Soo-Hyun Kim, Jeremy Turnbull, and Scott Guimond. “Extracellular matrix and cell signalling: the dynamic cooperation of integrin, proteoglycan and growth factor receptor”. In: *Journal of Endocrinology* 209.2 (Feb. 2011), pp. 139–151. DOI: 10.1530/joe-10-0377.
- [28] Alfonso Gautieri et al. “Age- and diabetes-related nonenzymatic crosslinks in collagen fibrils: Candidate amino acids involved in Advanced Glycation End-products”. In: *Matrix Biology* 34 (Feb. 2014), pp. 89–95. DOI: 10.1016/j.matbio.2013.09.004.
- [29] Julia C Hadley, Keith M Meek, and Nageena S Malik. “Glycation changes the charge distribution of type I collagen fibrils”. In: *Glycoconjugate Journal* 15.8 (1998), pp. 835–840. DOI: 10.1023/a:1006928403140.

- [30] Patrick Mesquida et al. “Evaluation of surface charge shift of collagen fibrils exposed to glutaraldehyde”. In: *Scientific Reports* 8.1 (July 2018). DOI: 10.1038/s41598-018-28293-1.
- [31] Sneha Bansode et al. “Glycation changes molecular organization and charge distribution in type I collagen fibrils”. In: *Scientific Reports* 10.1 (Feb. 2020). DOI: 10.1038/s41598-020-60250-9.
- [32] Gion Fessel et al. “Advanced Glycation End-Products Reduce Collagen Molecular Sliding to Affect Collagen Fibril Damage Mechanisms but Not Stiffness”. In: *PLoS ONE* 9.11 (Nov. 2014). Ed. by Hazel R. C. Screen, e110948. DOI: 10.1371/journal.pone.0110948.
- [33] P. Kannus. “Structure of the tendon connective tissue”. In: *Scandinavian Journal of Medicine and Science in Sports* 10.6 (Dec. 2000), pp. 312–320. DOI: 10.1034/j.1600-0838.2000.010006312.x.
- [34] Vincent R. Sherman, Wen Yang, and Marc A. Meyers. “The materials science of collagen”. In: *Journal of the Mechanical Behavior of Biomedical Materials* 52 (Dec. 2015), pp. 22–50. DOI: 10.1016/j.jmbbm.2015.05.023.
- [35] Alfonso Gautieri et al. “Hierarchical Structure and Nanomechanics of Collagen Microfibrils from the Atomistic Scale Up”. In: *Nano Letters* 11.2 (Feb. 2011), pp. 757–766. DOI: 10.1021/nl103943u.
- [36] Mitch Leslie. “Making tendons”. In: *Journal of Cell Biology* 172.2 (Jan. 2006), pp. 167–167. DOI: 10.1083/jcb1722fta2.
- [37] Orestis G. Andriotis, Sylvia Desissaire, and Philipp J. Thurner. “Collagen Fibrils: Nature’s Highly Tunable Nonlinear Springs”. In: *ACS Nano* 12.4 (Mar. 2018), pp. 3671–3680. DOI: 10.1021/acsnano.8b00837.
- [38] W. Folkhard et al. “Quantitative analysis of the molecular sliding mechanisms in native tendon collagen — time-resolved dynamic studies using synchrotron radiation”. In: *International Journal of Biological Macromolecules* 9.3 (June 1987), pp. 169–175. DOI: 10.1016/0141-8130(87)90047-x.
- [39] R. Puxkandl et al. “Viscoelastic properties of collagen: synchrotron radiation investigations and structural model”. In: *Philosophical Transactions of the Royal Society of London. Series B: Biological Sciences* 357.1418 (Feb. 2002). Ed. by A. J. Bailey et al., pp. 191–197. DOI: 10.1098/rstb.2001.1033.
- [40] Rene B. Svensson et al. “Fracture Mechanics of Collagen Fibrils: Influence of Natural Cross-Links”. In: *Biophysical Journal* 104.11 (June 2013), pp. 2476–2484. DOI: 10.1016/j.bpj.2013.04.033.



- [41] Orestis G. Andriotis et al. “Nanomechanical assessment of human and murine collagen fibrils via atomic force microscopy cantilever-based nanoindentation”. In: *Journal of the Mechanical Behavior of Biomedical Materials* 39 (Nov. 2014), pp. 9–26. DOI: 10.1016/j.jmbbm.2014.06.015.
- [42] O. G. Andriotis et al. “Structure–mechanics relationships of collagen fibrils in the osteogenesis imperfecta mouse model”. In: *Journal of The Royal Society Interface* 12.111 (Oct. 2015), p. 20150701. DOI: 10.1098/rsif.2015.0701.
- [43] Colin A. Grant et al. “Effects of hydration on the mechanical response of individual collagen fibrils”. In: *Applied Physics Letters* 92.23 (June 2008), p. 233902. DOI: 10.1063/1.2937001.
- [44] August J. Heim, William G. Matthews, and Thomas J. Koob. “Determination of the elastic modulus of native collagen fibrils via radial indentation”. In: *Applied Physics Letters* 89.18 (Oct. 2006), p. 181902. DOI: 10.1063/1.2367660.
- [45] Marco P.E. Wenger et al. “Mechanical Properties of Collagen Fibrils”. In: *Biophysical Journal* 93.4 (Aug. 2007), pp. 1255–1263. DOI: 10.1529/biophysj.106.103192.
- [46] Majid Minary-Jolandan and Min-Feng Yu. “Nanomechanical Heterogeneity in the Gap and Overlap Regions of Type I Collagen Fibrils with Implications for Bone Heterogeneity”. In: *Biomacromolecules* 10.9 (Sept. 2009), pp. 2565–2570. DOI: 10.1021/bm900519v.
- [47] Samuel J. Baldwin et al. “Nanomechanical Mapping of Hydrated Rat Tail Tendon Collagen I Fibrils”. In: *Biophysical Journal* 107.8 (Oct. 2014), pp. 1794–1801. DOI: 10.1016/j.bpj.2014.09.003.
- [48] Colin A. Grant et al. “Tuning the Elastic Modulus of Hydrated Collagen Fibrils”. In: *Biophysical Journal* 97.11 (Dec. 2009), pp. 2985–2992. DOI: 10.1016/j.bpj.2009.09.010.
- [49] Manuel R. Uhlig and Robert Magerle. “Unraveling capillary interaction and viscoelastic response in atomic force microscopy of hydrated collagen fibrils”. In: *Nanoscale* 9.3 (2017), pp. 1244–1256. DOI: 10.1039/c6nr07697a.
- [50] Christian Ehrenberger. “Investigating the influence of PBS on individual collagen fibrils through AFM nanoindentation”. MA thesis. Institute for Lightweight Design and Structure Biomechanics (ILSB), TU Vienna.
- [51] René B. Svensson et al. “Tensile Properties of Human Collagen Fibrils and Fascicles Are Insensitive to Environmental Salts”. In: *Biophysical Journal* 99.12 (Dec. 2010), pp. 4020–4027. DOI: 10.1016/j.bpj.2010.11.018.

- [52] Yehe Liu, Roberto Ballarini, and Steven J. Eppell. “Tension tests on mammalian collagen fibrils”. In: *Interface Focus* 6.1 (Feb. 2016), p. 20150080. DOI: 10.1098/rsfs.2015.0080.
- [53] S.J Eppell et al. “Nano measurements with micro-devices: mechanical properties of hydrated collagen fibrils”. In: *Journal of The Royal Society Interface* 3.6 (Nov. 2005), pp. 117–121. DOI: 10.1098/rsif.2005.0100.
- [54] Andrew S. Quigley et al. “In tendons, differing physiological requirements lead to functionally distinct nanostructures”. In: *Scientific Reports* 8.1 (Mar. 2018). DOI: 10.1038/s41598-018-22741-8.
- [55] Andrew S. Quigley et al. “Combining tensile testing and structural analysis at the single collagen fibril level”. In: *Scientific Data* 5.1 (Oct. 2018). DOI: 10.1038/sdata.2018.229.
- [56] S. M. Asif Iqbal, Dylan Deska-Gauthier, and Laurent Kreplak. “Assessing collagen fibrils molecular damage after a single stretch–release cycle”. In: *Soft Matter* 15.30 (2019), pp. 6237–6246. DOI: 10.1039/c9sm00832b.
- [57] Andrew S. Quigley, Samuel P. Veres, and Laurent Kreplak. “Bowstring Stretching and Quantitative Imaging of Single Collagen Fibrils via Atomic Force Microscopy”. In: *PLOS ONE* 11.9 (Sept. 2016). Ed. by Joseph P. R. O. Orgel, e0161951. DOI: 10.1371/journal.pone.0161951.
- [58] K GOH et al. “Analysis of collagen fibril diameter distribution in connective tissues using small-angle X-ray scattering”. In: *Biochimica et Biophysica Acta (BBA) - General Subjects* 1722.2 (Mar. 2005), pp. 183–188. DOI: 10.1016/j.bbagen.2004.12.004.
- [59] Melissa M. Basil-Jones et al. “Collagen Fibril Orientation in Ovine and Bovine Leather Affects Strength: A Small Angle X-ray Scattering (SAXS) Study”. In: *Journal of Agricultural and Food Chemistry* 59.18 (Sept. 2011), pp. 9972–9979. DOI: 10.1021/jf202579b.
- [60] Melissa M. Basil-Jones et al. “Collagen Fibril Alignment and Deformation during Tensile Strain of Leather: A Small-Angle X-ray Scattering Study”. In: *Journal of Agricultural and Food Chemistry* 60.5 (Jan. 2012), pp. 1201–1208. DOI: 10.1021/jf2039586.
- [61] Peter Fratzl et al. “Nucleation and growth of mineral crystals in bone studied by small-angle X-ray scattering”. In: *Calcified Tissue International* 48.6 (June 1991), pp. 407–413. DOI: 10.1007/bf02556454.
- [62] Karen Reiser, Richard J. McCormick, and Robert B. Rucker. “Enzymatic and nonenzymatic cross-linking of collagen and elastin”. In: *The FASEB Journal* 6.7 (Apr. 1992), pp. 2439–2449. DOI: 10.1096/fasebj.6.7.1348714.

- [63] NAILA AHMED and PAUL J. THORNALLEY. “Peptide Mapping of Human Serum Albumin Modified Minimally by Methylglyoxalin Vitroandin Vivo”. In: *Annals of the New York Academy of Sciences* 1043.1 (June 2005), pp. 260–266. DOI: 10.1196/annals.1333.031.
- [64] Naila Ahmed et al. “Increased formation of methylglyoxal and protein glycation, oxidation and nitrosation in triosephosphate isomerase deficiency”. In: *Biochimica et Biophysica Acta (BBA) - Molecular Basis of Disease* 1639.2 (Oct. 2003), pp. 121–132. DOI: 10.1016/j.bbadis.2003.08.002.
- [65] Naila Ahmed et al. “Methylglyoxal-Derived Hydroimidazolone Advanced Glycation End-Products of Human Lens Proteins”. In: *Investigative Ophthalmology & Visual Science* 44.12 (Dec. 2003), p. 5287. DOI: 10.1167/iovs.03-0573.
- [66] Arturo M. Baró and Ronald G. Reifengerger. *Atomic Force Microscopy in Liquid*. Wiley-VCH, Jan. 24, 2012. 402 pp. ISBN: 9783527649839. URL: [https://www.ebook.de/de/product/21194002/atomic\\_force\\_microscopy\\_in\\_liquid.html](https://www.ebook.de/de/product/21194002/atomic_force_microscopy_in_liquid.html).
- [67] Wilhelm Melitz et al. “Kelvin probe force microscopy and its application”. In: *Surface Science Reports* 66.1 (Jan. 2011), pp. 1–27. DOI: 10.1016/j.surfrep.2010.10.001.
- [68] *Marienfeld Glass Slides*. URL: <https://www.marienfeld-superior.com/microscope-slides-thickness-approx-1-mm.html>.
- [69] *Sigma Aldrich PBS*. July 12, 2020. URL: <https://www.sigmaaldrich.com/catalog/product/sigma/p4417?lang=de&region=AT>.
- [70] David S. Auld. “[14] Removal and replacement of metal ions in metallopeptidases”. In: *Proteolytic Enzymes: Aspartic and Metallo Peptidases*. Elsevier, 1995, pp. 228–242. DOI: 10.1016/0076-6879(95)48016-1.
- [71] *Desiccator*. July 12, 2020. URL: <https://us.vwr.com/store/product/21346683/vwr-vacuum-desiccator-bottom-and-lid-with-socket-valve>.
- [72] Yukie SAEGUSA and Hajime TABATA. “Usefulness of Infrared Thermometry in Determining Body Temperature in Mice”. In: *Journal of Veterinary Medical Science* 65.12 (2003), pp. 1365–1367. DOI: 10.1292/jvms.65.1365.
- [73] E. Leikina et al. “Type I collagen is thermally unstable at body temperature”. In: *Proceedings of the National Academy of Sciences* 99.3 (Jan. 2002), pp. 1314–1318. DOI: 10.1073/pnas.032307099.
- [74] *JPK General*. URL: <https://www.jpk.com/jpk-have-joined-bruker>.

- [75] *Zeiss AXIOS inv. Microscope*. URL: <https://www.zeiss.com/corporate/int/home.html?vaURL=www.zeiss.de/en>.
- [76] *PNP-DB Cantilevers (Product website)*. URL: <https://www.nanoworld.com/pyrex-nitride-rectangular-silicon-nitride-cantilever-afm-tip-pnp-db>.
- [77] *TGT-1 Grating*. URL: <https://ntmdt-tips.com/products/view/tgt1>.
- [78] David J. Keller and Fransiska S. Franke. “Envelope reconstruction of probe microscope images”. In: *Surface Science* 294.3 (Sept. 1993), pp. 409–419. DOI: 10.1016/0039-6028(93)90126-5.
- [79] John E. Sader, James W. M. Chon, and Paul Mulvaney. “Calibration of rectangular atomic force microscope cantilevers”. In: *Review of Scientific Instruments* 70.10 (Oct. 1999), pp. 3967–3969. DOI: 10.1063/1.1150021.
- [80] W.C. Oliver and G.M. Pharr. “An improved technique for determining hardness and elastic modulus using load and displacement sensing indentation experiments”. In: *Journal of Materials Research* 7.6 (June 1992), pp. 1564–1583. DOI: 10.1557/jmr.1992.1564.
- [81] W.C. Oliver and G.M. Pharr. “Measurement of hardness and elastic modulus by instrumented indentation: Advances in understanding and refinements to methodology”. In: *Journal of Materials Research* 19.1 (Jan. 2004), pp. 3–20. DOI: 10.1557/jmr.2004.19.1.3.
- [82] *Bruker Dimension FastScan AFM*. URL: <https://www.bruker.com/de/products/surface-and-dimensional-analysis/atomic-force-microscopes/dimension-fastscan/overview.html>.
- [83] *NanoScope V*. URL: <http://www.eicsac.com/nanoscope5.pdf>.
- [84] *Olympus AC-200TN-R3*. URL: [http://probe.olympus-global.com/en/product/omcl\\_ac200ts\\_r3/spec.html](http://probe.olympus-global.com/en/product/omcl_ac200ts_r3/spec.html).
- [85] *Gwyddion*. URL: <http://gwyddion.net/>.
- [86] S. L. Crick and F. C.-P. Yin. “Assessing Micromechanical Properties of Cells with Atomic Force Microscopy: Importance of the Contact Point”. In: *Biomechanics and Modeling in Mechanobiology* 6.3 (June 2006), pp. 199–210. DOI: 10.1007/s10237-006-0046-x.
- [87] N ria Gavara. “Combined strategies for optimal detection of the contact point in AFM force-indentation curves obtained on thin samples and adherent cells”. In: *Scientific Reports* 6.1 (Feb. 2016). DOI: 10.1038/srep21267.

- [88] M. A. Monclus, T. J. Young, and D. Di Maio. “AFM indentation method used for elastic modulus characterization of interfaces and thin layers”. In: *Journal of Materials Science* 45.12 (Mar. 2010), pp. 3190–3197. DOI: 10.1007/s10853-010-4326-6.
- [89] Rafael Benítez et al. “A new automatic contact point detection algorithm for AFM force curves”. In: *Microscopy Research and Technique* 76.8 (June 2013), pp. 870–876. DOI: 10.1002/jemt.22241.
- [90] Yow-Ren Chang et al. “Automated AFM force curve analysis for determining elastic modulus of biomaterials and biological samples”. In: *Journal of the Mechanical Behavior of Biomedical Materials* 37 (Sept. 2014), pp. 209–218. DOI: 10.1016/j.jmbbm.2014.05.027.
- [91] David C. Lin, Emiliós K. Dimitriadis, and Ferenc Horkay. “Robust Strategies for Automated AFM Force Curve Analysis—I. Non-adhesive Indentation of Soft, Inhomogeneous Materials”. In: *Journal of Biomechanical Engineering* 129.3 (Nov. 2006), pp. 430–440. DOI: 10.1115/1.2720924.
- [92] Kathryn A. Melzak et al. “Rationalized approach to the determination of contact point in force-distance curves: Application to polymer brushes in salt solutions and in water”. In: *Microscopy Research and Technique* (2010), NA–NA. DOI: 10.1002/jemt.20851.
- [93] Ian N. Sneddon. “The relation between load and penetration in the axisymmetric boussinesq problem for a punch of arbitrary profile”. In: *International Journal of Engineering Science* 3.1 (May 1965), pp. 47–57. DOI: 10.1016/0020-7225(65)90019-4.
- [94] Alex Krizhevsky, Ilya Sutskever, and Geoffrey E Hinton. “ImageNet Classification with Deep Convolutional Neural Networks”. In: *Advances in Neural Information Processing Systems 25*. Ed. by F. Pereira et al. Curran Associates, Inc., 2012, pp. 1097–1105. URL: <http://papers.nips.cc/paper/4824-imagenet-classification-with-deep-convolutional-neural-networks.pdf>.
- [95] Facundo Bre, Juan M. Gimenez, and Victor D. Fachinotti. “Prediction of wind pressure coefficients on building surfaces using artificial neural networks”. In: *Energy and Buildings* 158 (Jan. 2018), pp. 1429–1441. DOI: 10.1016/j.enbuild.2017.11.045.
- [96] Aphex34. URL: [https://de.wikipedia.org/wiki/Convolutional\\_Neural\\_Network#/media/Datei:Typical\\_cnn.png](https://de.wikipedia.org/wiki/Convolutional_Neural_Network#/media/Datei:Typical_cnn.png).
- [97] Kaiming He et al. “Deep Residual Learning for Image Recognition”. In: (Dec. 10, 2015). arXiv: 1512.03385v1 [cs.CV].

- [98] *Matlab R2020a Deep Learning Toolbox*. URL: <https://de.mathworks.com/products/deep-learning.html>.
- [99] Yarin Gal and Zoubin Ghahramani. “Dropout as a Bayesian Approximation: Representing Model Uncertainty in Deep Learning”. In: (June 6, 2015).
- [100] Johannes Suppan et al. “Tick attachment cement - reviewing the mysteries of a biological skin plug system”. In: *Biological Reviews* 93.2 (Nov. 2017), pp. 1056–1076. DOI: 10.1111/brv.12384.
- [101] Diederik P. Kingma and Jimmy Ba. “Adam: A Method for Stochastic Optimization”. In: (Dec. 22, 2014). arXiv: 1412.6980v9 [cs.LG].
- [102] John P. A. Ioannidis. “Why Most Published Research Findings Are False”. In: *PLoS Medicine* 2.8 (Aug. 2005), e124. DOI: 10.1371/journal.pmed.0020124.
- [103] Matlab R2020a. *On Boxplots*. URL: <https://de.mathworks.com/help/stats/box-plots.html>.
- [104] Greg Haugstad. *Atomic force microscopy : understanding basic modes and advanced applications*. Hoboken, New Jersey: John Wiley & Sons, Inc, 2012. ISBN: 9780470638828.
- [105] Alexander D. D. Stone and Patrick Mesquida. “Kelvin-probe force microscopy of the pH-dependent charge of functional groups”. In: *Applied Physics Letters* 108.23 (June 2016), p. 233702. DOI: 10.1063/1.4953571.
- [106] C. G. Schalkwijk and C. D. A. Stehouwer. “Methylglyoxal, a Highly Reactive Dicarbonyl Compound, in Diabetes, Its Vascular Complications, and Other Age-Related Diseases”. In: *Physiological Reviews* 100.1 (Jan. 2020), pp. 407–461. DOI: 10.1152/physrev.00001.2019.
- [107] Lanti Yang et al. “Micromechanical bending of single collagen fibrils using atomic force microscopy”. In: *Journal of Biomedical Materials Research Part A* 82A.1 (2007), pp. 160–168. DOI: 10.1002/jbm.a.31127.
- [108] N.C. Avery and A.J. Bailey. “The effects of the Maillard reaction on the physical properties and cell interactions of collagen”. In: *Pathologie Biologie* 54.7 (Sept. 2006), pp. 387–395. DOI: 10.1016/j.patbio.2006.07.005.
- [109] <https://commons.wikimedia.org/wiki/User:Krishnavedala>. *Probability distribution functions of log-normal distributions*. Mar. 23, 2015. URL: [https://commons.wikimedia.org/wiki/File:PDF-log\\_normal\\_distributions.svg](https://commons.wikimedia.org/wiki/File:PDF-log_normal_distributions.svg).
- [110] Arthur L. Koch. “The logarithm in biology 1. Mechanisms generating the log-normal distribution exactly”. In: *Journal of Theoretical Biology* 12.2 (Nov. 1966), pp. 276–290. DOI: 10.1016/0022-5193(66)90119-6.

# A. Appendix

## A.1. Alternative Statistical Analysis

### Analysis done on $E_{mod}$ derived from the RoV-method

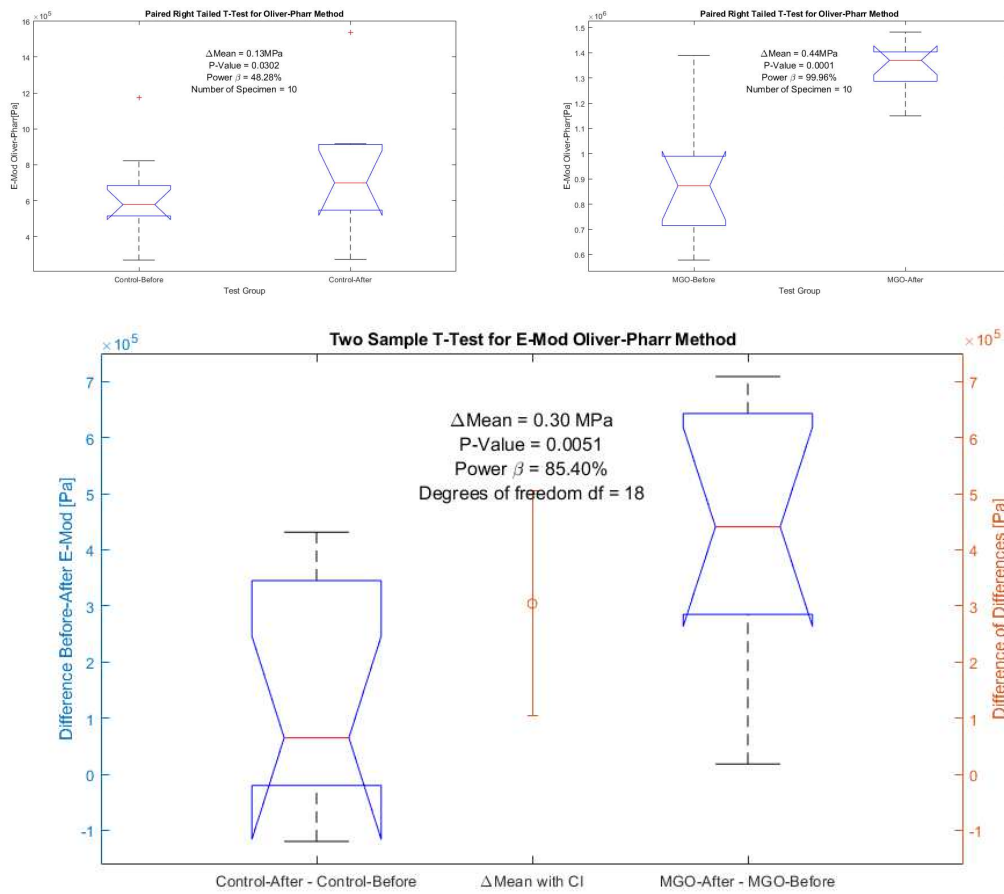


Figure A.1.

### Analysis done on $E_{mod}$ derived from the SD6-method

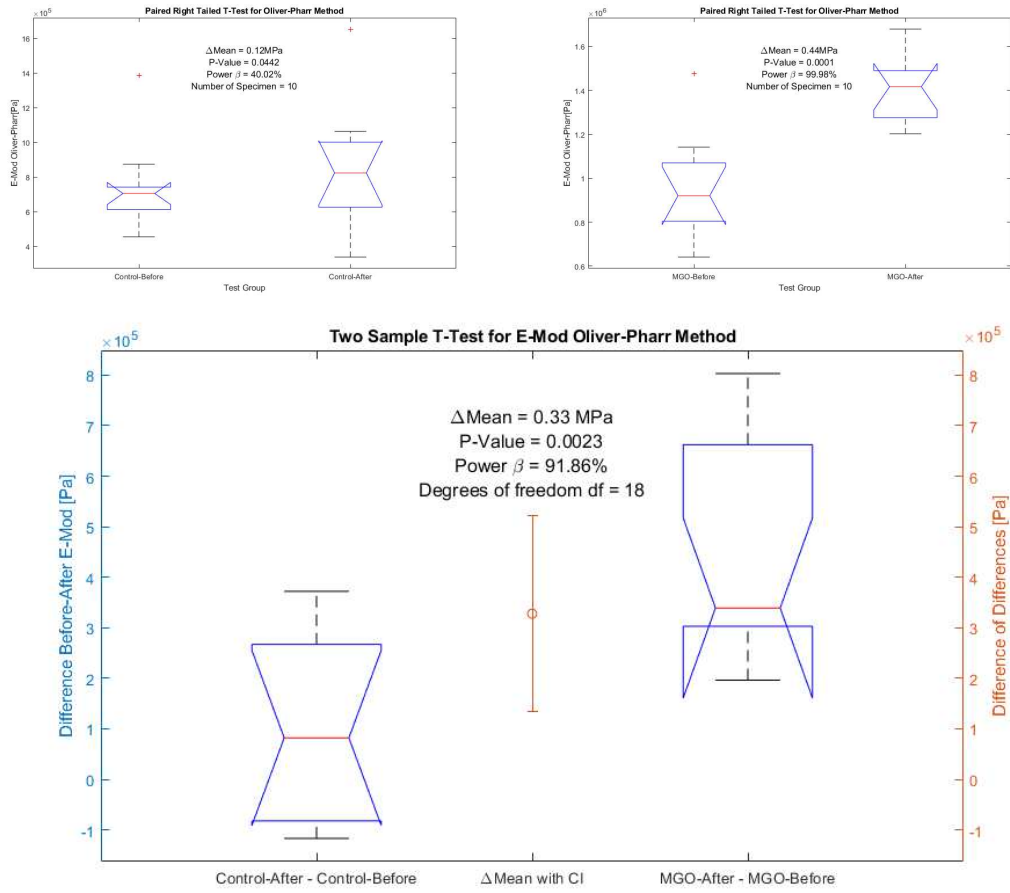


Figure A.2.



## A.2. D-Banding Statistical Analysis

### Analysis of the D-Banding period

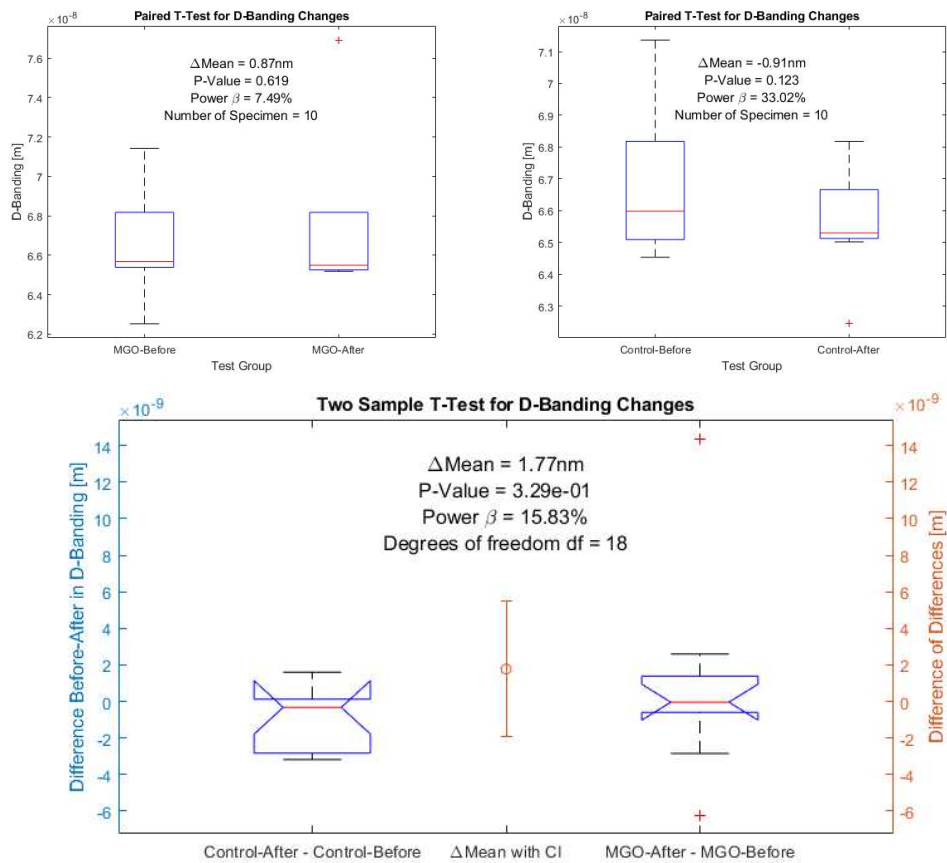


Figure A.3.: Statistical analysis of the D-Banding did not show significant changes at any level.

## A.3. Handling of Debris on Fibrils

Figure A.4 shows the typical changes that were observed in the MGO group after glycation on a fibril with an unidentified structure on top. The elevated structure that can be seen in both instances at the top is either random debris or the top layer of collagen molecules detaching from the fibril, maybe because of denaturation, and was excluded during the only manual masking step of the analysis. The typical downwardshift in relative surface potential, in this case from an average

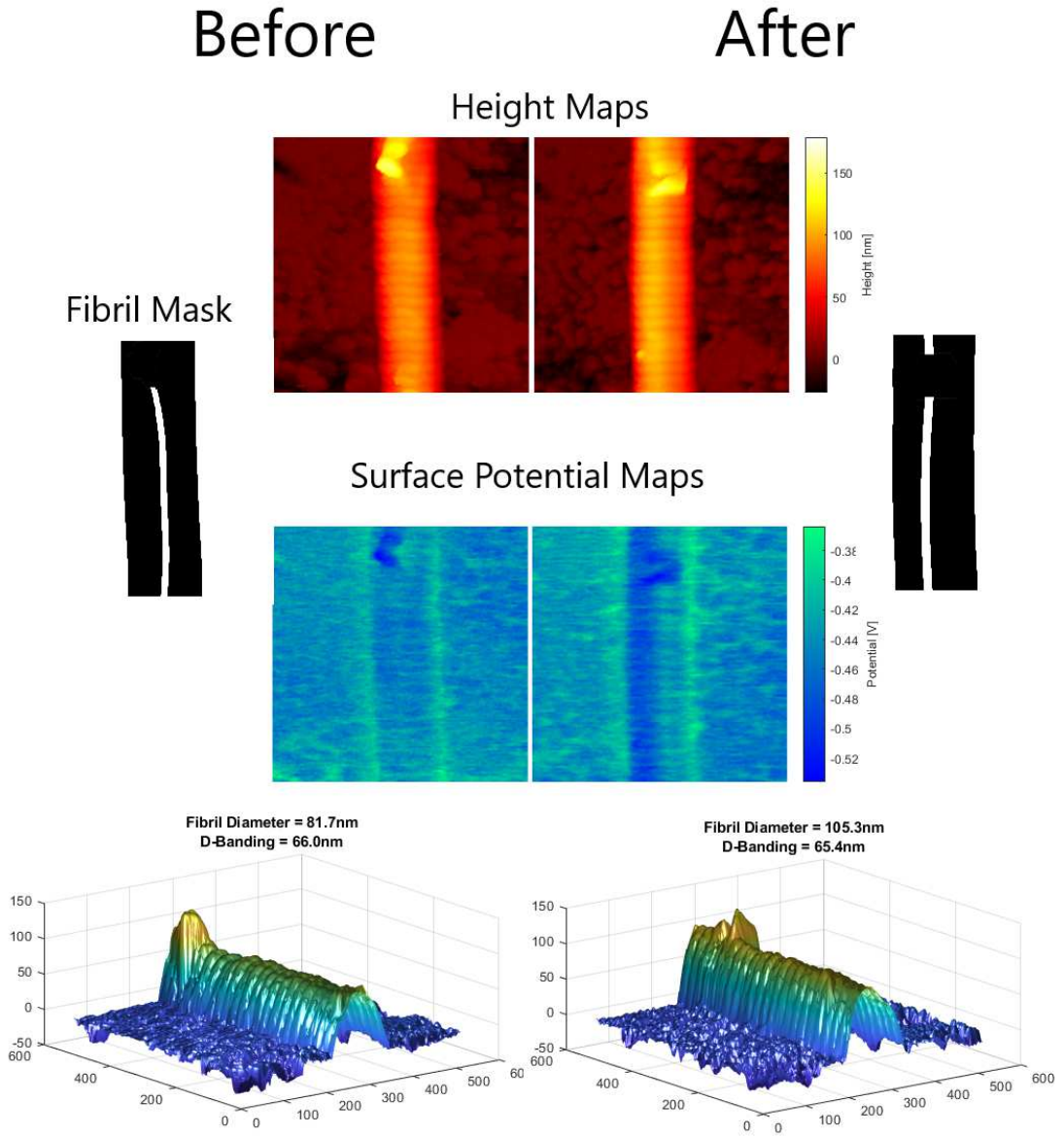


Figure A.4.: Exemplary specimen with debris taken from the MGO group. Excluded regions can be seen on fibril mask. (Exhaustive description in full text body)

of  $-9.68\text{ mV}$  to  $-28.49\text{ mV}$ , is well pronounced and can be seen by the naked eye. Given that the mask for the fibril surface potential lays along the fibril apex the difference in curvature possibly hints at a slight rearrangement of the general fibril structure, be it through re- and dehydration, the force exerted during force mapping or a combination of both.

During data processing of both AFM force maps and KPFM surface potential maps, exclusion of suspicious areas was done by hand, representing the only non-automated step.